UNIVERSITY OF OKLAHOMA

GRADUATE COLLEGE

MULTI-SCALE CHARACTERIZATION OF THE WOODFORD SHALE IN WEST-CENTRAL OKLAHOMA:

FROM SCANNING ELECTRON MICROSCOPE TO 3D SEISMIC

A DISSERTATION

SUBMITTED TO THE GRADUATE FACULTY

in partial fulfillment of the requirements for the

Degree of

DOCTOR OF PHILOSOPHY

By

NABANITA GUPTA
Norman, Oklahoma
2012

INTEGRATED CHARACTERIZATION OF THE WOODFORD SHALE IN WEST-CENTRAL OKLAHOMA

A DISSERTATION APPROVED FOR THE
CONOCOPHILLIPS SCHOOL OF GEOLOGY AND GEOPHYSICS

BY

_____
Dr. Kurt J. Marfurt, Chair

_____
Dr. Chandra S. Rai

_____
Dr. Carl H. Sondergeld

_____
Dr. Richard D. Elmore

_____
Dr. Zeev Reches

_____
Dr. Mike A. Miller

Dedicated to my parents

Acknowledgements

The journey towards the Ph.D. degree has been an eventful and enriching experience through these five years at the University of Oklahoma. I feel really blessed to work with important people from two schools and three disciplines within the Mewbourne College of Earth and Energy. There are many people who made this journey a unique experience.

First of all, I would like to extend my deepest gratitude to my adviser, Dr. Kurt J. Marfurt, which cannot be expressed with mere words; all I can do is to thank him from the bottom of my heart. He not only showed his confidence in me at difficult time, he also helped to extend my research in completely new direction where I had very limited knowledge. His invaluable advise on writing and presentations helped me to improve a lot. I feel extremely fortunate that Dr. Marfurt gave me an opportunity to work with him, one of the most wonderful persons I have ever met in my life. I will cherish my meeting with him for the rest of my life.

I wouldn't be able to achieve my goal without Dr. Chandra S. Rai, who technically advised my research and helped me with financial support. I am deeply indebted to him for giving me the opportunity to work with him and his confidence in me for whatever I wanted to do. He is a man of constant source of inspiration. His guidance, constructive criticism and scholastic advice kept me in focus throughout my Ph.D. study.

I thank Dr. Carl H. Sondergeld, another important member of my research committee. His attitude, the constant strive to be perfect and heartfelt passion for work

sometimes made me reevaluate about my capabilities ultimately, I hope to achieve a similar outlook on life and work. I am highly indebted for all his support and effort.

I want to convey my sincere thanks to Dr. Mike Miller, one of my eminent committee members and one of the principal industry advocates in starting the Woodford project between The University of Oklahoma and Cimarex Energy.

I want to thank Dr. Richard D. Elmore for being in my committee and supporting me during my study at the University of Oklahoma both as a committee member and department chair. I also thank Dr. Zeev Reches for his comments and critical suggestions which played a great role to improve this dissertation.

My special thanks to Mr. Craig Caldwell for his thoughtful suggestions that improved my understanding and helped me to move forward with my interpretation. I thank Mr. Brian Cardott for his comments and suggestions on organic maturity. He also provided me an important dataset on the vitrinite reflectance that was critical for this project. Thanks to Mr. Richard Andrews for invaluable discussions.

My sincere gratitude to Cimarex Energy for providing support and data for this project. I also thank the Oklahoma Geological Survey for well and core databases and CGG-Veritas for providing a license to their seismic data volume for research and education.

I am indebted to Dr. Mark Curtis for his help with the SEM imaging. Thank you Mark. My gratitude to Gray Stowe for getting me familiarize with the equipments at the Integrated Core Characterization Center (IC^3). My heartfelt thanks to Bruce Spears, Aravinda Buddhala and Jeremy Jernigen at the IC^3 laboratory for all the help and support. My special thanks to the undergraduate students and fellow graduate students at the IC^3

laboratory for their help with the laboratory measurements. I wouldn't be able to finish the laboratory measurements without their help. I would like to thank all members of the IC^3 laboratory and Shale Consortium for granting their support towards my graduate study.

I wholeheartedly thank the AASPI consortium and its sponsors for their support for the geophysics part of my dissertation. Special thanks to Dr. J. Timothy Kwiatkowski for his help with the prestack seismic data analyses along with numerous help with the AASPI software and computer hardware. Without that help, I could not have progressed this far in the project.

Loads of thanks go to Schlumburger for providing their immense support to the University of Oklahoma through access to Techlog and Petrel software. I also thank CGG-Veritas for access to their Hampson-Russel software.

I want to thank all the student members at the AASPI consortium and also my fellow graduate students at the ConocoPhillips School of Geology and Geophysics. Special thanks to Dr. Sunday Amoyodo for his companionship along with several academic and non-academic discussions. I also want to thank my dear friends at the University of Oklahoma during these years: Dana, Evan, Avinash, Atish, Matt, Sumit, Cathrene, Debapriya, Roderick, Julieta, Pratik, Aneeta and many other colleagues who shared office or lab space with me and if not, shared good times through delightful chat.

Last but not the least, I would like to thank my family who are of utmost importance to me, I would like to say "Thank you" to my Mom (ma) and Dad (baba) for all the sacrifices they have made for me. Today I am here because of their constant inspiration, boundless love and affection. I would like to thank my brother Debajyoti,

sister-in-law Daita and my parents–in–law for their constant support throughout my Ph.D. study.

Finally, I deeply thank my spouse Dr. Supratik Sarkar for standing beside me while I was going through the roller coaster of euphoria and frustration as a graduate student. He was my mentor and helped me to get a quick-start with geophysics, of which I knew very little. Being an expert in the same discipline, he has always been the best critic of my research. His support through all the situations enabled me to finish my research and progress towards the goal to earn a Ph.D. I can't thank him enough for all the support he gave me over the last few years. Lastly, I would like to thank the super-power without which nothing can be accomplished.

Table of Contents

List of Tables

List of Figures

Abstract

This dissertation focuses on the characterization of unconventional resource-shales for resource evaluation using the Woodford Shale as a primary example for this study. The limited understanding of the actual rock properties together with the complex nature of the resource shales, demand an integrated characterization at multiple scales. In this research, I present a fully integrated characterization including petrophysical, geophysical and geological evaluation of the Woodford Shale in West Central Oklahoma, which improves the understanding about this shale as well as other resource shales. I have used a multi-scale dataset collected from multiple sources and ranging from nanometer scale scanning electron microscopic image analysis, microscopic observations made through petrographic microscope, macroscopic visual observations, laboratory measured petrophysical parameters, well-logs, to surface seismic data for regional characterization.

Driven by growing energy demand and technology advancement, resource-shales have emerged as one of the primary areas for hydrocarbon exploration. Petrophysical properties characterize both physical and mechanical properties and hence, are important for identifying sweet-spots for hydrocarbon exploration. This dissertation summarizes the petrophysical characterization of the Woodford Shale based on 300 samples collected from six hydrocarbon-producing and non-producing wells. Crushed rock porosity, bulk density, grain density, mineralogy, acoustic velocities, mercury injection capillary pressure along with total organic carbon content, rock-eval pyrolysis, and vitrinite reflectance were measured at the Integrated Core Characterization Center. NMR

measurements were made on few samples to track distribution of different fluids in the pore spaces. Visual inspections were made at macroscopic-, microscopic- and scanning electron microscope-scale in order to calibrate rock-petrophysical properties with the actual rock architecture. The wide porosity range from 1% to 10% indicates different rock types with variable storage capacities. Mineralogy indicates that the Woodford is a silica-dominated silty shale with small amount of carbonate. Rock-eval analyses indicate that the Woodford Shale in two of the studied wells fall within the oil window (Ro< 1%) and four wells fall within the dry gas-condensate window (Ro>1.2%). Wells from different maturity provide an opportunity to analyze changes in petrophysical properties with changes in thermal maturity. Laboratory measured petrophysical properties were finally analyzed through cluster analyses in order to identify three rock-types characterized by unique reservoir properties.

A set of seismic attributes help to illuminate both stratigraphic and structural features present within the Woodford interval on a regional scale. I used both conventional (for example, Sobel filter similarity, most positive and most negative principal curvatures) and recently developed (for example, coherent seismic energy, most negative principal curvature modulate by azimuth, reflector rotation with respect to reflector normal) seismic attributes in this study. Petrophysical properties extracted through simultaneous inversion of the prestack seismic data allowed me to perform regional characterization of the Woodford Shale in a semi-quantitative manner. Rock types identified through the petrophysical characterization in the previous section were combined with geophysical analyses to build a regional distribution of each rock type. Finally, seismic attributes, production data along with the geologic history indicate that

the basin-floor depressions are likely areas for presence of alternating TOC-rich ductile and TOC-lean brittle rock, forming potential sweet spots within the Woodford Shale.

Detailed analyses of macroscopic, microscopic and submicroscopic sedimentary features combined with the regional geologic history allowed me to build the depositional framework and associated lithofacies distribution for the Woodford Shale in the Anadarko Basin. Petrophysical measurements made on samples collected from each lithofacies present in six wells allowed me to correlate petrophysical properties with the geologic framework and identify petrophysical proxies that can be used to track stratigraphic changes in the uncored areas. This study reveals that mineralogy is one of the important tools for tracking the geologic history. Since mineralogy correlates well with other petrophysical properties, one can correlate the petrophysical properties of the Woodford Shale based on the geologic framework and thus can improve on the accuracy of well-placement and future exploration activities.

Outline

Like most modern Ph.D. dissertations, this dissertation is structured as a suite of four papers for publication in peer-reviewed journals. Unlike most modern Ph.D. dissertations, this dissertation includes a great deal of proprietary, highly sensitive data. These sensitivities are more economic than scientific, having to do with acreage positions (buying, selling, and forming partnerships) rather than data analysis and interpretation workflows. For this reason, well names, and even absolute well depths, in the hydrocarbon-producing areas are not disclosed. Likewise, while the seismic data have accurate scale and time axes and formation name, they do not exhibit any latitude/longitude information or cultural data.

The Abstract provides a high-level overview of what may seem to be disparate petrophysical, geological, and geophysical components of this thesis spanning scales from the nanometer to the 100-kilometer scale – some 14 orders of magnitude.

Chapter 1, entitled 'An integrated petrophysical characterization of the Woodford Shale in Oklahoma' is accepted by the Society of Petrophysicists and Well-log Analysis.

Chapter 2, entitled 'Microstructural study of shales for evaluating reservoir properties at different thermal maturities' is submitted to the Society of Petroleum Engineers.

Chapter 3, entitled 'Seismic attribute-driven integrated characterization of the Woodford Shale in west-central Oklahoma' will be submitted to Geophysics. Excerpts of this work has been presented at the 2011 International Meeting of the Society of Exploration Geophysicists in San Antonio, and at the 2012 Spring Symposium of the

Rocky Mountain Association of Geoscientists in Denver. Excerpts of this work will also be presented at the 2012 South Texas Meeting of the AAPG

Chapter 4, entitled 'Lithostratigraphic characterization and depositional setting of the Woodford Shale in west-central Oklahoma' will be submitted to the Bulletin of the American Association of Petroleum Geologists. Excerpts of this work has been presented at the 2011 Midcontinent Meeting of the AAPG.

The Conclusion summarizes this integrated piece of work as a whole, underlining the value of analyzing a shale reservoir at multiple scales.

For those who read this dissertation, please excuse the small amount of overlap of figures and references between these separate 'chapters', necessary to make each one 'stand alone'.

Nabinta Gupta, 4-4-2012

Chapter 1

1 Integrated petrophysical characterization of the Woodford Shale in Oklahoma

1.1 Abstract

Heterogeneity of the resource-shale plays and limited knowledge about the shale petrophysical properties demand detailed core-scale characterization in order to understand field-scale measurements that have poor vertical resolution. Analyses of a set of laboratory measured petrophysical properties collected on 300 samples of the Woodford Shale from 6 wells provided an opportunity to track changes in petrophysical properties in response to thermal maturity and their effect on hydrocarbon production. Porosity, bulk density, grain density, mineralogy, acoustic velocities (V_p-fast, V_s-fast and V_s-slow), mercury injection capillary pressure along with total organic carbon content (TOC), Rock-Eval pyrolysis, and vitrinite reflectance were measured. Visual inspections were made at macroscopic-, microscopic- and scanning electron microscope-scale (SEM) in order to calibrate rock-petrophysical properties with the actual rock architecture. Mineralogically, the Woodford Shale is a silica-dominated system with very little carbonate presence. Crossplot of porosity and TOC clearly separate the lower thermal maturity (oil window) samples from higher thermal maturity (wet gas-condensate window) as porosity is lower at lower thermal maturity. Independent observations made through SEM-imaging confirm much lower organic porosity at lower thermal maturity

while organic pores are the dominant pore types in all samples irrespective of thermal maturity. Crack-like pores are only observed at the oil window.

Cluster analyses of TOC, porosity, clay and quartz content revealed three clusters of rocks which could be ranked as good, intermediate and poor in terms of reservoir quality. Good correlations between different petro-types with geological core descriptions, along with the good conformance between different petro-types with production data ascertain the practical applicability of such petro-typing. Petro-types can be upscaled and applied to the uncored interval through calibrating well logs with core measurements. However, limited well-log analyses were performed due to unavailability of log-data.

1.2 Introduction

The Woodford Shale has long been known as the source of most of Oklahoma's hydrocarbon reserves until it emerged as resource play following the huge success of the Barnett Shale play in 2005. Geographically the Woodford Shale play can be grouped into 3 regions: Woodford, Cana-Woodford of the Midwest and Barnett Woodford of the Southwest, with estimated technically recoverable resource as 22.21 TCF, 5.72 TCF and 32.15 TCF respectively (EIA, 2011). This study focuses on an area in the Midwest where the shale is reported to produce dry gas, condensate as well as oil and has an average thickness of 200 ft.

Despite of the economic success, variability in petrophysical parameters controlling reservoir quality is poorly understood and hence, the exploration activities rely heavily on the history matching. This limits the identification of new sweet spots and also expansion of exploration activities outside the proven area. Moreover, unlike

conventional hydrocarbon prospects, resource-shales serve as the source, seal, and reservoir, which make it difficult to identify or rather, define the reservoir unit within this rock. Appropriate petrophysical characterization leads to identification of different petro-types with unique petrophysical properties, which eventually help to identify sweet spots and to decide appropriate areas for well placement. As production from these shales requires stimulation through hydraulic fracturing, appropriate petrophysical models would help to predict hydrocarbon reserve as well as areas/intervals with high "fracability".

Centimeter-scale vertical heterogeneity of resource-shales limits the use of field-scale measurements and misrepresents the petrophysical characterization of such shales to some extent. Petrophysical characterization based on measured petrophysical properties from representative samples of individual litho/petro-type helps to identify and estimate the range of values for parameters which correlates well with reservoir evaluation attributes such as, gas-in-place and fracability, the two important parameters for the resource-shales. Such laboratory-measurements based analyses require a large dataset, which makes the resource-shale characterization time intensive but necessary for the evaluation of resource-shales (Kale, 2009).

Swanson (1981), Thomeer (1960; 1983), Amaefule et al. (1993) etc. have developed and successfully applied different rock typing principles to the conventional reservoirs. All of these rock-typing principles are based on the dynamic range of porosity, permeability and variations in their inter-relationships present in the conventional reservoirs. None of these rock-typing principles can be applied to the resource-shales due to narrow range of porosity and nanodarcy permeability, which are few orders of

magnitude smaller than even tight gas sands (Sondergeld et al., 2010). Moreover, it is also difficult either to measure such low permeability or to estimate permeability from porosity-permeability relationship previously observed by Swanson (1981), Thomeer (1960, 1983) etc. Klinkenberg correction becomes significant at this low permeability, which lead to the erroneous estimation of permeability (Kamath, 1992). Gunter et al. (1997) defined petro-types as "units of rocks deposited under similar geological conditions, undergone similar digenetic processes resulting in unique porosity – permeability relationships, capillary pressure profile and water saturations above free water." Such petro-types are unique geologically and petrophysically and ideally helpful in delineating good reservoir rocks from poor for any kind of reservoir rocks. However, it still relies heavily upon porosity and permeability, which limits its use for the resource-shales.

Despite of all the difficulty, rock typing can be an important tool for the evaluation of resource-shales if the petro-types can capture subtle differences in petrophysical properties that may influence production. Sondergeld et al. (2010) documented a set of petrophysical properties (rock composition, total organic carbon content, porosity, saturation, permeability and mechanical properties) impacting the performances of resource-shales. Newsham and Rushing (2001) tried to follow the rock typing principles of Gunter et al. (1997) and proposed a specialized workflow for the evaluation of unconventional reservoir and applied that for the evaluation of tight-gas sandstone; the workflow is named it as "modified PIPM." They defined rock-types in three ways, such as: depositional, petrographic and hydraulic. This rock typing workflow has limited practical applicability, as it is difficult to correlate these three petro-types with

one another. Jacobi et al. (2008) proposed a workflow for integrated petrophysical evaluation of shale gas reservoirs; they called it as "expert system." This workflow is focused on the petrophysical evaluation based on well logs and used limited core data, which may not work always, owing to the high variability typical of resource shales. Kale (2009) proposed a core measurement based rock typing workflow for the Barnett Shale. Passey et al. (2010) made an effort to integrate petrophysical and geological characterization of resource shales.

1.3 Study area

The Woodford Shale was deposited in the palaeo-Oklahoma Basin covered by an epeiric sea, during global sea-level transgression (Lambert, 1993; Johnson, 1988) (Figure 1.3-1). Different petro-types are expected in different parts of the sea (horizontal variability) as well as in different stages of the transgression (vertical variability). Sub-surface cores collected from 6 wells located in both hydrocarbon producing and non-producing areas (approximately 1440 square miles) were used for this study (Figure 1.3-2). Thermal maturity of the Woodford Shale in wells 1, 2, 3, and 6 are within dry gas-condensate maturity window whereas wells 4 and 5 are within oil window. Samples are collected from ~200 feet long continuous cores acquired from wells 1 through 3. For well 4, 5, and 6 samples are collected from cores at discrete depth intervals.

About 300 samples are collected after careful visual inspection of the subsurface cores. Samples are collected at every 2-foot interval in apparently monotonous interval while intermittent samples are collected at places with visual-changes in lithology. At this point it is worth mentioning that sometime it is possible to miss some of the lithologic changes due to dark color of the rock. Sharp changes in petrophysical

properties along with inspection of microscopic properties is used in tracking such significant but apparently invisible lithologic changes.

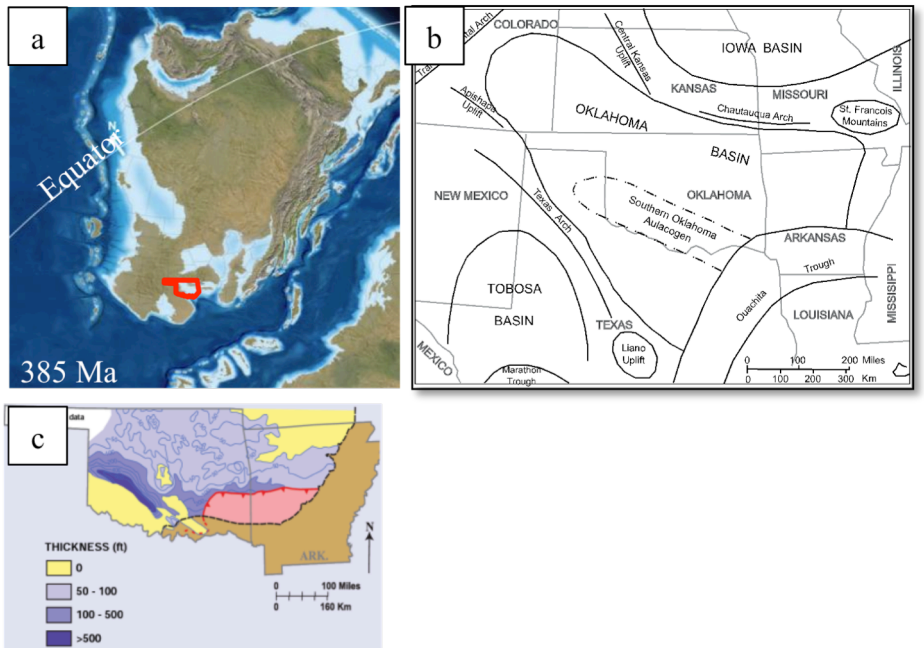

Figure 1.3-1: (a) Paleogeography of North America at the beginning of late Devonian (Frasnian). Paleo-location of Oklahoma is marked with red line. Figure is modified from Comer, 2008. (b) Location of the Oklahoma Basin covering a vast area of the Southern Midcontinent during Late Devonian-Early Mississippian time. Oklahoma Basin was later broken into a number of sub-basins due to tectonic activity. Map modified from Johnson, 1988. (c) Isochore map of the Woodford Shale in Oklahoma. Map modified from Comer, 2008.

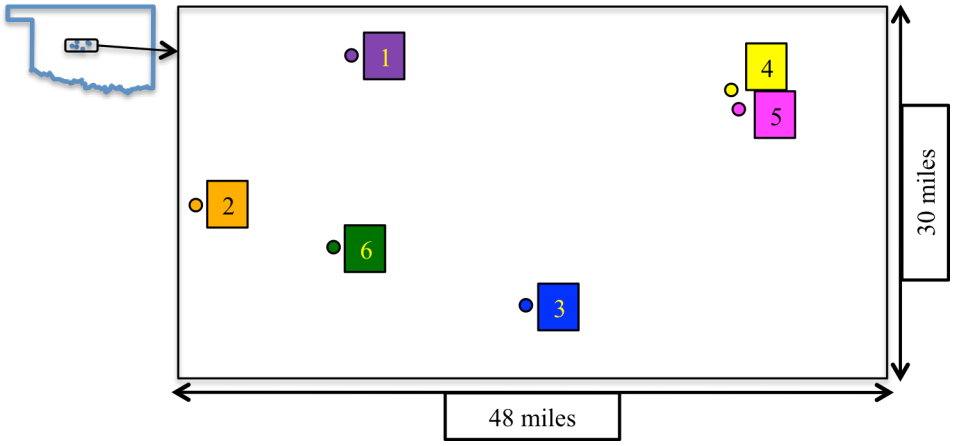

Figure 1.3-2: Location of the six cored wells considered in this study.

1.4 Laboratory Measurements

A set of petrophysical properties impacting two reservoir assessment categories: storage capacity and flow capacity are measured: (i) crushed rock porosity (Φ), (ii) bulk density (ρ_b), (iii) grain density (ρ_g), (iv) mineralogy through transmission Fourier Transform Infra-Red spectroscopy (FTIR), (v) acoustic velocities (V_p-fast, V_s-fast and V_s-slow), (vi) total organic carbon (TOC) content, (vii) Rock-Eval analyses and (viii) mercury injection capillary pressure (MICP) along with microscopic and sub-microscopic inspection of samples through (ix) petrographic microscopic analyses of thin sections, and (x) scanning electron microscopic (SEM) analyses of focused ion beam (FIB) or broad-beam milled samples. Nuclear magnetic resonance (NMR) measurements have been performed on few samples to gain knowledge about shale wettability. Most of these measurements are made at the Integrated Core Characterization Centre (IC^3) at the University of Oklahoma while the organic content (TOC) and Rock-Eval measurements are made at a commercial laboratory. Dynamic elastic moduli calculated from ultrasonic acoustic velocities provide indirect estimates for rock-mechanical characteristics.

Detail descriptions of how the petrophysical properties are measured can be found in the following references:

- Φ, ρ_b, and ρ_g in Karastathis (2007), Kale (2009)
- FTIR in Ballard (2007), Matteson and Herron (1993), and Sondergeld and Rai (1993)
- Ultrasonic velocities in Birch (1960), Raina (2010), and Schreiber et al. (1973)
- MICP in Kale (2009)

Crushed rock porosity (Φ): Represent the total porosity of shales and include the free and capillary bound pore spaces but exclude the spaces occupied by clay bound water.

FTIR mineralogy: The system is set up to identify sixteen common rock forming minerals which are grouped into 5 mineral groups as shown in Table 1.4-1.

Ultrasonic measurements: For the current study ultrasonic measurements are performed on horizontal plug. One compressional (V_p-fast) and two orthogonally polarized shear wave velocities (V_s-fast and V_s-slow) are measured, as shown on Figure 1.4-1. Core plugs are subjected to increasing confining pressure from 250 psi to 5000 psi in eight steps and ultrasonic data is collected at each step using ultrasonic pulse transmission technique.

Minerals	Mineral Groups
Quartz	Quartz
Albite	Total Feldspar
Orthoclase Feldspar	
Oligoclase Feldspar	
Calcite	Total Carbonates
Dolomite	
Siderite	
Aragonite	
Chlorite	Total Clays
Illite	
Smectite	
Kaolinite	
Mixed Clays	
Anhydrite	Others
Apatite	
Pyrite	

Table 1.4-1: Minerals identified in FTIR.

MICP: Along with the capillary pressure, pore throat diameter can be calculated from this measurement, using Washburn equation.

$$r=\frac{2\gamma k\cos\theta}{P_{cap}}$$

Where, P_{cap} = capillary pressure (psi), γ = interfacial tension, 480 dyne/cm for mercury, k =0.145, and θ = contact angle, 140° for mercury, and r = pore throat radius (μm). Hence, knowing the pressure at which intrusion takes place we can calculate the

pore throat radius. For example, at 60,000 psi mercury enters pores with throat diameters of 3 nm.

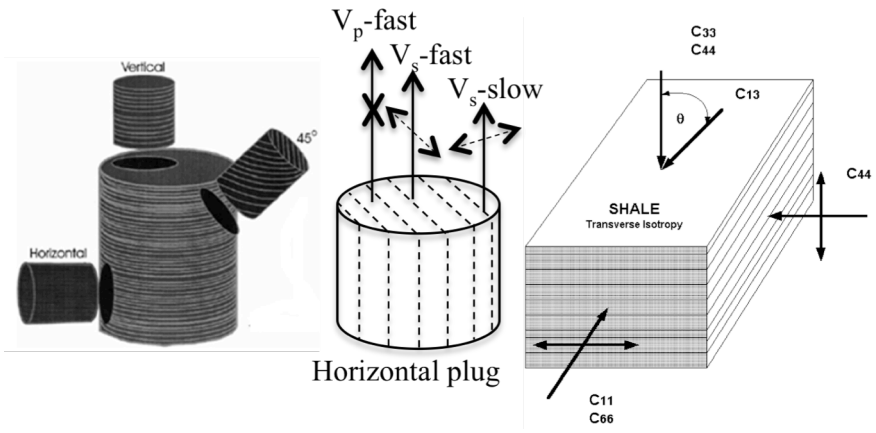

Figure 1.4-1: Schematic diagram showing the orientation of core plug. V_p-fast and V_s-fast are fast compressional and shear wave velocities. V_s-slow is the slow shear where the particle movement is perpendicular to the bedding and the wave is travelling parallel to the bedding. The schematic on the right shows the principal directions and the required elastic constants for anisotropic characterization of the shales.

1.5 Results

Table 1.5-1 summarizes the distribution of the laboratory measured petrophysical properties.

Porosity: Φ varies between 0% and 10% in the studied wells. Φ shows a normal distribution, especially when wells with high organic maturity are considered. Porosity of wells within oil window belongs to a different normal distribution. Φ ranges between 2%

and 10% with 6% average in high maturity wells (wells 1, 2, 3, and 6), and ranges between 3% and 5% with 1.6 % average in wells within oil window (wells 4 and 5).

Density: Bulk density varies between 2.2g/cm^3 and 2.9g/cm^3 with 2.4g/cm^3 average. Grain density varies between 2.4g/cm^3 and 3g/cm^3 with 2.6g/cm^3 average.

Mineralogy: Figure 1.5-1 summarizes the mineralogy in Table 1.4-1. Individual mineral weight percentages from wells 1 through 6 located in different parts of the basin show overall narrow spread (Figure 1.5-1a, and b) while quartz and illite show comparatively wider spread (Figure 1.5-1a). Despite the narrow range in mineralogy, depth plots show strong mineralogical variations with depth (Figure 1.5-1c) in wells 1 through 3. For example, well 3 has higher clay concentration compared to well 1 and 2, clay concentration decreases notably upward in well 2.

Ternary plots indicate that the Woodford Shale is a silica-dominated system with <20% carbonate except for a few samples (Figure 1.5-2a). The highly calcareous samples are located near the boundary of the Woodford Shale and the underlying Hunton Limestone. Figure 1.5-1a also shows that wells 3 and 4 are more clayey compared to well 1 and 5 while well 2 has a wider range in clay concentration. Overall, clay percentage varies between 20% and 70%. Clays are dominantly illite with some mixed clays and little to no kaolinite (Figure 1.5-1b). Dolomite and siderite are the dominant carbonate minerals with <40% calcite (Figure 1.5-1c). Two dominate minerals: quartz and total clays are inversely proportional to each other (Figure 1.5-1d).

a

Properties	Well 1	Well 2	Well 3	Well 4	Well 5	Well 6
	No. of samples	No. of samples	No. of samples	No. of samples	No. of samples	No. of samples
Φ	85	17	76	9	11	2
ρ_b	85	17	76	9	11	2
ρ_g	85	17	76	9	11	2
Mineralogy	85	17	76	9	11	2
Velocity	34	N/A	50	N/A	N/A	N/A
TOC	85	15	71	9	11	2
Rock Eval	85	15	37	9	11	2
MICP	45	16	47	6	5	2

Table 1.5-1: (a) Summarizes number of samples used for laboratory measurements, (b) Summary of laboratory measured petrophysical properties for the studied wells.

b

Properties		Well 1		Well 2		Well 3		Well 4		Well 5		Well 6	
		Range	Average	Range	Average	Range	Average	Range	Average	Range	Average	Range	Average
Φ_{He} (%)		4-8.5	6	3-8	6	4-8.5	6	0-4.3	3	2.5-5	3.4	6-8	7
ρ_b (g/cm^3)		2.2-2.65	2.4	2.33-2.7	2.52	2.2-2.7	2.43	2.35-2.54	2.45	2.33-2.45	2.4	2.55-2.56	2.56
ρ_g (g/cm^3)		2.4-3	2.56	2.5-2.8	2.67	2.4-3	2.59	2.39-2.6	2.5	2.39-2.56	2.45	2.69-2.76	2.72
Velocity (km/s)	Vp-fast	3.7-6.35	4.8	N/A	N/A	4-5.7	4.8	N/A	N/A	N/A	N/A	N/A	N/A
	Vs-fast	2.35-3.9	3.03	N/A	N/A	2.6-3.85	3	N/A	N/A	N/A	N/A	N/A	N/A
	Vs-slow	2.2-3.76	2.59	N/A	N/A	1.99-3.7	2.39	N/A	N/A	N/A	N/A	N/A	N/A
TOC (wt.%)		0-9	5.4	0-7.7	2.88	0-13	5.5	5.2- 10	7.2	2.9-7	6	0.7- 1.24	0.37

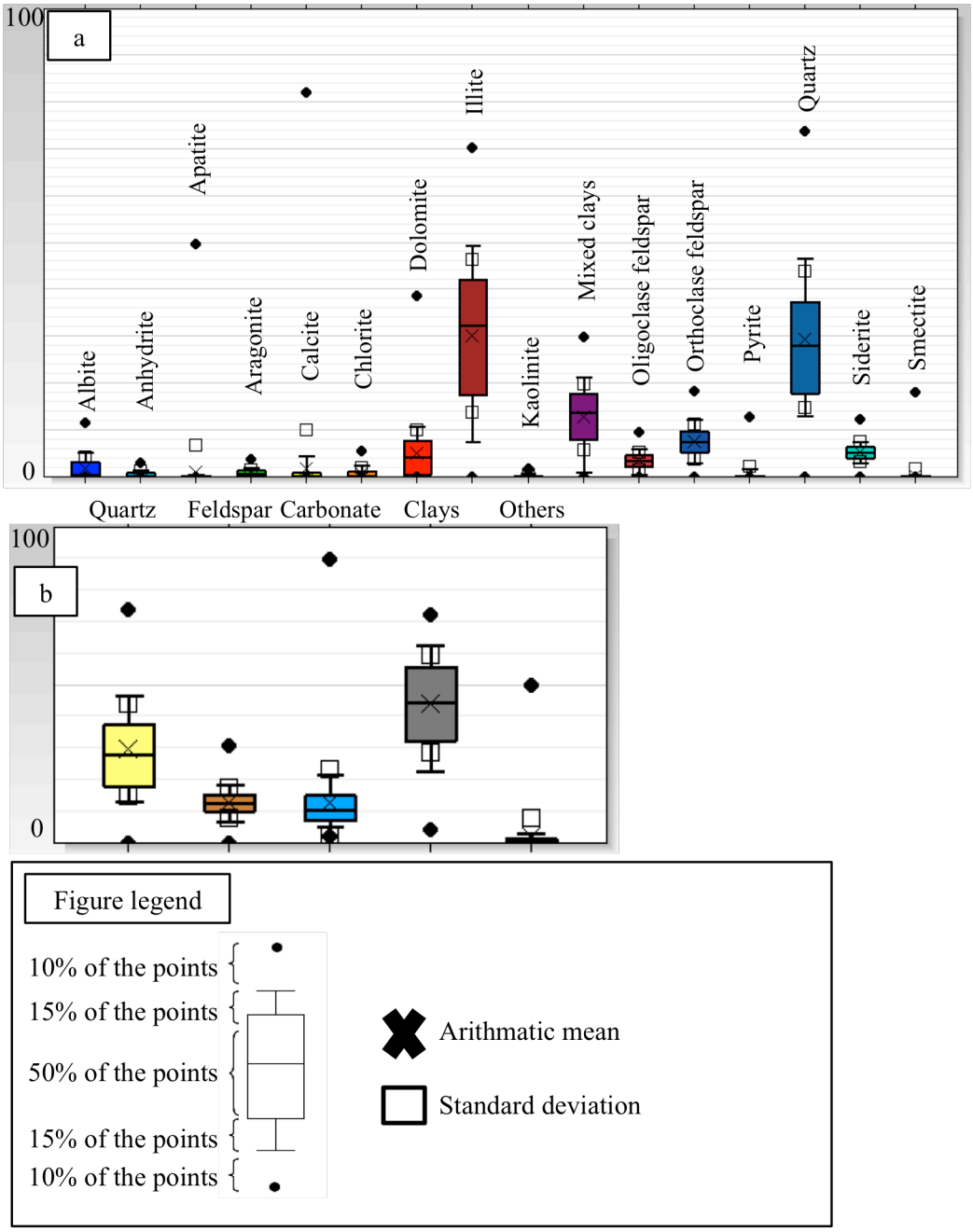

Figure 1.5-1: Box-and-whisker plots showing distributions of different minerals measured through FTIR (a). Distributions of 5 group of minerals mentioned in Table 1.4-1 (b). (c) Mineralogic variations with depth for well 1, 2, and 3. (d) Crossplot of the two dominant minerals: quartz and clays in the studied wells 1 through 6 indicate that these two parameters are inversely related.

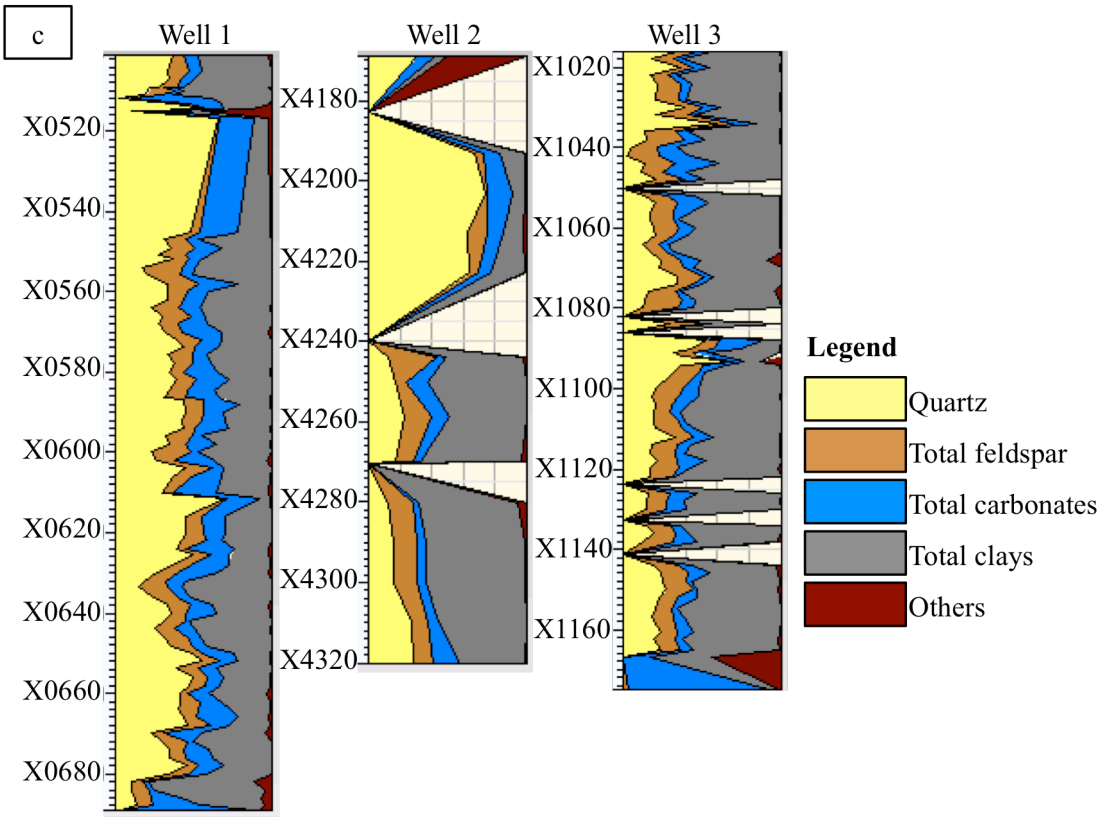
c
Well 1
Well 2
Well 3
X0520
X0540
X0560
X0580
X0600
X0620
X0640
X0660
X0680
X4180
X4200
X4220
X4240
X4260
X4280
X4300
X4320
X1020
X1040
X1060
X1080
X1100
X1120
X1140
X1160
Legend
Quartz
Total feldspar
Total carbonates
Total clays
Others

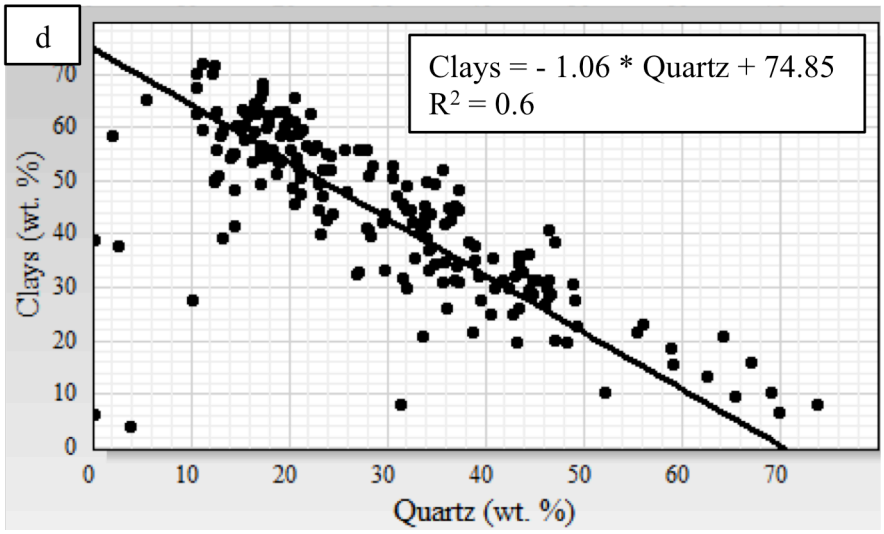
d
Clays = - 1.06 * Quartz + 74.85
R2 = 0.6
Clays (wt. %)
Quartz (wt. %)
0
10
20
30
40
50
60
70

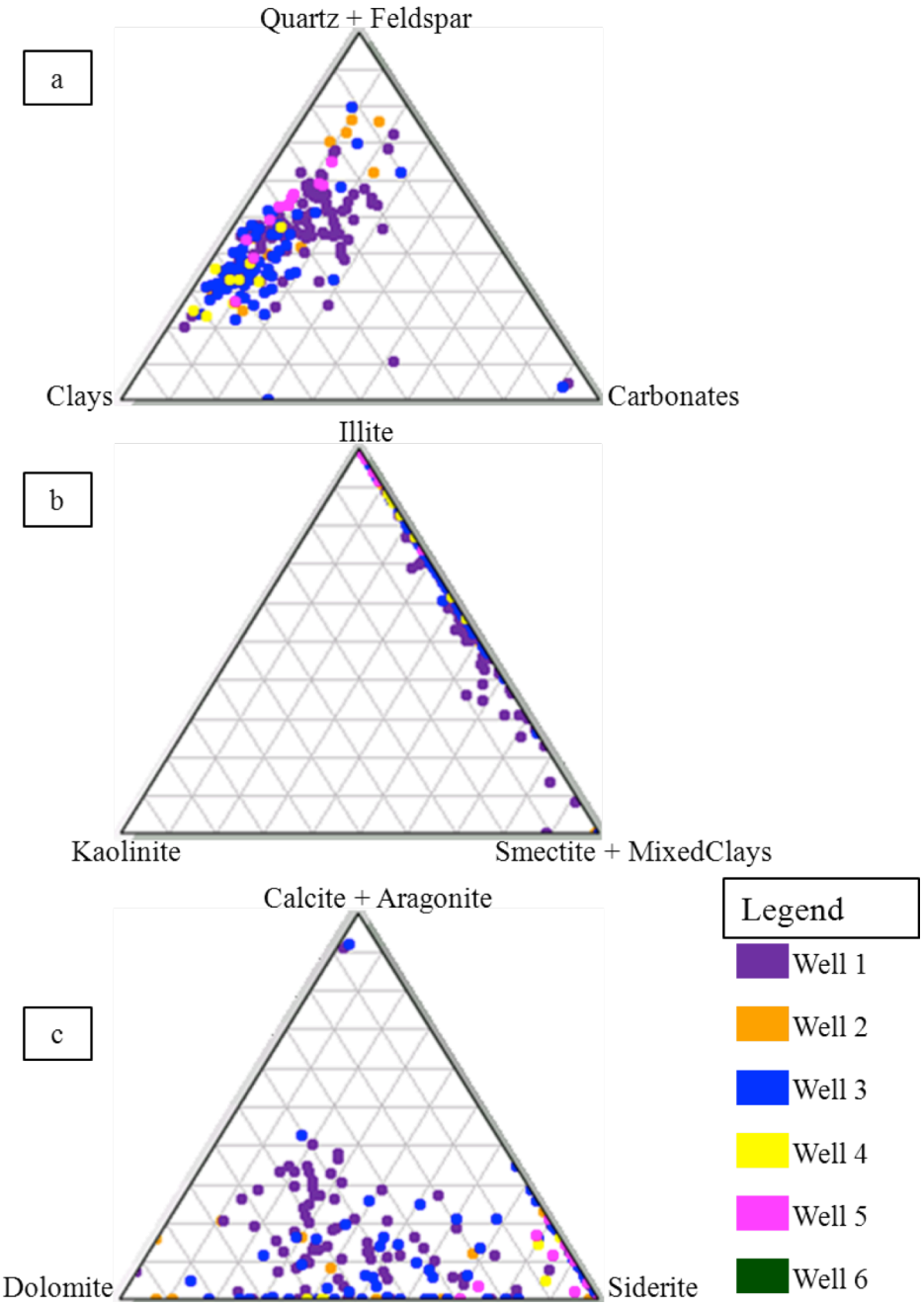

Figure 1.5-2: Ternary plots showing distributions of (a) quartz+feldpar, clays, and carbonates. Note, the Woodford is a silica-dominated system with little carbonate. Total carbonate is <20% except for few samples, (b) distributions of different clay minerals, and (c) distributions of different carbonate minerals.

Ultrasonic measurements: Acoustic velocities are measured on horizontal core plugs at native state from wells 1 & 3, as core plugs required for the ultrasonic velocity measurement could be recovered from the two wells only. 84 velocity measurements are performed. The ranges and averages for V_p-fast, V_s-fast and V_s-slow are 3.7 km/s to 6.35 km/s and 4.79 km/s, 2.35 km/s to 3.91 km/s and 3.01 km/s, 1.3km/s to 3.76 km/s and 2.48 km/s, respectively. Ultrasonic velocities show little pressure dependence (Figure 1.5-3). Small increase in velocity at low confining pressure (P_c) is most likely due to closures of desiccation cracks. Such characters are observed specially in samples with higher clay concentration.

It was not possible to obtain 3 sets of plugs (horizontal, vertical and 45°) required to measure 5 independent elastic moduli which are needed to fully define the characteristic transverse anisotropy of shales. The fine-scale heterogeneity poses a problem to acquire equivalent core plugs with different orientation and also samples are always biased toward the more competent strata. However, the anisotropic parameter, γ can be calculated using the orthogonally polarized shear wave velocities. The V_p-fast can be compared to V_p collected in a vertical borehole in order to calculate another anisotropic parameter, ε.

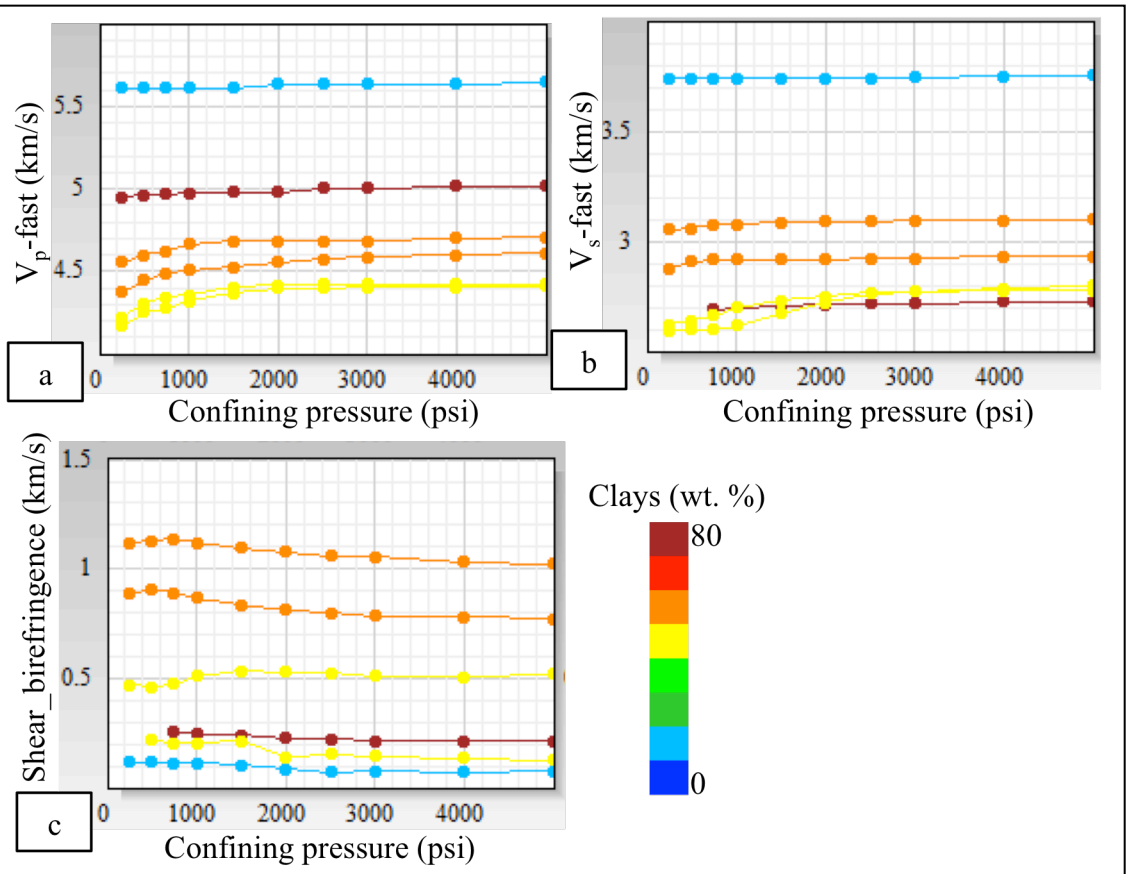

Figure 1.5-3: Crossplots of ultrasonic measurements and confining pressure. Data are colored with clay content. (a, b) Both compressional- and shear-wave velocities (V_p-fast and V_s-fast) exhibit weak dependence on pressure. Note, small increase in velocities (primarily compressional) at low confining pressure for samples with higher clay concentrations. (c) Plot showing shear wave birefringence increases with increasing clay content.

TOC: Total organic carbon (TOC) ranges between 0 wt.% and 14 wt.%. Such concentration of TOC indicates a significant volume fraction of the rock since the density of organic matter ($1 g/cm^3$) is much lower compared to common rock forming minerals (Sondergeld et al., 2010). This implies that the petrophysical properties of organic matter significantly affect the overall rock petrophysical properties. Moreover, SEM imaging

has revealed high porosity within organic matter, which even increases the volume of organic matter for a given TOC weight percent (Chapter 2 of this dissertation).

Rock-Eval analyses: Rock Eval has been performed on 150 samples. In this experiment, organic matter is pyrolized with step increases in temperature. The amplitudes of S1, S2 and S3 peaks recorded in this experiment are representative of liquid hydrocarbons present in the rock, the amount of convertible kerogen, and the amount of inorganic carbon dioxide released, respectively. The temperature for the highest S2 peak represents thermal maturity (T_{max}). Average T_{max} for studied wells 1 through 5 are: 467°C, 458°C, 466°C, 439°C and 441°C and equivalent R_o are: 1.25%, 0.99%, 1.23%, 0.74% and 0.78%. T_{max} is converted to equivalent vitrinite reflectance value through equation: R_o (%) = (0.0180*T_{max})-7.16 (Espitalie, 1986). For wells 1, 2 and 3, S2 peaks are either too low or form a plateau and lack any peak (characteristics of high thermal maturity) (Figure 1.5-4) and hence, limited confidence should be given to S2 values and T_{max} derived from this S2 peak. Also quantitative use of these parameters should be limited. Measured R_o for well 1 through 6 are: 1.62%, ~1.6%, 1.67%, 0.54%, 0.54% (Comer, personal communication). Jarvie (1991) mentioned that for high maturity samples microscopic estimation of R_o is more reliable than Rock-Eval analyses. However, such measurements should be made by the same person in order to reduce human error.

Both vitrinite reflectance and average T_{max} values indicate that wells 1 through 3 and 6 are in condensate-wet gas window and wells 4 and 5 are in the oil window; however, over a 300 ft interval (average thickness of the Woodford Shale in the study area) thermal maturity may vary significantly. Figure 1.5-5 indicates that wells 4 and 5

have type II kerogen whereas the high maturity wells fall near the origin and shows a wide range of kerogen type; this plot represents the present day organic matter type. Jarvie et al. (2007) documented that thermal maturity as well as expulsion of hydrocarbon from rocks affect the chemical composition of kerogen and make it difficult, if not impossible, to recognize original kerogen type in highly mature samples. Since, low maturity samples are plotted as type II, starting material for the highly maturity samples are also interpreted to be type II. The facts that type II kerogen results primarily from marine source and the wells 4 and 5 are located near-shore compared to wells 1,2, 3 and 6 which are located deeper marine, further suggest that starting organic matter in the studied wells is type II. Overall, the wells are grouped into two ranges of maturity: highly mature (wells 1, 2, 3 and 6) and low mature (wells 4 and 5). Original kerogen type has been interpreted as type II.

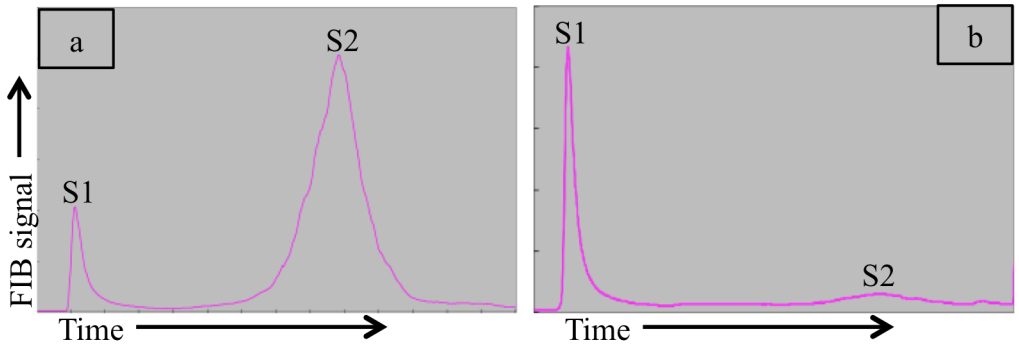

Figure 1.5-4: (a) Pyrogram of a sample from well 4, showing distinct S1 and S2 peaks, respectively from left to right. (b) Pyrogram from high maturity sample in well 1. Note, the low S2 peak in Figure b.

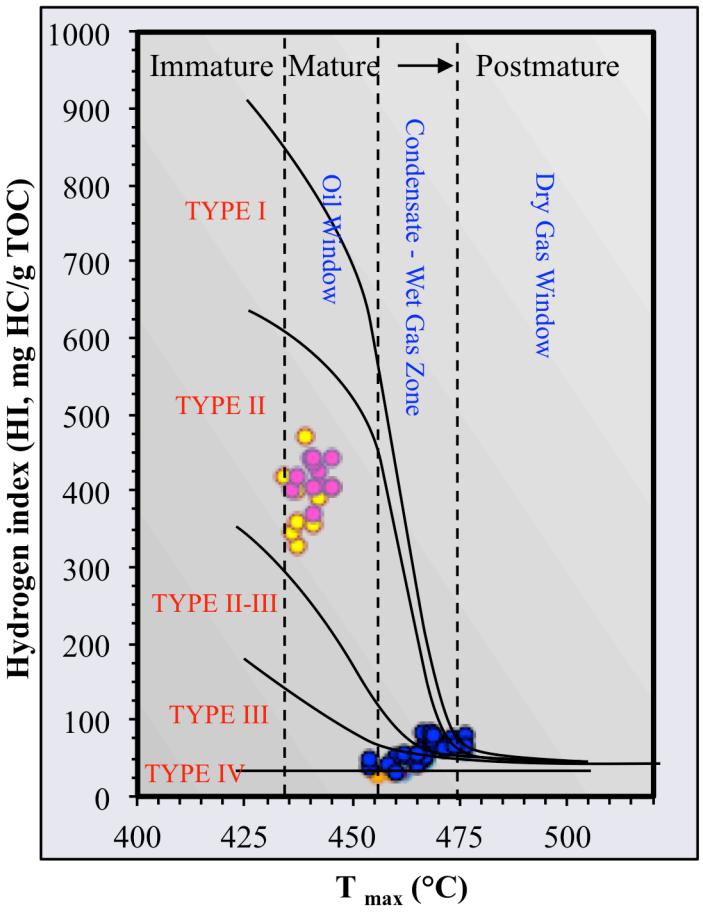

Figure 1.5-5: Crossplot of Hydrogen index (HI) and T_{max}. Wells 1 through 3 and 6 are at higher maturity level compared to wells 4 and 5. HI is calculated using the following formula: S2*100/TOC, mg HC/g TOC.

Mercury injection capillary pressure (MICP): MICP measurements show absolutely no mercury intrusion below 10,000-psi confining pressure, indicating pore throats are smaller than 0.01µm. This is equivalent to a matrix permeability of few 100's of nanodarcy. Lack of representative sample, appropriate for applying conformance correction to the shale sample (Sigal, 2009) limits the quantitative use of MICP data. This is why emphasis has been placed on analyzing the shape of the capillary pressure curve,

even though Hg injection measurement provides an estimate of the connected pore space. Different shape of the capillary pressure curve represents different pore throat distributions, different pore throat diameters etc. and have been used for rock typing.

1.6 Discussions

Like any other petroleum system porosity (Φ) is directly related with storage capacity. The concentration of organic matter (TOC) not only affects potential volume of hydrocarbon present within the system but also hosts pores and thus improves the storage capacity also. However, there is no tool to directly measure either porosity in shale or TOC in field-scale and it is impossible to collect core or laboratory data from each well. Here we evaluate any correlation between these two properties and other petrophysical properties such that closely associated parameters can be used to indirectly estimate porosity and TOC.

Crossplot of TOC and Φ shows porosity increases with TOC (Figure 1.6-1). Correlation between TOC and porosity improves when wells with similar thermal maturities are considered. Overall, samples with lower thermal maturity (wells within oil window) have lower Φ compared to samples with higher thermal maturity (wet gas–condensate window). More pore space is created within organic matter as more and more hydrocarbon is expelled with increasing thermal maturity. Good correlation between TOC and porosity is supported by the fact that organic pores are the dominant pore types in this resource shale, as observed through SEM imaging (Chapter 2 of this dissertation). Previous authors (Curtis et al., 2011; Loucks et al., 2009; Passey et al., 2010; Sondergeld et al., 2010b) have observed organic pores as the most dominant pore types in other resource shales as well. Although we speculate that overall porosity increases with

thermal maturity, SEM imaging has revealed a more complex nature to this porosity development. Mechanism behind the formation of such organic pores is discussed later.

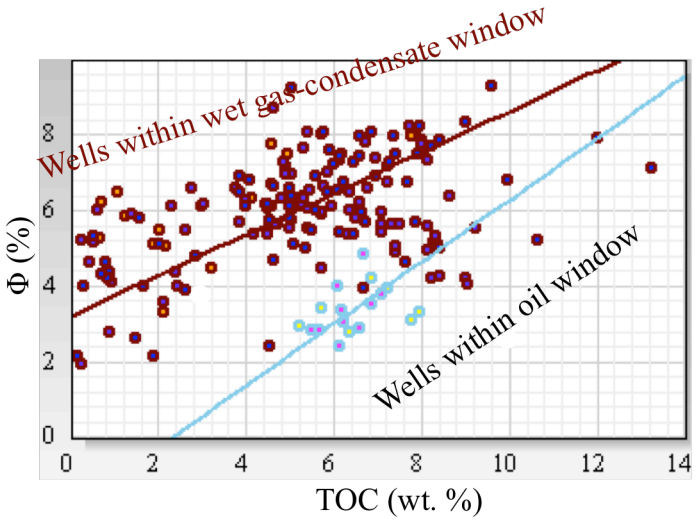

Figure 1.6-1: Crossplot of core porosity (Φ) and TOC indicates good correlation between these two parameters. Red circles represent data from high thermal maturity wells (wells 1, 2, 3, and 6). Cyan points are from low thermal maturity wells (wells 4 and 5). Equations for the red and cyan regression lines, fitted to red and cyan points are: Φ = 0.54 * TOC + 3.22; Φ = 0.83* TOC - 1.98.

Crossplots of porosity and mineralogical composition reveal complex relations between porosity and the two dominate minerals: quartz and total clays. Crossplot of Φ and clays indicates overall increasing Φ with increasing clay concentration (Figure 1.6-2). Similar correlation has been observed in the Barnett Shale (Kale, 2009) and 13 Finger (Raina, 2010). A closer look at the crossplot of porosity and clay indicates two clusters: (i) rocks with clays<42%, where porosity increases with increasing clay concentration, and (ii) clay concentration>42%, where porosity decreases with increasing

clay concentration. The first group of rocks is also characterized by overall high quartz concentration compared to the second group. Crossplot of porosity and quartz (Figure 1.6-3) apparently does not indicate any correlation. Correlation between porosity and quartz improves when data is broken into two clusters: (i) rocks with quartz<40% where porosity increases with quartz, and (ii) rocks with quartz>40% where porosity decreases with increasing quartz.

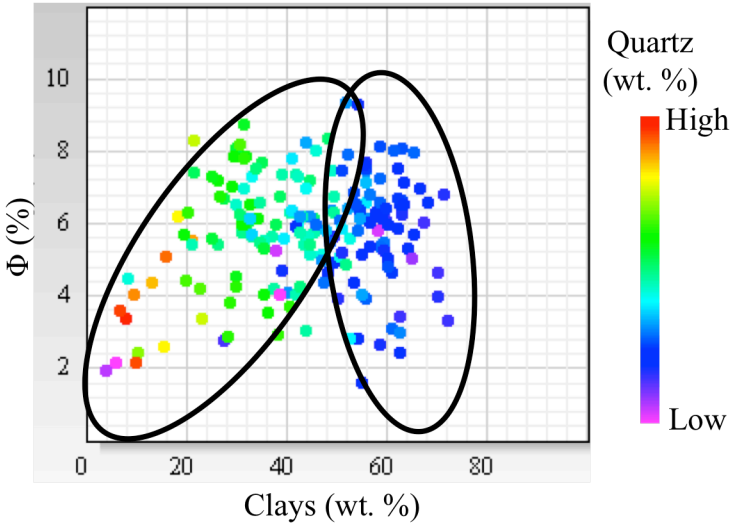

Figure 1.6-2: Crossplot of core porosity (Φ) and total clays. Data is colored with quartz content (wt. %). Data bounded by two ellipses indicate two clusters. The cluster with higher clay concentration is characterized by low quartz concentration and the other cluster with lower clay concentration is characterized by higher quartz concentration.

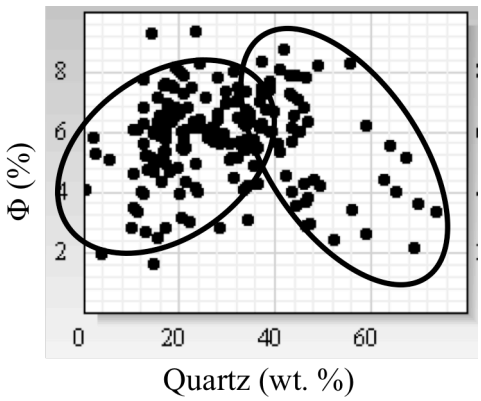

Figure 1.6-3: Crossplot of core porosity (Φ) and quartz. Crossplot exhibits two clusters of rocks as indicated by two ellipses. Φ increases with increasing quartz for quartz<40% and decreases with increasing quartz for quartz>40%.

In general TOC increases with increasing clay content as observed by previous authors (Kale, 2009; Raina, 2010) in other resource shales. Crossplot of TOC and clays (Figure 1.6-4a) however reveals more subtle trends between these two parameters for the Woodford shale. The crossplot indicates three clusters with unique correlations between these two parameters: (i) Rocks with both low clay (0 wt.%<clays<24 wt.%) and low TOC content. TOC has no dependency on clay for this group. (ii) Rocks with clay concentration ranging between 8 wt.% and 48 wt.% where TOC exhibit an increasing trend with increasing clay content. (iii) Clay rich rocks (clays>44%), this group of rocks has a wide range of TOC (0%-14%). TOC does not show much dependence on clay content for this group as well. Crossplots of TOC and quartz shows apparently poor correlation between these parameters; correlation improves when the data is broken into three clusters (Figure 1.6-4b): (i) rocks with quartz<25 wt.%, where TOC shows loosely increasing trend with increasing quartz content. This group is also characterized by high

clay content. (ii) For rocks with 24 wt.%<quartz<58 wt.%, TOC shows increasing trend with increasing quartz content. This group is also characterized by intermediate clay content. (iii) Rocks with high quartz content (quartz>58 wt.%), TOC decreases with increasing quartz concentration. Overall TOC is low in this group of rocks. This group of rocks is representative of the characteristic cherty facies of the Woodford Shale (Chapter 4 of this dissertation, Hoeve et al., 2011). This group of rocks contains low clay content.

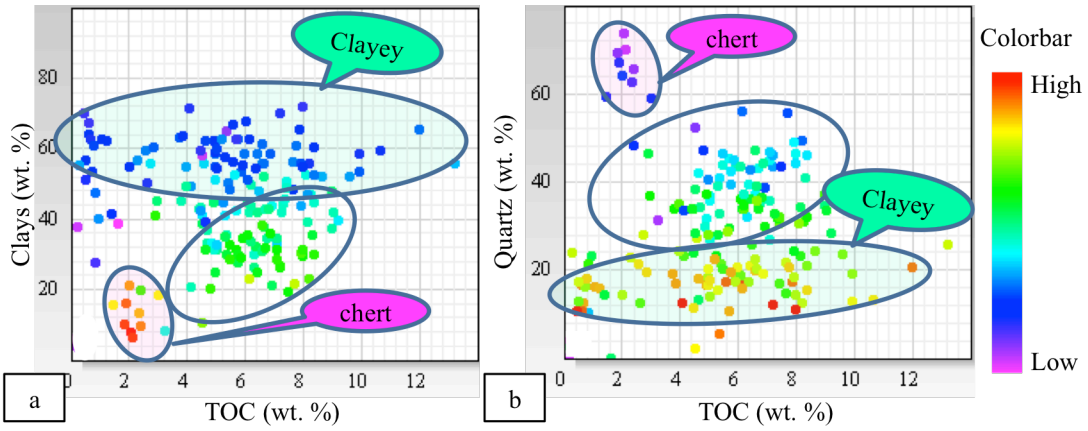

Figure 1.6-4: Crossplot of TOC and (a) clays, (b) quartz. Data is colored with quartz and clay content in figure a, and b respectively. Crossplots indicate more than one cluster of data as bounded by the ellipses.

TOC does not have any correlation with total carbonate, which is obvious, as the geologic history indicates silica-shelled organisms dominated the Woodford Sea (Chapter 4 of this dissertation; Lambert, 1993; Sullivan, 2006). These silica-shelled organisms along with marine algae (Tasmanities for example) are the source of TOC in the Woodford Shale. Carbonate shelled organisms had limited existence in the study area (Comer, 2008; Chapter 4 of this dissertation; Sullivan, 2006). Primary source of carbonate was detrital (Comer, 2008) along with some diagenetic dolomite and aragonite

which formed as bi-product of bacterial activity in the upper few centimeter of sediment column (Chapter 4 of this dissertation).

Geologic history of the study area indicates two sources of silica: biogenic and detrital (Geology paper, Caldwell, 2011). For the group of samples with intermediate clay and quartz content (8 wt.%<clays<48 wt.% and 24 wt.%<quartz<58 wt.%), increasing trends of TOC with increasing quartz content indicate possible biogenic silica enrichments in this group. Increasing quartz content also increases the brittleness (Sondergeld et al., 2010a) of this group.

Dynamic elastic moduli calculated from acoustic velocities provide an indirect estimate of elastic moduli. In this study, ultrasonic velocities are measured on horizontal core plugs collected from two wells (well 1 and 3). Crossplots of ultrasonic velocities, elastic moduli with other petrophysical indicate that both both Vp and Vs vary inversely with porosity and TOC. Young's modulus (E) varies inversely with TOC, specially for samples with E<60 GPa and TOC>4% (Figure 1.6-5).

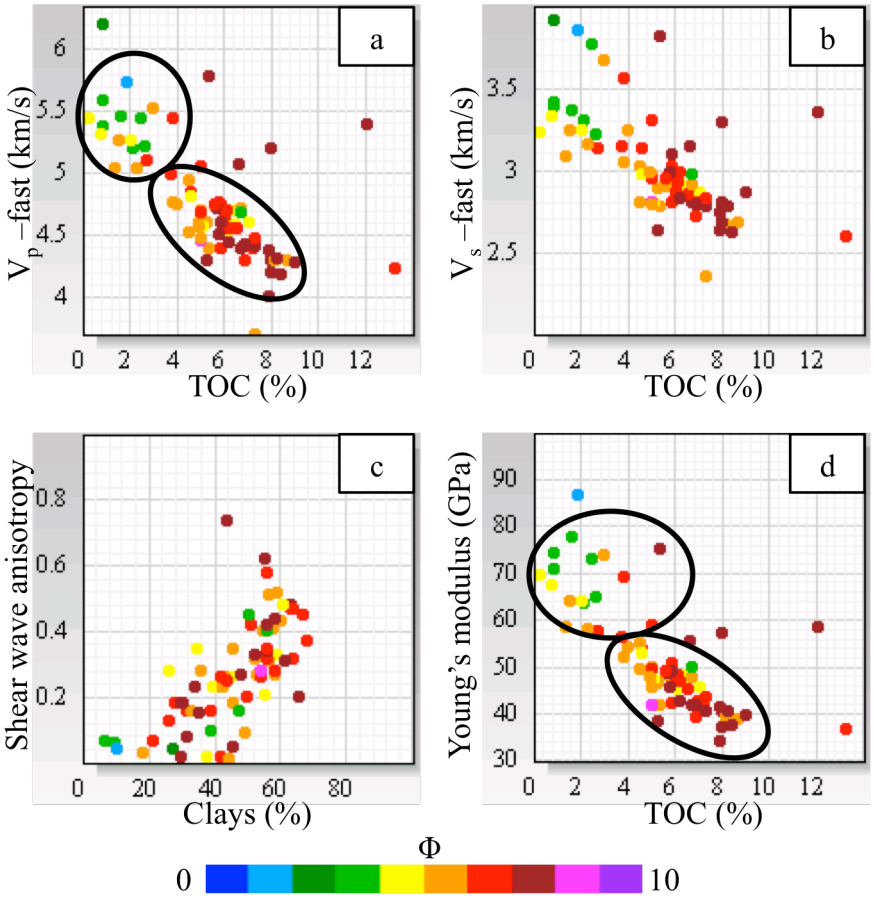

Figure 1.6-5: Crossplots of V_p-fast and V_s-fast with TOC, shear wave anisotropy and clay, and Young's modulus and TOC. Black circles indicate possible different petro-types holding unique correlation between different petrophysical parameters. Data are colored with Φ, as shown on the color bar.

Combination of Young's modulus and Poisson's ratio is often used to define brittleness of rocks such that rocks with high Young's modulus and low Poisson's ratio are brittle, and hence, are "fraccable" compared to rocks with low Young's modulus and high Poisson's ratio which are considered as ductile (Rickman et al., 2008). For the Woodford Shale, Poisson's ratio varies between 0.05 and 0.16, V_p-fast/V_s-fast ranges between 1.4 and 1.65 while Young's modulus varies between 36 GPa and 80 GPa for

horizontal samples. Due to such narrow range of both Poisson's ratio and V_p/V_s the brittleness of the Woodford Shale is dictated by the Young's modulus.

Detailed core description of well 3 reveals that only layer bound natural fractures are present in two intervals where some siliceous laminae/cherty layers are present with alternate mudstone facies (Figure 1.6-6). Although it was not possible to collect plugs and ultrasonic measurements from the thin brittle layers, mineralogy data confirms high quartz content of those siliceous layers.

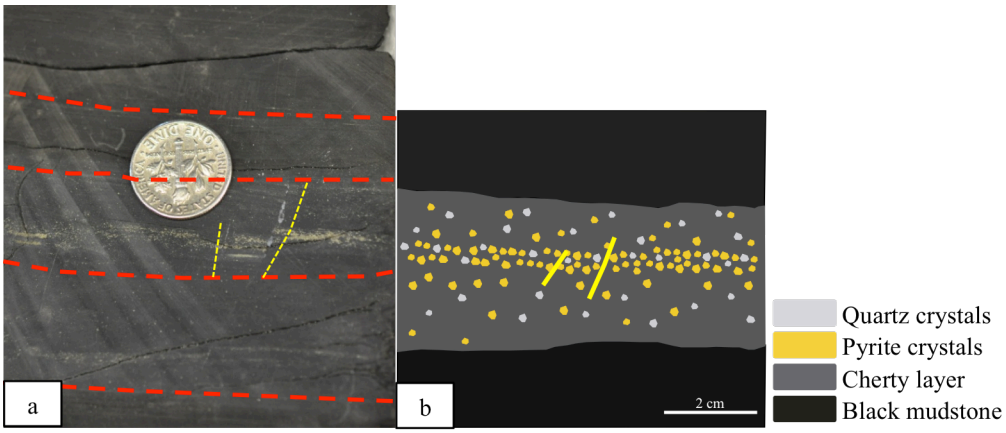

Figure 1.6-6: (a) Core sample from well 3 showing small-scale faulting bounded within the brittle layer. Red dashed lines indicate the boundaries between more brittle (central interval), less brittle and ultimately to the black mudstone, yellow lines indicate vertical fractures bounded within the brittle layer. Dime is kept for scale. (b) Schematic representation of picture a.

1.7 Mechanism for organic-pore development

SEM imaging analysis enabled me to make visual inspection of organic and other pore-types. SEM imaging of samples with thermal maturity varying from oil window (R_o 0.7%) to post-mature wet gas condensate window (Ro 1.72%) allowed me to investigate porosity development with increasing thermal maturity. Figure 1.7-1, Figure 1.7-2a and

1.7-2b shows examples of organic pores at different thermal maturities indicating very little porosity in low thermal maturity samples (Figure 1.7-1a and Figure 1.7-2a) and significant porosity in organics of high thermal maturity samples (Figure 1.7-1b and Figure 1.7-2b). This is consistent with the overall increase in porosity with increasing thermal maturity (Figure 1.6-1). However, SEM images of some samples with low thermal maturity (R_o 0.7%) reveal high organic porosity (Figure 1.7-2c, and d) indicating a more complex mechanism is behind the formation of such pores.

SEM imaging indicate that although more organic pores are developed with increasing thermal maturity; such increase in porosity is not a simple function of thermal maturity. A possible mechanism for the formation of organic pores is discussed as follows. Jarvie (1991) documented three forms of organic carbon such as: (i) extractable organic carbon (EOM), (ii) convertible carbon, and (iii) residual carbon. We propose that distributions of these different forms of carbon within the starting organic matter actually control the amount of organic pore formation through the following mechanism. With increasing thermal maturity hydrocarbon is generated from EOM while some convertible carbon becomes EOM and fill up the void space created by the expulsion of hydrocarbon (Figure 1.7-3). This process continues until the convertible organic carbon concentration drops so much that it cannot fill all the void spaces created by the expulsion of hydrocarbon from EOM; organic pores are developed at this stage. Zargari et al. (2011) noticed softening of organic matter at the initial stage of thermal maturity and progressive drop in elastic modulus and hardening of organic matter leading to increase in elastic modulus with progressive increase in thermal maturity at later stage of thermal maturity.

Detailed core description reveals that porous organic matter with larger pores at low thermal maturity occurs in samples from the cherty mudstone facies. Geologic history indicates that deposition of such facies were associated with high energy flow; hence, different types of organic matter representing a mixture of both insitu as well as transported organic matter are expected within this lithofacies. This also implies differential distribution of different forms of organic carbon and hence, heterogeneous distribution of pores within this lithofacies.

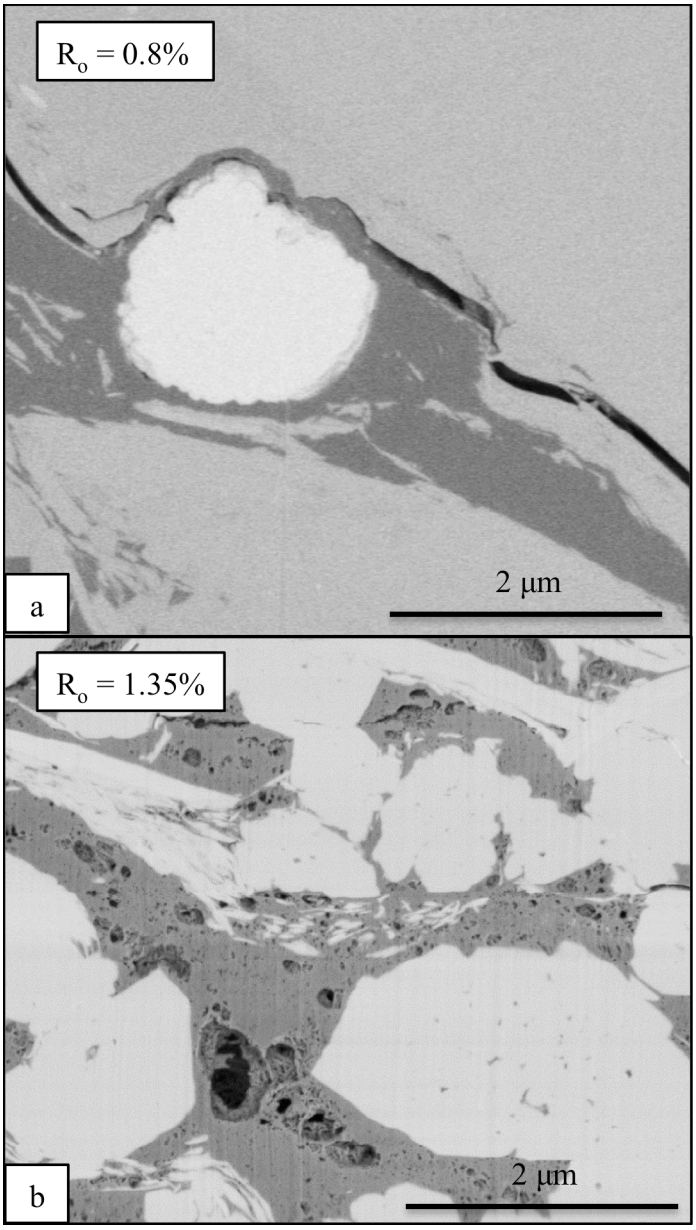

Figure 1.7-1: Backscatter SEM images of focused ion beam milled samples. Grey areas are indicating organic matter; dark areas within the organic matter indicate organic pores. (a) No organic pore in sample with estimated R_o = 0.8%. (b) Lots of organic pores can be observed in sample with estimated R_o = 1.35%.

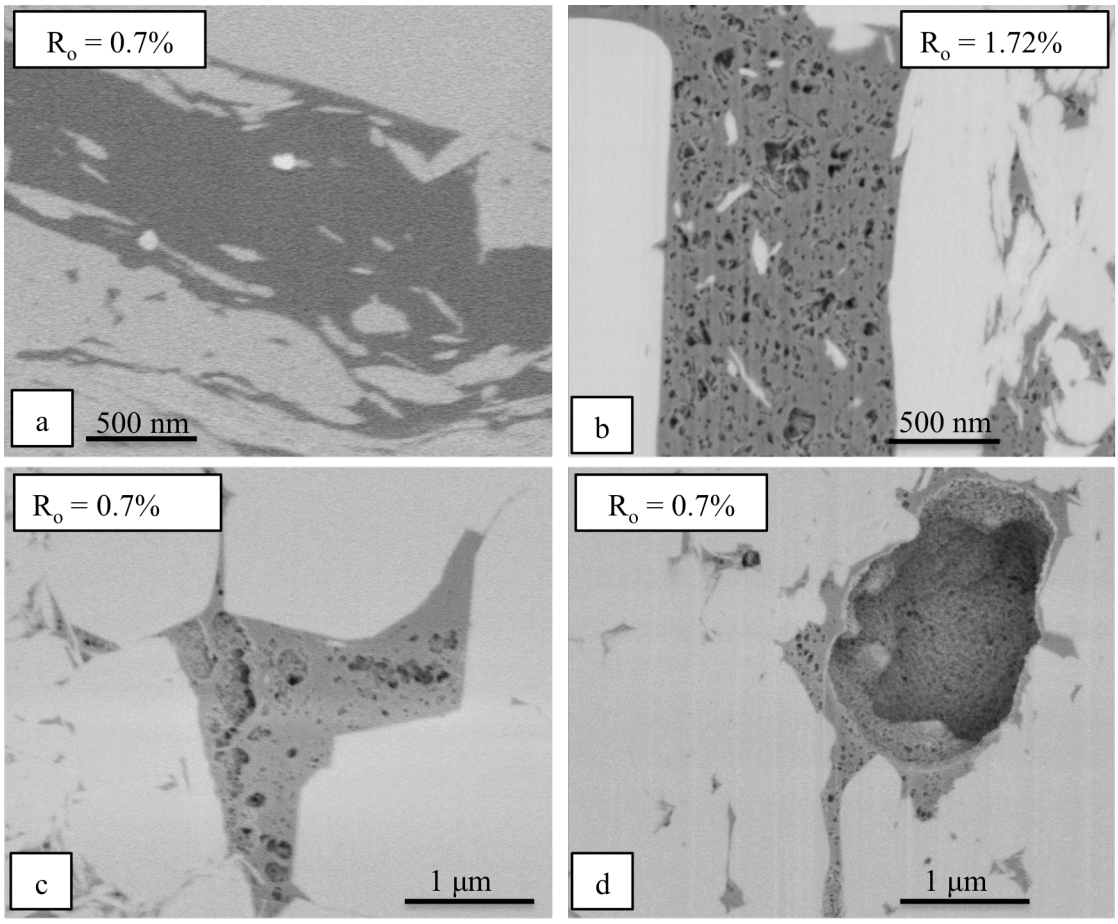

Figure 1.7-2: Backscatter SEM images of samples showing distribution of organic pores at different thermal maturity. Grey areas are indicating organic matter, dark areas within the organic matter indicate organic pores. (a) and (b) Samples with estimated R_o = 0.7% and 1.72% showing samples without any organic pores and sample with lots of organic pores. (c) and (d) Backscatter electron image of a sample with thermal maturity in the oil window (estimated R_o =0.7%) showing lots of pores. Figure d shows large micrometer-size pore present at low thermal maturity (estimated R_o = 0.7%).

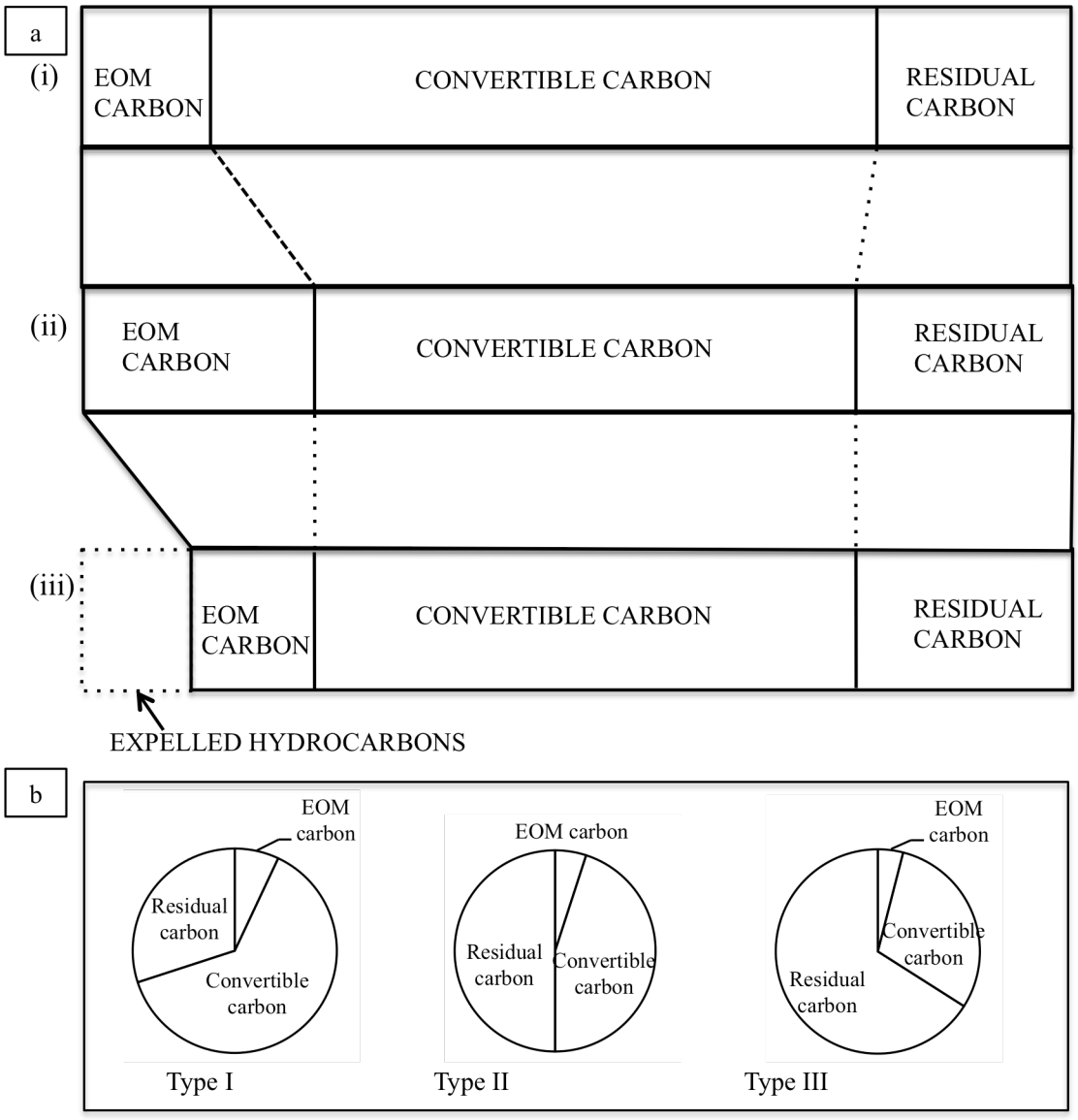

Figure 1.7-3: (a) Effect of thermal maturation on a given volume of organic carbon: (i) with increasing thermal maturity, the initial EOM and convertible carbon amounts are changed as a result of generation, (ii) EOM carbon increases at the expense of the convertible carbon, (c) with expulsion, the original TOC value is decreased by the amount of carbon contained in the expelled EOM carbon fraction. The residual carbon increases slightly with maturation. (b) Typical distributions of different forms of carbon in different kerogen types (Modified from Jarvie, 1991).

Heterogeneity of the starting organic material also causes heterogeneous distribution of porosity within samples from same depth. Backscattered SEM image from well 1 emphasizes different amount of pores within the same piece of organic matter (Figure 1.7-4). While the heterogeneity in organic matter may result from different types of organic matter present in the host rock, heterogeneity can also be observed in different body parts of multicellular organisms. Totten (2011) has imaged different types of organic material forming the outer rim of a spore compared to the material inside it.

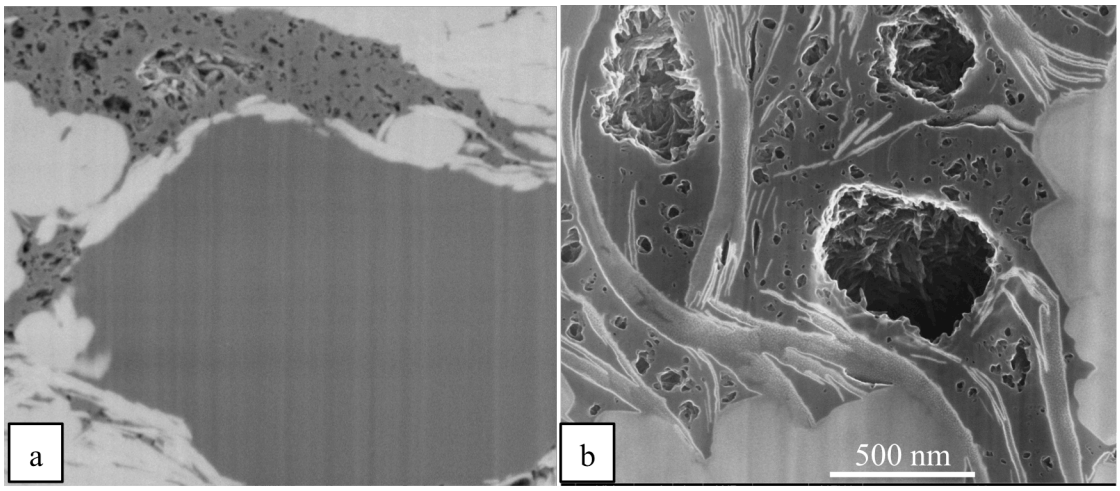

Figure 1.7-4: Backscattered images of samples from studied wells with T_{max} = 443°C and 549°C, respectively in figure a, and b. Note organic matter (dark grey) with lots of pores (black) and without any pore space located few nanometer apart, displayed in figure a. Figure b shows heterogeneous distribution of pore spaces within the same piece of organic matter. Horizontal axis is same for both the images.

1.8 Mercury injection capillary pressure (MICP)

Complex nature of the resource-shales limits the quantitative use of the capillary pressure data. However, different shapes of the capillary pressure curves

indicate different types of rocks. Four groups of rocks have been identified based on the different shapes of the capillary pressure curves. Typical characteristics of these curves are described below (Figure 1.8-1):

Type ‘A’: Incremental Hg intrusion plot increases monotonicaly and does not reach plateau even at 60,000-psi pressure (Figure 1.8-1a). This indicates that the largest pore throats are either smaller than 3 nm diameter or pores were initially larger than 3 nm and got compressed in response to increasing confining pressure during the experiment.

Type ‘B’: In this type incremental Hg intrusion plot reaches a plateau (Figure 1.8-1b) indicating that largest pore throat in this rock-type is larger than 3 nm. This also implies that this rock type has the highest permeability. This rock type is also associated with highest range of Φ. Φ. = 9.3% for the example shown in Figure 1.8-1b.

Type ‘C’: Incremental Hg intrusion has similar shape as type ‘A’ (Figure 1.8-1a, and c). The saturating and desaturation cumulative intrusion curves almost follow each other without much separation between them (lack of hysteresis) which indicate false intrusion (right figure of Figure 1.8-1c). Significant hysteresis hysteresis is observed in cumulative Hg intrusion curve type ‘A’. This rock type also shows very little Hg intrusion (<0.0005 ml/g of sample); such small volume also indicates that Hg did not actually intrude the sample and the Hg-intrusion is not real.

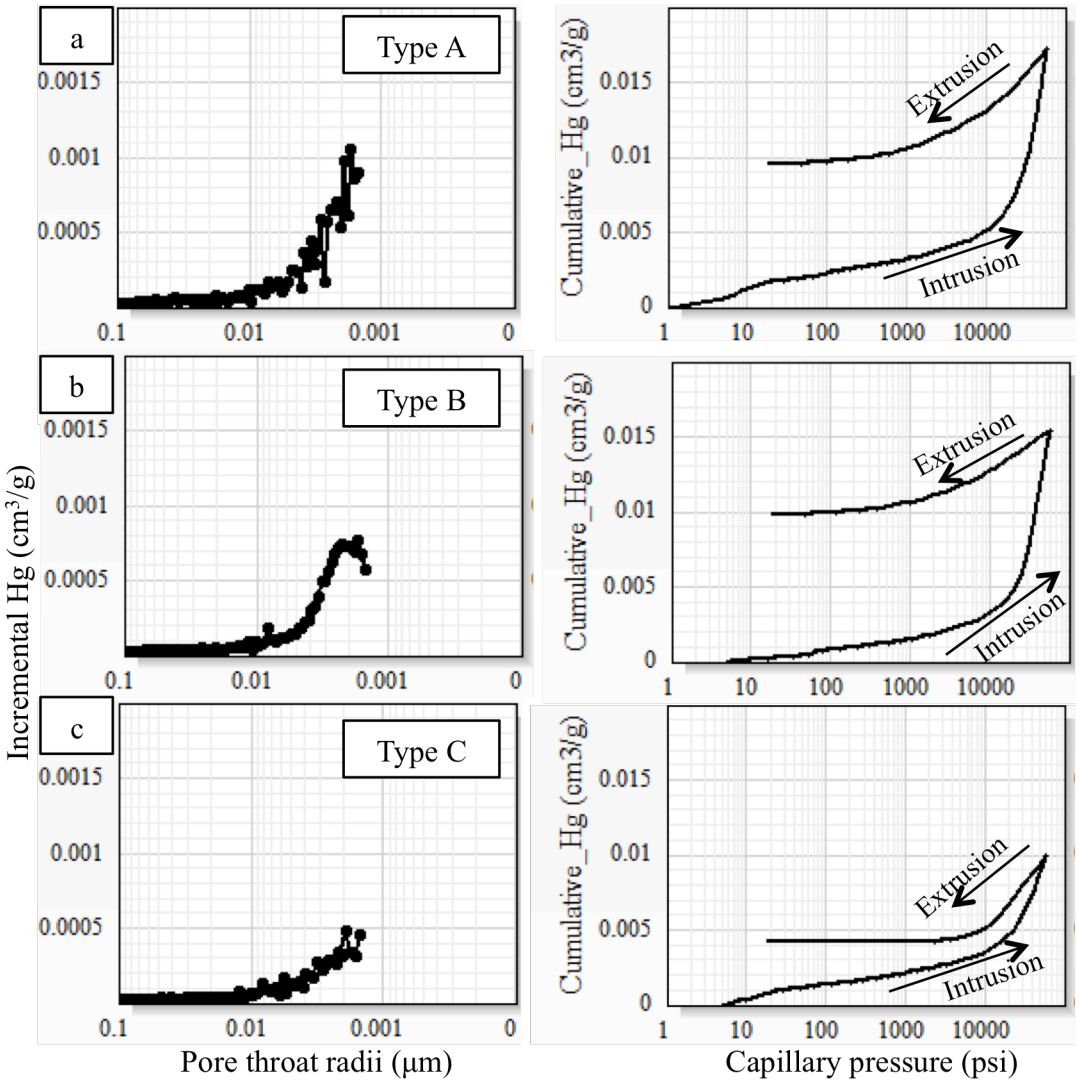

Figure 1.8-1: Examples of MICP curve type A through C in figures 'a' through 'c' respectively.

Type ‘A’, ‘B’ and ‘C’ have also been observed in the Barnett Shale from the Fort Worth Basin (Kale et al., 2010). For all the samples, it has been observed that intruded Hg volume is smaller compared to volume of Φ. This implies that either pores are not connected (mercury can intrude only into the connected pore spaces) or pore throats are smaller than 3 nm.

1.9 Petro typing

It is obvious from the previous discussion that there are at least two clusters of rocks possibly indicating different petro-types. We have used clustering analyses of principal petrophysical properties to quantitatively recognize different petro-types within the Woodford Shale in the Study area. Kale (2009) applied a similar clustering analysis technique to identify different petro-types within the Barnett Shale.

Petrophysical analysis discussed in the previous sections show that only few petrophysical parameters show sufficient dynamic range to be useful for identifying different group of rocks, such as: Φ, TOC, quartz, illite, smectite-mixed clays, total clays (Figure 1.5-1a, and b). Mineralogy data from wells 1 through 6, located in different parts of the basin, show that illite is the most dominant clay mineral and hence, total clay instead of illite have been used for clustering analyses. Previous studies (Kale, 2009; Raina, 2010; Sondhi, 2011) on other resource-shales also indicate that wide range of porosity, total organic carbon content, and mineralogy are useful in defining different rock types within the resource-shales.

Clustering analysis of different parameters using Gaussian K-means classification method (Bardley and Mangasarian, 2000) ultimately helped to quantitatively define these rock types. The Gaussian K-means classification method analyzes “N” data points

located in “I” dimensional space and then classifies them into “K” clusters, so that the variance between any two members from two different groups are more than the variance between any two members of the same group (N, I and K are any integers). Three groups of rocks (K=3) have been identified through this technique using four petrophysical parameters (I=4): Φ, TOC, quartz, and clays.

Ultrasonic velocities as well as dynamic elastic moduli also indicate different clusters as shown in Figure 1.6-5. However, ultrasonic data could not be included into the clustering analyses as only few ultrasonic measurements could be performed and also sampling of core plugs required for these measurements are biased towards more competent rocks.

Table 1.9-1 summarizes petrophysical properties of different petro-types identified through clustering analysis. Figure 1.9-1 shows petrophysical characteristics of different petro-types identified through clustering analysis. Petro-type 1 shows intermediate clay (20%<clay<53%) and quartz content (26%<quartz<55%) with high porosity and high TOC values (average TOC 7.5%). In this petro-type TOC increases proportionally with quartz content (Figure 1.9-1d), which enhances the brittleness of the host rock. Such petrophysical properties indicate that this petro-type forms good reservoir rock. Petro-type 2 has a wider range of porosity (2.4%-9%) and TOC (0%-13%). However, this petro-type is characterized by high clay concentration (>42%; 90% confidence interval) (Figure 1.9-1c). Measured petrophysical properties indicate that Petrotype 3 is characterized by both low porosity and TOC values. The organic matter in this petrotype contains large micrometer size pores identified through SEM imaging. The low porosity values are due to overall low TOC content of this facies. High quartz

content (Figure 1.9-1a) of this lithofacies makes it the most brittle (high Young's modulus-low Poisson's ratio) petro-type.

Petro-type	TOC (%)		Φ (%)		Quartz (%)		Clays (%)	
	Range	Average	Range	Average	Range	Average	Range	Average
1	1-4	2.5	2-5.5	3.9	59-73	66.5	7-20	13
2	0-13	6.5	2.4-9	6.0	13-56	37	27-71	55
3	3-12	7.5	4-9	6.5	26-55	40.5	20-53	36

Table 1.9-1: Petrophysical properties of different petro-types. Petro-type 1 with high TOC, high porosity and intermediate quartz and clay content is considered as the best petro-type followed by petro-type 2 and 3 respectively.

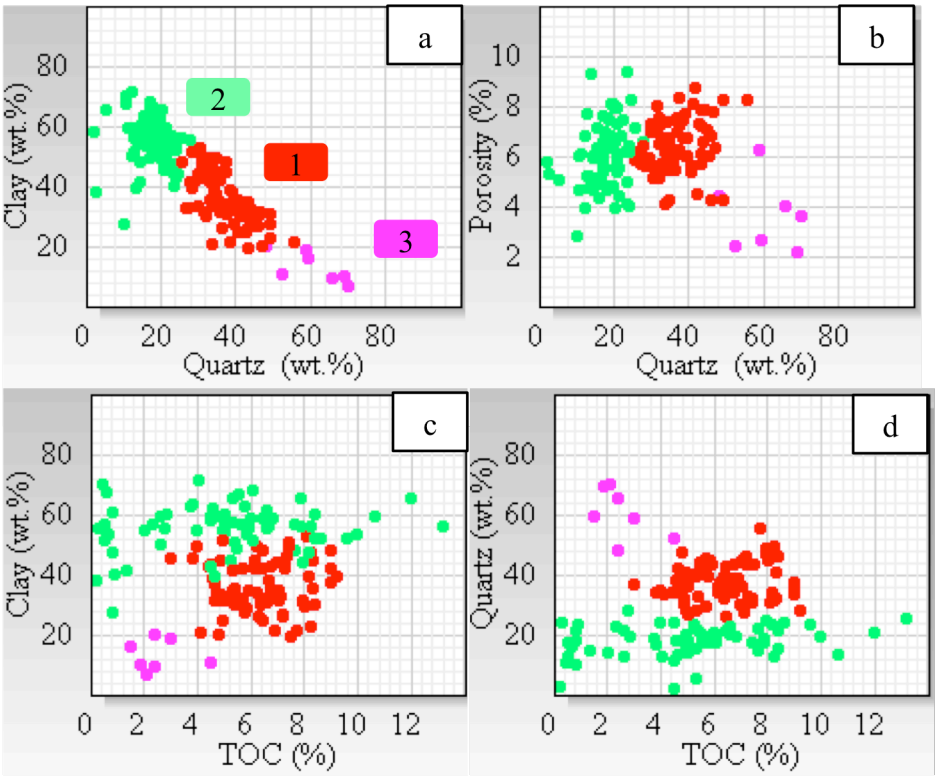

Figure 1.9-1: Crossplots of porosity, TOC, quartz and clays showing 3 petro-types identified through clustering analyses. Petrotype 1 through 3 are colored with red, green and pink as marked on figure 'a'. Figure 'a' indicates that each petro-type is characterized by unique range of clay and quartz concentrations.

Reservoir qualities indicated by petrophysical properties also correspond to the production data. For example, well 1 is a hydrocarbon producing and is characterized by the highest thickness of petro-type 1. Thicknesses of different petro-types within the Woodford interval in this well are as follows: 66%, 16% and 18% respectively for petro-type 1 through 3. While well 3 is reported as dry well, which contains the highest thickness of the clay rich petro-type 2 and the thicknesses of different petro-types within the Woodford interval in this well are as follows: 18%, 78% and 4% respectively for petro-type 1 through 3.

For example, petro-type 3 represents the cherty mudstone lithofacies, characterized by high quartz content and low TOC while petro-type 1 and 2 represent the black mudstone facies. Visual inspections of cores reveal that the cherty mudstone facies are typically centimeter thick; the thin nature of this lithofacies makes it difficult to measure petrophysical properties of this petro-type even at the laboratory-scale.

Although petrophysically petro-type 1 is the best reservoir followed by petro-type 2, TOC-rich intervals from either petro-type are characterized by low Young's modulus, high Poisson's ratio as well as high V_p-V_s ratio and hence, are considered as ductile in nature (Figure 1.9-2). Such ductile nature of the hydrocarbon/TOC enriched intervals demand intervening brittle intervals in order to initiate hydraulic fracturing. Hence, vertical juxtaposition of petro-types with contrasting mechanical properties (brittle versus ductile) will improve reservoir quality of the resource shales. Among the studied wells, the best producing well 2 is characterized by the widest distributions of petrophysical parameters indicating presence of different petro-types in the stratigraphic column. On the other hand, despite of good reservoir storage capacity (high TOC and Φ,) well 3 is a dry well. Lack of contrasting petro-types in the vertical section and high clay content limited the hydraulic fracturing in this well. This is an ideal example of a well with good storage capacity and zero hydrocarbon production due to inability to initiate hydraulic fracturing. Petro-typing is not performed on well 6 (located in between well 2 and 3) due to limited sample availability.

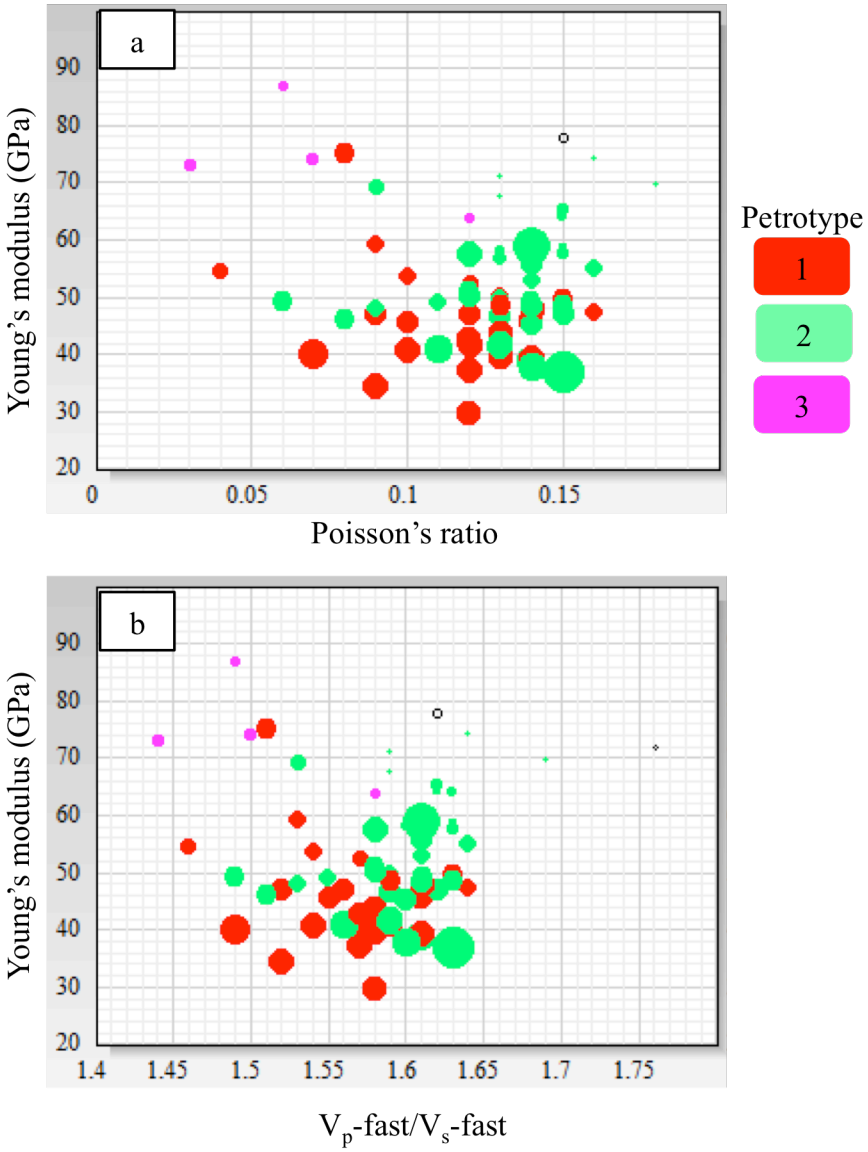

Figure 1.9-2: Crossplots of (a) Young's modulus versus Poisson's ratio (v), (b) Young's modulus versus ratio of V_p-fast/V_s-fast. Point size depicts TOC content.

Calibration of petro-types with MICP data

MICP characteristics of each petrotype is summarized in Table 1.9-2 indicating that petrotype 3 is represented by MICP type C, petro-type 2 is represented by MICP type A while petrotype 1 contains almost equal quantity of MICP type A and MICP type B.

MICP type C indicates the poorest connectivity between pores. Although SEM imaging has revealed micrometer size pores within petrotype 3, poor connectivity between those pores (as indicated by MICP type C) reduces the reservoir quality of this petrotype. MICP type A (Figure 1.8-1a) indicates pore throats smaller than 3 nanometer which resulted from nanometer-size pores present in the studied rocks and as observed through SEM-imaging. MICP type B (Figure 1.8-1b) is indicative of little larger pore throat diameter and is most commonly present within petrotype 1 compared to petro-type 2 and petrotype 3. Hence, presence of rocks with MICP type B improves the reservoir quality. Such integration of petro-types with the MICP curve types improves our understanding about individual petro-types.

Petro-type	MICP 'A'	MICP 'B'	MICP 'C'
1	41%	51%	8%
2	72.5%	17.5%	10%
3	0%	0%	100%

Table 1.9-2: Distributions of different types of MICP curve within each petro-type. MICP measurements were performed on 110 samples.

1.10 Welllog Analyses

Our objective is to find welllog proxies for these petrotypes. However, limited welllogs from only one well (well 1) were available for this study and petrotyping from well logs could not be performed. Welllogs were used in combination with core data for calculating fluid density and TOC and to identify well-log signatures of the petrotypes identified from core data.

Welllog data was first shifted to core depth prior to integrating well logs with core data. Depth-shifting is critical for this highly heterogeneous rocks and it is obvious that

correlation between core and well-log as well as any analyses involving both core and welllog data will improve with high precision depth shifting. In this study, depth shifting was performed through high-resolution gamma-ray correlation.

Total organic carbon (TOC)

Good correlations between TOC and ρ_b and V_p (Figure 1.6-5a) indicate that these two parameters can be used to estimate TOC from well logs. TOC is calculated from both compressional velocity-deep resistivity and bulk density-deep resistivity pairs using Passey method (Passey et al., 1990). Ultimately TOC is estimated at welllog scale by taking arithmetic average from these two sources and calibrating it with the core measured TOC. This welllog derived TOC can be used in combination with Welllog measured quartz and clay content in order to identify similar rock types at welllog scale as identified based on core data.

Well-log signatures of petro-types

Petrotype 1 when plotted against deep resistivity (AT90) shows the highest resistivity values compared to petrotype 2 and type 3 (Figure 1.10-1). Intervals of petrotype 1 with high resistivity, low clay concentration, and high porosity (>6.5%) further define the reservoir intervals. High resistivity values coupled with low clay concentration, high porosity, and high TOC in these intervals indicate that the high resistivities result from the hydrocarbon enrichment. Most of these intervals are located within the Middle Woodford interval, indicating that this is the most productive interval at least in this well (Figure 1.10-2). Good reservoir interval alternating with intervals of high Young's modulus and low Poisson's ratio fine tune a particular interval within the Middle Woodford as the most prolific interval for placing the horizontal well (Figure

1.10-2). This analysis indicates that it is possible to detect reservoir intervals within the Woodford Shale when well logs are used in combination with laboratory measured core data.

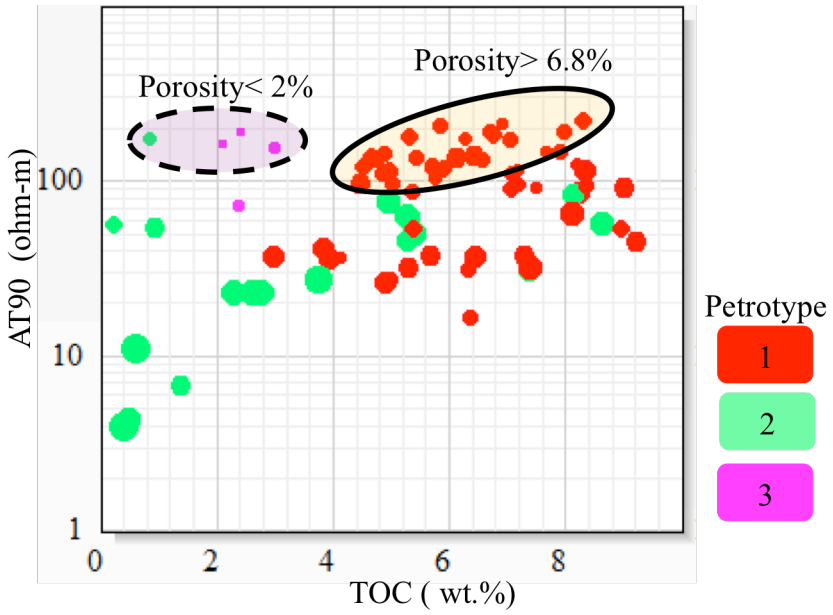

Figure 1.10-1: Crossplot of laboratory measured organic carbon (TOC) with deep resistivity from well-log (AT90). Size of the data points is proportional to clay concentration. Data points marked by solid black ellipse indicate good reservoir rocks characterized by high porosity (>6.5%), data with dashed ellipse is characterized by very low porosity (~2%).

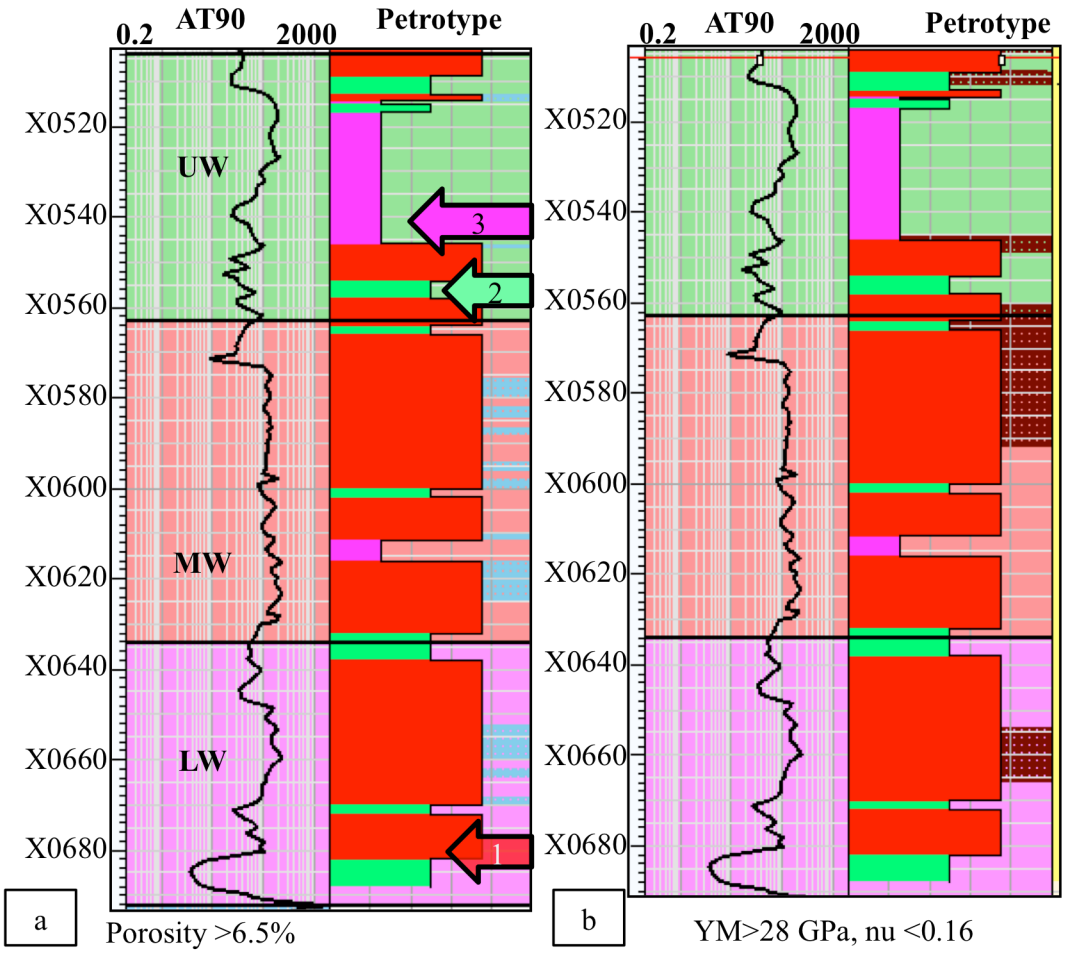

Figure 1.10-2: Distribution of the petro type 3 in well 1. Deep resistivity is plotted in track 1, petro-type is plotted in track 2. LW, MW, and UW refer to lower, middle and upper member of the Woodford Shale respectively. (a) Petro-type 3 with Φ>6.5% are highlighted with cyan in track 2. (b) Petro-type 3 with dynamic Young's modulus >28 GPa and v<0.16 are highlighted with maroon in track 2. Note, the alternating cyan and maroon intervals located within the middle Woodford member.

1.11 Conclusions

Analyses of petrophysical properties measured on samples from different part of the basin showed that four petrophysical parameters such as porosity, TOC, quartz and clay concentrations have significant dynamic range which can be used to identify different petro-types within the Woodford Shale play.

Clustering analyses using these four parameters indicated that the Woodford Shale in the study area is characterized by three petro-types. The petro-type with intermediate clay (20 wt. %- 53 wt. %) and quartz (26 wt. %- 55 wt. %) concentrations is the best reservoir rocks as those rocks also contain high TOC content (7.5 wt. %) and high porosity (6.5%). Moreover, TOC shows an increasing trend with quartz concentration within this petro-type.

Like many other resource shale the TOC-rich rocks within the Woodford Shale is ductile in nature as indicated by the dynamic elastic moduli calculated from ultrasonic measurements. Such ductile nature of the TOC-rich demand that the sweet-spots within the Woodford Shale is located at the intervals with alternating reservoir intervals (interval with good petro-type) and brittle layers (cherty mudstone facies) unlike the conventional reservoirs where the target is to place wells near the highest net to gross,.

Geologic analysis indicates that the cherty mudstone facies is resulted from storm-related deposits which typically follow the depressions on the basin floor making these areas good target for placing wells compared to basin floor highs which are characterized by high clay content deposited with the sediments from suspension fall out and least affected by detrital sediments from any storm/current flows (good source for detrital sediments).

Both thermal maturity and distributions of different forms of carbon control the formation of organic pores. More organic pores are developed with increasing thermal maturity. Heterogeneity in the organic matter causes different distributions of organic carbon, which result into heterogeneous distributions of organic pores at any stages of thermal maturity.

The integrated workflow described in this study can also be applied to identify critical petrophysical parameters followed by determination of the sweet-spots within any other resource shales.

References

Amaefule, J. O., M. Altunbay, D. Tiab, D. G. Kersey, and D. K. Keelan, 1993, Enhanced reservoir description: using core and log data to identify hydraulic (flow) units and predict permeability in uncored intervals/wells, SPE Annual Technical Conference and Exhibition, Houston, Texas, 1993 Copyright 1993, Society of Petroleum Engineers, Inc.

Ballard, B., 2007, Quantitative mineralogy of reservoir rocks using Fourier transform infrared spectroscopy: SPE Annual Technical Conference and Exhibition.

Birch, F., 1960, The velocity of compressional waves in rocks to 10 kilobars, part 1: Journal of Geophysical Research, v. 65, p. 1083-1102.

Bradley, P. S., and O. L. Mangasarian, 2000, k-plane clustering: Journal of Global Optimization, v. 16, p. 23-32.

Caldwell, C. D., 2011, Lithostratigraphy of the Woodford Shale, Anadarko Basin, West-Central Oklahoma: Mid-Continent Section meeting.

Comer, J. B., 2008, Distribution and source-rock characteristics of Woodford Shale and

age-equivalent strata: AAPG Annual Convention and Exhibition.

Curtis, M. E., R. J. Ambrose, C. H. Sondergeld, and C. S. Rai, 2011, Investigation of the relationship between organic porosity and thermal maturity in the Marcellus Shale, North American Unconventional Gas Conference and Exhibition, The Woodlands, Texas, USA, Society of Petroleum Engineers.

Energy information administration, 2011, Review of emerging resources: US shale gas and shale oil plays, ftp://ftp.eia.doe.gov/natgas/usshaleplays.pdf.

Espitalilie, J., 1986, Use of Tmax as a maturation index for different types of organic matter. Comparison with vitrinite reflectance, *in* J. Burrus, ed., Thermal modeling in sedimentary basins: Paris, Editions Technip, p. 475-496.

Gunter, G. W., J. J. Pinch, J. M. Finneran, and W. T. Bryant, 1997, Overview of an integrated process model to develop petrophysical based reservoir descriptions, SPE Annual Technical Conference and Exhibition, San Antonio, Texas, Society of Petroleum Engineers, Inc.

Hoeve, M. V., S. C. Meyer, J. Preusser, and A. Makowitz, 2011, Basin-wide delineation of gas shale sweet spots using density and neutron logs; implications for qualitative and quantitative assessment of gas shale resources: AAPG Geoscience Technology Workshop: US Shale Plays.

Jacobi, D. J., M. Gladkikh, B. LeCompte, G. Hursan, F. Mendez, J. Longo, S. Ong, M. Bratovich, G. L. Patton, and P. Shoemaker, 2008, Integrated petrophysical evaluation of shale gas reservoirs, CIPC/SPE Gas Technology Symposium 2008 Joint Conference, Calgary, Alberta, Canada, Society of Petroleum Engineers.

Jarvie, D. M., 1991, Total organic carbon (TOC) analysis, *in* R. K. Merrill, ed., Treatise

of Petroleum Geology: Handbook of Petroleum Geology, Source and Migration Processes and Evaluation Techniques, American Association of Petroleum Geologists, p. 113-118.

Jarvie, D. M., R. J. Hill, T. E. Ruble, and R. M. Pollastro, 2007, Unconventional shale-gas systems: The Mississippian Barnett Shale of north-central Texas as one model for thermogenic shale-gas assessment: AAPG bulletin, v. 91, p. 475.

Johnson, K. S., 1988, Geologic evolution of the Anadarko basin, *in* K. S. Johnson, ed., Anadarko basin symposium: Circular 90, Oklahoma Geological Survey, p. 3-12.

Kale, S., 2009, Petrophysical characterization of Barnett Shale play, MS thesis, University of Oklahoma.

Kale, S., C. S. Rai, and C. H. Sondergeld, 2010, Rock typing in gas shales, SPE Annual Technical Conference and Exhibition, Florence, Italy, Society of Petroleum Engineers.

Kamath, J., 1992, Evaluation of accuracy of estimating air permeability from mercury-injection data: SPE formation evaluation, v. 7, p. 304-310.

Karastathis, A., 2007, Petrophysical measurements on tight gas shale, MS thesis, University of Oklahoma, Norman.

Lambert, M. W., 1993, Internal stratigraphy and organic facies of the Devonian-Mississippian Chattanooga (Woodford) Shale in Oklahoma and Kansas: Source rocks in a sequence stratigraphic framework: AAPG Studies in Geology, v. 37, p. 163-176.

Loucks, R. G., R. M. Reed, S. C. Ruppel, and D. M. Jarvie, 2009, Morphology, genesis, and distribution of nanometer-scale pores in siliceous mudstones of the

Mississippian Barnett Shale: Journal of Sedimentary Research, v. 79, p. 848.

Matteson, A., and M. M. Herron, 1993, Quantitative mineral analysis by Fourier transform infrared spectroscopy, p. 1-15.

Newsham, K. E., and J. A. Rushing, 2001, An integrated work-flow model to characterize unconventional gas resources: Part I - Geological Assessment and Petrophysical Evaluation, SPE Annual Technical Conference and Exhibition, New Orleans, Louisiana, Copyright 2001, Society of Petroleum Engineers Inc.

Passey, Q., S. Creaney, J. Kulla, F. Moretti, and J. Stroud, 1990, A practical model for organic richness from porosity and resistivity logs: AAPG bulletin, v. 74, p. 1777-1794.

Passey, Q. R., K. Bohacs, W. L. Esch, R. Klimentidis, and S. Sinha, 2010, From oil-prone source rock to gas-producing shale reservoir-geologic and petrophysical characterization of unconventional shale-gas reservoirs, International Oil and Gas Conference and Exhibition in China, Beijing, China, Society of Petroleum Engineers.

Pittman, E. D., 1992, Relationship of porosity and permeability to various parameters derived from mercury injection capillary pressure curves for sandstone: AAPG bulletin, v. 76, p. 191-198.

Raina, I., 2010, Petrophysical characterization of Thirteen Finger Limestone, University of Oklahoma.

Rickman, R., M. J. Mullen, J. E. Petre, W. V. Grieser, and D. Kundert, 2008, A practical use of shale petrophysics for stimulation design optimization: all shale plays are not clones of the Barnett Shale, SPE Annual Technical Conference and

Exhibition, Denver, Colorado, USA, Society of Petroleum Engineers.

Rushing, J. A., K. E. Newsham, and T. A. Blasingame, 2008, Rock typing-keys to understanding productivity in tight gas sands, SPE Unconventional Reservoirs Conference, Keystone, Colorado, USA, Society of Petroleum Engineers.

Screiber, E., O. Anderson, and N. Soga, 1973, Elastic constants and their measurements, McGraw-Hill, New York.

Sigal, R. F., 2009, A methodology for blank and conformance corrections for high pressure mercury porosimetry: Measurement Science and Technology, v. 20, p. 045108.

Sondergeld, C., and C. Rai, 1993, A new concept in quantitative core characterization: The Leading Edge, v. 12, p. 774.

Sondergeld, C. H., K. E. Newsham, J. T. Comisky, M. C. Rice, and C. S. Rai, 2010a, Petrophysical considerations in evaluating and producing shale gas resources, SPE Unconventional Gas Conference, Pittsburgh, Pennsylvania, USA, Society of Petroleum Engineers.

Sondergeld, C. H., R. J. Ambrose, C. S. Rai, and J. Moncrieff, 2010b, Micro-structural studies of gas shales, SPE Unconventional Gas Conference, Pittsburgh, Pennsylvania, USA, Society of Petroleum Engineers.

Sondhi, N., 2011, Petrophysical characterization of Eagle Ford Shale, MS thesis, University of Oklahoma.

Sullivan, K. L., 2006, Organic facies variation of the Woodford Shale, in western Oklahoma, MS thesis, University of Oklahoma.

Swanson, B., 1981, A simple correlation between permeabilities and mercury capillary

pressures: Journal of Petroleum Technology, v. 33, p. 2498-2504.

Thomeer, J., 1983, Air permeability as a function of three pore-network parameters: Journal of Petroleum Technology, v. 35, p. 809-814.

Thomeer, J., 1960, Introduction of a pore geometrical factor defined by the capillary pressure curve: Journal of Petroleum Technology, v. 12, p. 73-77.

Totten, M. W., 2011, Electron probe micro-analysis of the Woodford Shale, south-central Oklahoma, The University of Oklahoma, Norman.

Zargari, S., M. Prasad, K. C. Mba, and E. Mattson, 2011, Organic maturity, hydrous pyrolysis, and elastic property in shales, Canadian Unconventional Resources Conference, Alberta, Canada, Society of Petroleum Engineers.

2 Chapter 2

2 Microstructural study of shales for evaluating reservoir properties at different thermal maturities

2.1 Abstract

A set of intrinsic properties including micrometer range grain size, nanometer range pore size, along with nanodarcy permeability of resource-shales demand sub-microscopic investigations in order to understand the factors controlling critical reservoir parameters like gas in place and deliverability. Scanning electron microscopic (SEM) imaging is a critical tool for this purpose. Textural arrangement, distribution of pore spaces, pore sizes, pore shapes and distribution of organic matter, as well as distributions of different minerals have been investigated on the Woodford shale samples through high magnification imaging of focused ion beam milled (FIB) samples. Samples have been chosen from different thermal maturity windows (vitrinite reflectance: 0.7% to 1.6%) in order to track any physical changes of the organic matter, and distribution of pore spaces in response to increasing thermal maturity.

SEM imaging reveals organic pores as the primary pore types within the Woodford Shale. While nanometer-size pores are common, only a few micrometer-size pores have been observed. Nanometer-size pores also estimated using a mercury injection capillary pressure injection.

Both SEM imaging and more traditional laboratory measurements indicate that porosity increases with increasing thermal maturity. However, detail SEM analyses of samples from different thermal maturities indicate that formation of organic pores is controlled by the distributions of extractable-, convertible- and residual- organic carbon at any particular place within the organic matter. At any stage of thermal maturity, heterogeneous distribution of these three forms of organic carbon originating from either the internal structure of organisms or mixing of in-situ and transported organic matter, causes a heterogeneous distribution of organic pores.

2.2 Introduction

Until the advent of shale-gas exploration, organic-rich shales have been considered to be a source rather than reservoir rock. Owing to the higher oil price compared to gas, resource-shales are being explored for liquid hydrocarbon as well. Typical characteristics of the resource-shales include fine grain size (10 nm<grain size<65 μm) (Loucks et al., 2009), and high concentration of organic matter (>2 wt.%), with thermal maturity ranging from mature to post-mature. Changes in thermal maturity affects both physical and chemical properties of the organic matter which in turn affects the overall rock properties as the low-density organic matter occupy significant rock volume. SEM imaging allows the visual inspection of fine-scale (nanometer range) constituents including organic matter. However, SEM imaging captures only an extremely small portion of the highly heterogeneous resource shales. Integrated SEM imaging and macro-scale laboratory measurements provides a means to identify microstructural effects on critical reservoir attributes.

In this paper, I performed an integrated study of the sub-microscopic features of the Woodford Shale through SEM-imaging and macroscopic laboratory measured properties. I start with textural analyses in order to document the arrangement of different rock forming elements; next, I focus on the distribution of pores spaces. In the course of this study I analyzed samples from different thermal maturities, which enabled me to document effect of thermal maturity on the host rock's physical characteristics that is discussed in the following section. Ultimately, I propose a possible mechanism for the development and distribution of major pore system within the Woodford Shale. Consistency between macroscopic measurements and SEM observations indicate that indeed the objects controlling critical reservoir attributes are small and have been captured through SEM imaging.

2.3 Sample preparation

I have examined Woodford Shale samples from five wells located within 1500 square miles in Oklahoma. Samples were examined using both a petrographic microscope and SEM imaging. Ultra-thin (30-micron thick) thin sections were prepared and impregnated with blue dye. Rock textures, along with some microcracks were identified; however, no pores were visible through the microscope.

Small pieces of samples closely resembling the rocks at the equivalent depths were collected for the SEM imaging. Special techniques need to be applied to image the nanometer-size pores present within the highly heterogeneous resource shale. First, a surface perpendicular to the bedding plane was grounded and polished, resulting in a rugose surface surface as the softer materials were selectively removed in the process.

The next step was to broad beam ion mill the surface. Unfortunately, common Ar^+ milling systems generate "curtains" or ridges on the milled surface (Curtis et al., 2010a). To address this issue a focused ion beam (FIB) integrated within the SEM machine was used to provide good surface for high-magnification images. Images of the milled surface were taken using backscattered electrons (BSE) to differentiate different constituents.

In order to correlate microstructural properties to bulk rock petrophysical properties collected from samples, I measure properties of core plugs taken from the same depth.

2.4 SEM imaging

SEM imaging is used to analyze textural arrangements between different constituents, the location of pore spaces, as well as the size and shape of pores as well as their changes with thermal maturity. Detail understanding about the location, internal structure, shape, and size of pores imaged through SEM provides the basis for an appropriate fluid flow model. I break the discussion into: (i) textural pattern, and (ii) pores.

Textural information

I break the rock forming elements into four groups useful for textural analyses: (i) organic matter, (ii) pores, (iii) clay minerals and (iv) non-clay inorganic material. Organic matter, primarily present in amorphous form, shows conformable boundaries between organic matter and inorganic particles. Such boundaries indicate that the starting organic material was soft and was squeezed into the inter-granular space with continued burial (Figure 2.4-1). In this way, organic matter occupied almost all original pore spaces at one

time in the Woodford Shale. Imbrication of the floating clay particles within organic matter further supports this hypothesis of flowing organic matter (Figure 2.4-1). Absence of hard shells at the time of deposition resulted in an amorphous organic matter from marine planktonic algae and radiolarians, those are identified as sources of organic matter in this shale (Chapter 4 of this dissertation). Most of the radiolarian tests were dissolved at the sediment-water interface owing to unstable silica (Schieber, 1996). However, some of the organic matters is still identifiable through petrographic analyses and low magnification SEM imaging, owing to the early diagenetic silicification. Both diagenetic as well as detrital minerals are observed in the SEM images.

Clays are mainly present as clay laminae, which were deformed against larger and heavier grains. Such bedding-parallel clay imbrication can be seen in Figure 2.4-2a, b, c, and e. Originally, these clay particles might have been deposited as clay floccule containing randomly orientated clay minerals (Schieber et al., 2007). The Woodford Shale lacks any bedding-parallel laminae and appears as massive mudstone for intervals with clay concentrations below a certain threshold. Clay particles are randomly oriented in intervals with lower clay concentrations as well as within intervals with diagenetic clays. Such randomly oriented clays can decrease the host shale's elastic anisotropy when present in a significant number.

The non-clayey inorganic material covers a wide range of grain size from coarse silt (>30 μm) to fine clay (<4 μm). Presence of such clay-size non-clayey minerals along with silt-sized materials provides an overall grain-supported appearance of all the rock types at low-magnification backscatter images (Figure 2.4-3).

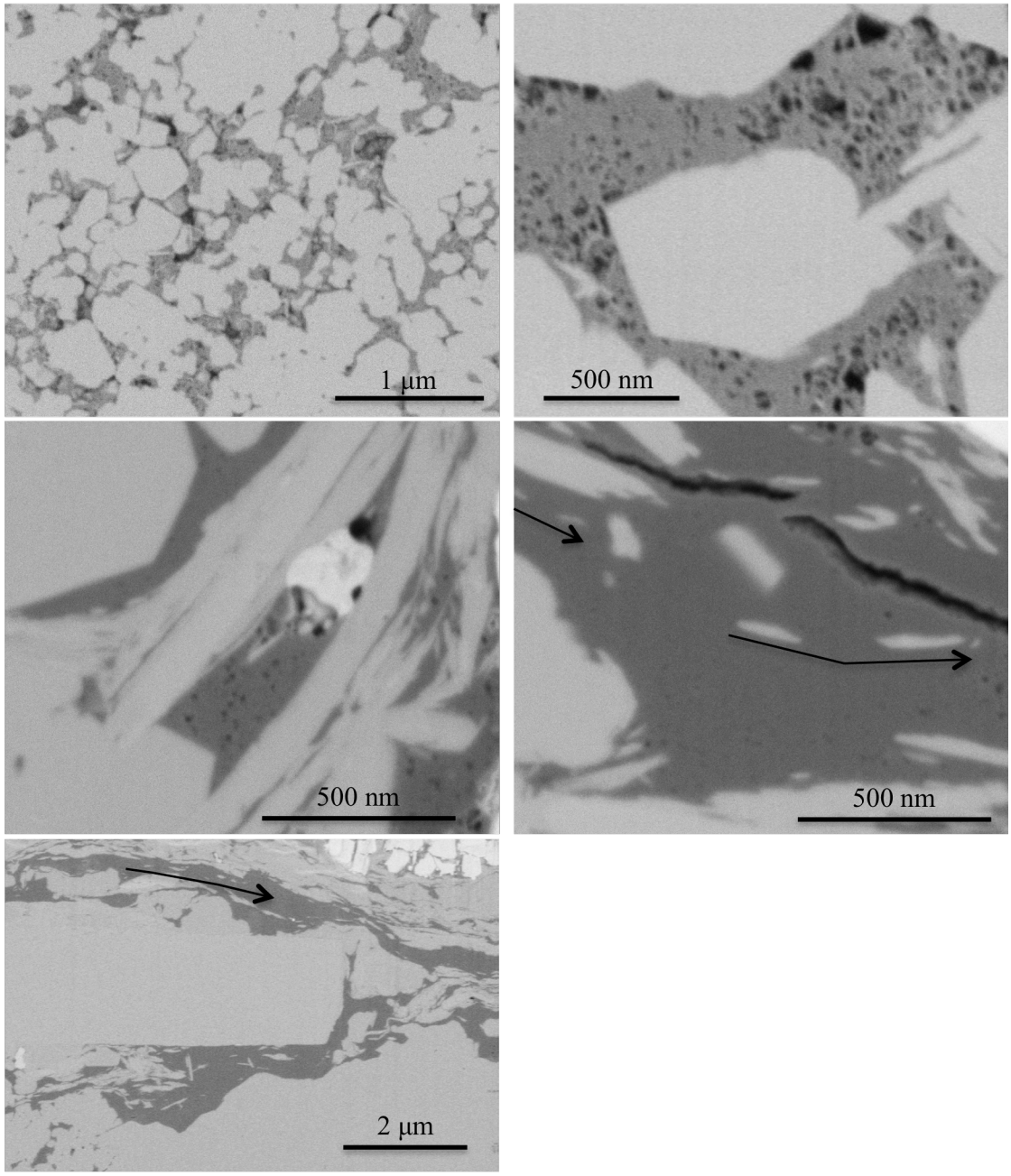

Figure 2.4-1: Backscatter SEM images of focused beam ion-milled surfaces. Dark gray materials are organic matter, black areas are pores with the light gray and white areas are other inorganic minerals. Note how the organic matter conforms to the grain boundaries of the inorganic material and occupies the intergranular spaces visible at different magnification. Black arrows indicate imbrication of floating clay particles within the organic matter indicating stream-like flow of the organic matter.

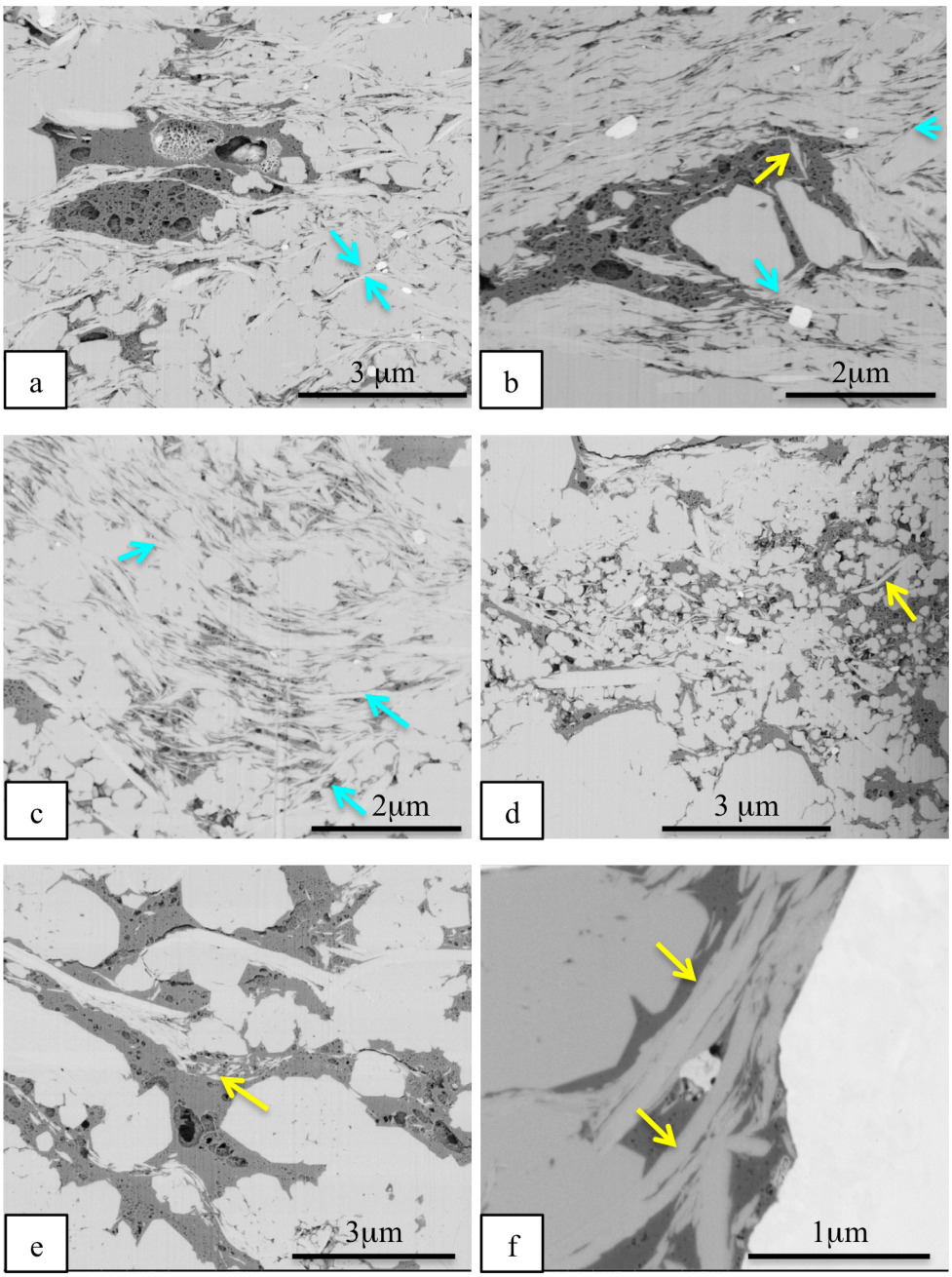

Figure 2.4-2: Backscatter SEM images showing clays with detrital (cyan arrows) and diagenetic origin (yellow arrows). Figures c and d show imbricated detrital clays and randomly oriented diagenetic clays in different areas of the same sample. Dark gray areas are organic matter.

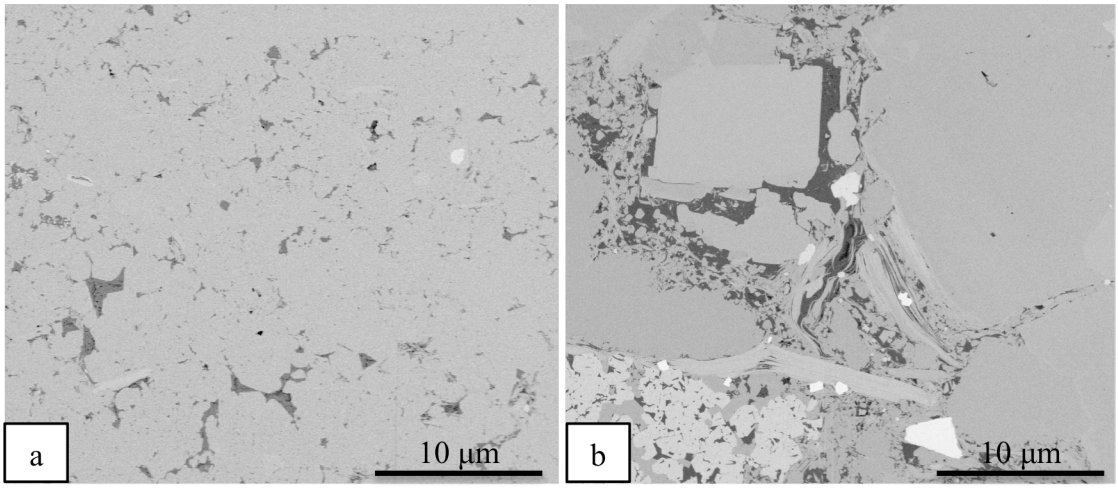

Figure 2.4-3: Backscatter SEM images of samples with low- (28%) and high-(62%) clay content respectively in Figures a and b. Note, the overall grain-supported appearance of both samples at low magnification. Sample in Figure 'a' came from X597ft, and sample in Figure 'b' came from XX250ft. Horizontal scale is same in both the images.

Pore spaces

Porosity of the Woodford Shale in the study area ranges from 0% to 10%. SEM imaging reveals that organic pores (Figure 2.4-4a-g) are the most common pore-types with very few inorganic pores (Figure 2.4-4h and i). Such observations confirm that organic matter occupied most of the intergranular spaces and thus destroyed any pre-existing intergranular porosity before significant burial. Modal analysis of organic pores visible on the SEM images reveal good correlation between the organic pores and the laboratory measured porosity (Figure 2.4-5). Curtis et al. (2010b), and Loucks et al. (2009) have observed organic pores as the most common pore types in other resource shales as well.

A few inorganic pores were observed at irregular grain boundaries (Figure 2.4-4i), spaces between individual clay particles, and in the form of microcracks. Nanometer-scale pores, observed at the SEM scale match the interpretations made from capillary pressure experiments. However, caution should be taken in attempting to generalize interpretations from SEM-scale observations since SEM imaging captures an extremely small portion of the highly heterogeneous shale.

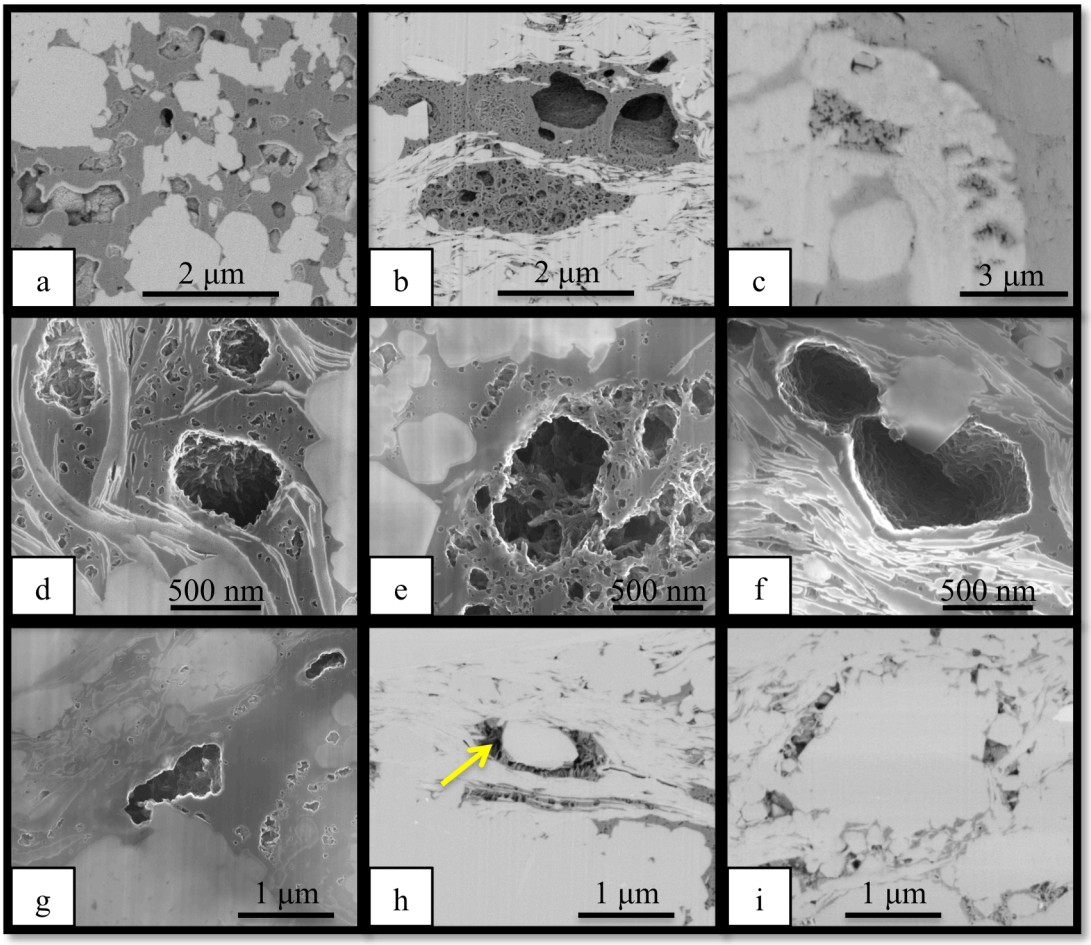

Figure 2.4-4: Backscatter SEM images showing distribution of pores in the Woodford Shale. (a) and (b) Backscatter images of organic-pores in samples from two wells. (c) Organic matter present within a fossil. Porosity developed inside that organic matter. (d), (e), and (f) High magnification SEM images showing internal structures of the organic pores. (g) Pores formed within the bitumen. (h) Pore spaces have developed at the boundary of a quartz grain and organic matter (dark grey). (i) Inorganic pore developed at the irregular grain boundary. Organic matter in the underlying layer is visible through the empty pore space.

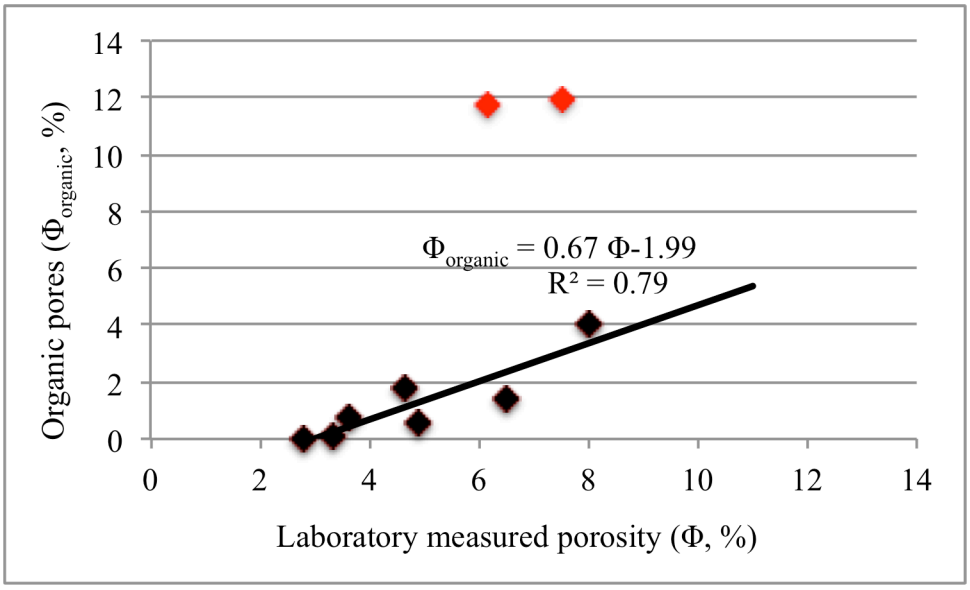

Figure 2.4-5: Crossplot of organic pores calculated from the modal analysis of the SEM images and laboratory-measured porosity. High correlation between the two indicates organic pores as the most common pore type in the studied rock. Two outlying points (shown in red) are from samples, which were highly photogenic, thus biasing our attention towards the organic pores.

Large variations of the organic pore size and shape as well as their heterogeneous distributions observed at SEM-scale further complicate the reservoir evaluation process. Most commonly, pores vary from a few nanometers to few 100s of nanometers (Figure 2.4-4b, d, and g, and Figure 2.4-6). Average, pore sizes observed through SEM imaging matched with the macroscopic averaging measures of pore bodies through nuclear magnetic resonance (NMR) relaxation and of pore throats through high-pressure mercury injection. Shape of the organic pores also varies from semi-circular (Figure 2.4-4, and Figure 2.4-6) to high aspect ratio micro-crack shape (Figure 2.4-7). High magnification images also reveal that these shales are characterized by complex internal pore structures

(bird's-nest-like structure) (Figure 2.4-4d, and e, and Figure 2.4-6) instead of tubular pores. Such complex internal pore structure is expected to improve connectivity between different sizes of pores as observed in Figure 2.4-4b, and Figure 2.4-6.

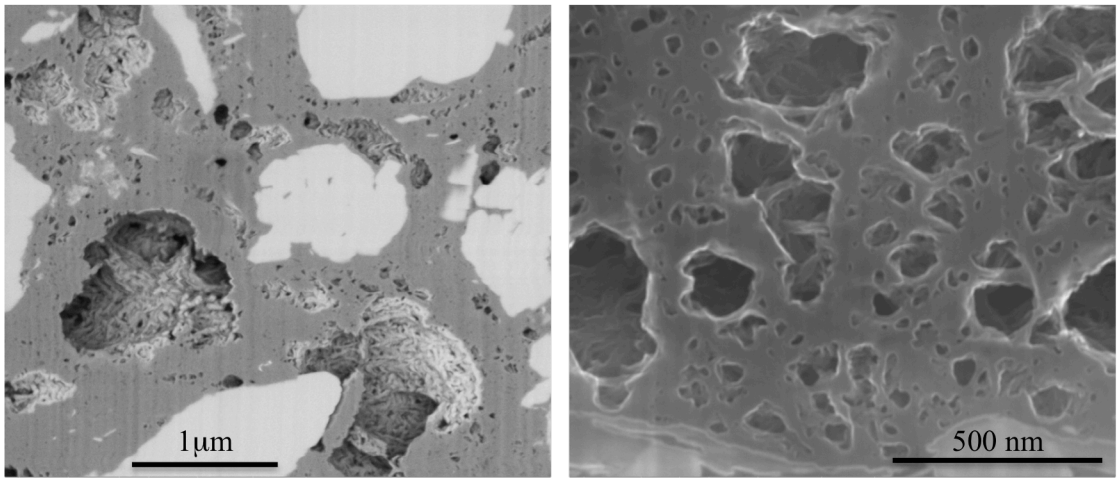

Figure 2.4-6: Backscatter SEM images showing different sizes of pores even within the same piece of organic matter.

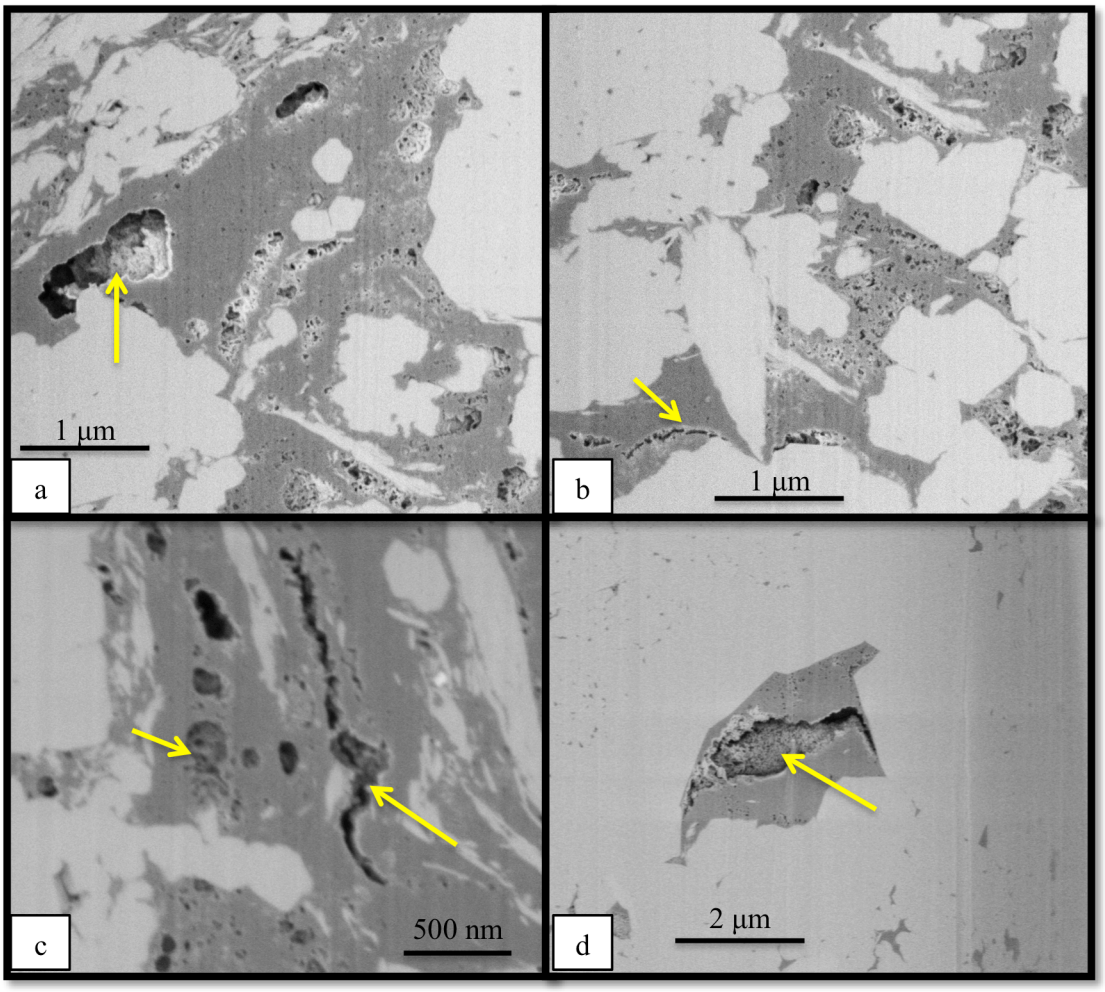

Figure 2.4-7: Backscatter SEM images showing different shapes of the organic pores. Note, the shape varies from almost circular- to crack-shape with high aspect ratio. In Figure 'c' mineral growth connecting either side of the open space ensuring the intrinsic origin of these pores.

Thermal maturity

I have studied samples from the Woodford Shale over a thermal maturity range varying from the oil window (R_o = 0.7%) to the wet gas condensate window (R_o = 1.72%). Figure 2.4-8 shows examples of organic pores at different thermal maturity.

A limited numbers of pores have been identified within organic matter @ R_o = 0.7%. Microcrack like pores (Figure 2.4-8b) at the boundary between organic matter and inorganic minerals have been observed in this low maturity sample. Microcrack like pores also have been reported at low thermal maturity during hydrous pyrolysis experiments on the Woodford Shale (O'Brien et al., 2002). On the other hand, abundant organic pores are observed in samples with higher maturity values (Figure 2.4-8c, and d). Laboratory measured porosity on 200 samples show overall higher porosity at higher thermal maturity compared to samples with lower maturity and equivalent TOC (Figure 2.4-9).

Despite an overall increase in organic pores with increasing thermal maturity, Figure 2.4-8e and f show significant numbers of organic pores in samples having low thermal maturity (R_o = 0.7%). Both figures are taken from the same sample. Figure 2.4-8f shows micrometer size organic pores within a cherty mudstone sample. Visual inspections of the core reveal that such pore spaces are characteristic of the cherty mudstone facies. This cherty mudstone facies are typically a few centimeters thick and are not easily distinguishable in rock samples, as they appear as shiny black rocks in a black mudstone facies background (Figure 2.4-8g). The non-linear boundary between the cherty mudstone facies and the background black mudstone facies indicates that deposition of the cherty facies was associated with high energy flow; hence, different types of organic matter representing a mixture of both in-situ as well as transported organic matter are expected within this lithofacies. The presence of large micrometer-size organic pores within the cherty facies at low thermal maturity indicates that the development of organic pores is not solely controlled by the thermal maturity.

SEM imaging also reveals a heterogeneous distribution of the organic pores even at a fixed thermal maturity. For example, Figure 2.4-8c shows preferential development of pore spaces in some areas of the same piece of organic matter. Such preferential porosity development most likely reflects compositional differences within the organic matter. For example, Totten (2011) has imaged different types of organic material forming the outer rim of a spore compared to the material inside it.

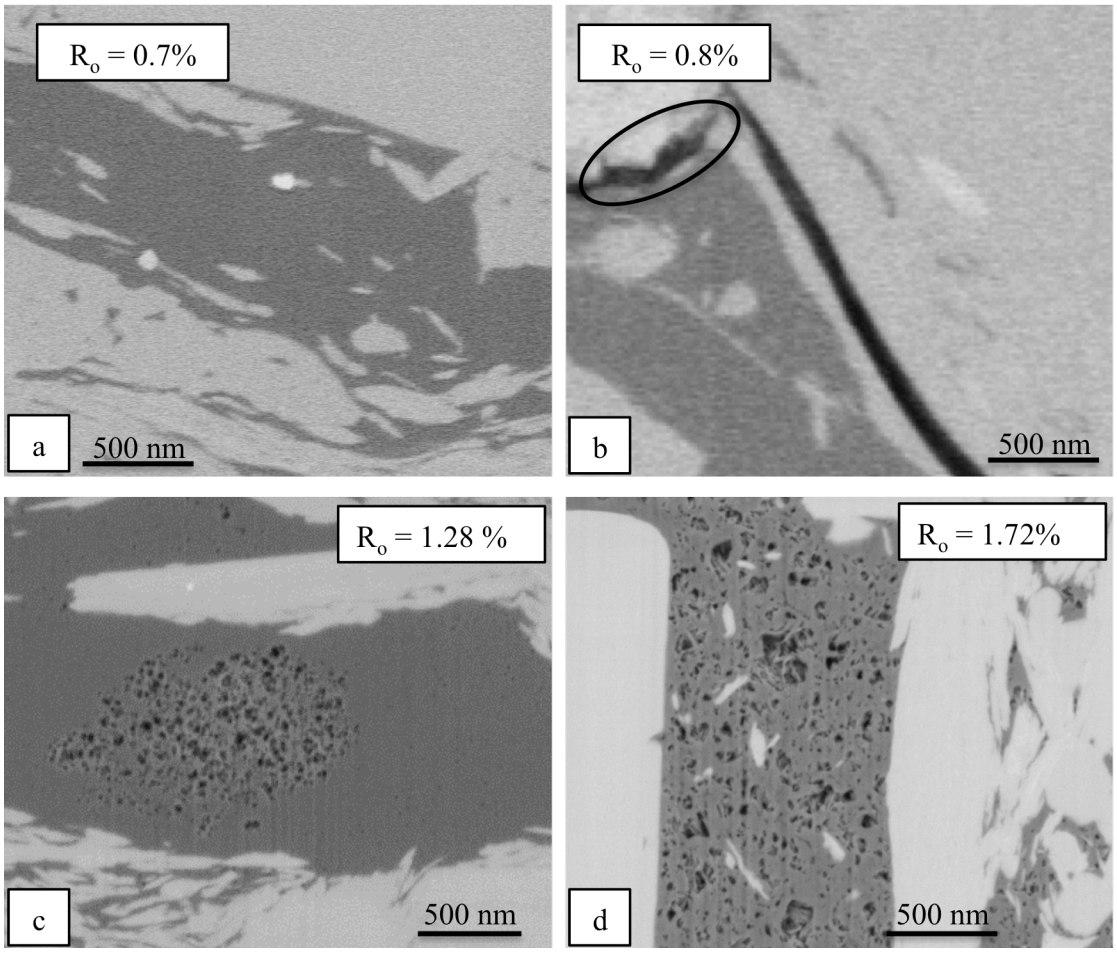

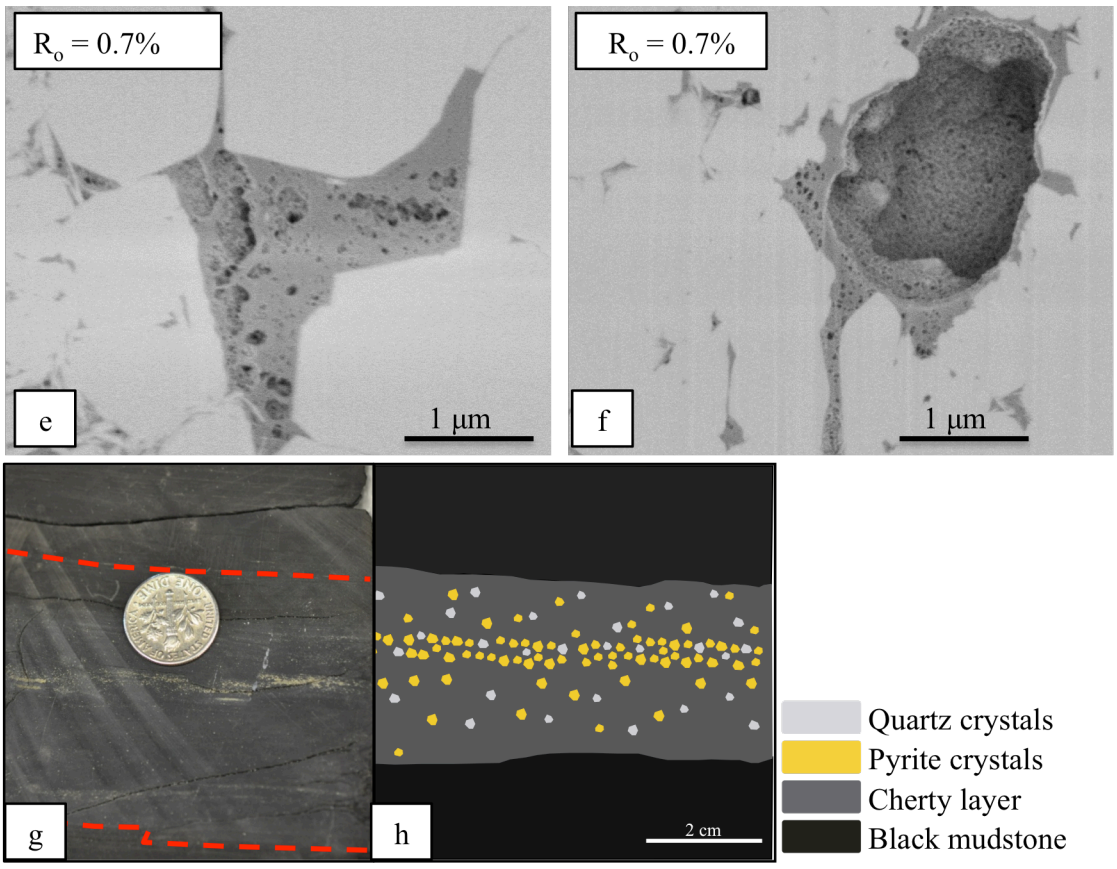

Figure 2.4-8: Backscatter SEM images of samples from different thermal maturity. (a), and (b) Samples in the oil-window, showing almost no organic pores except for a microcrack like pore marked by the black ellipse. (c), and (d) Samples having higher thermal maturity (wet gas-condensate window) containing lots of organic pores. Preferential or localized pore space development in the same piece of organic matter shown in Figure c. (e) and (f) Picture taken from the same sample with thermal maturity in the oil window. Figure f shows micron size pores. (g) Photo of a hand specimen showing the cherty layer bounded by the two red lines (dime for scale). (h) Schematic diagram of Figure g, showing the centimeter thick chert layer.

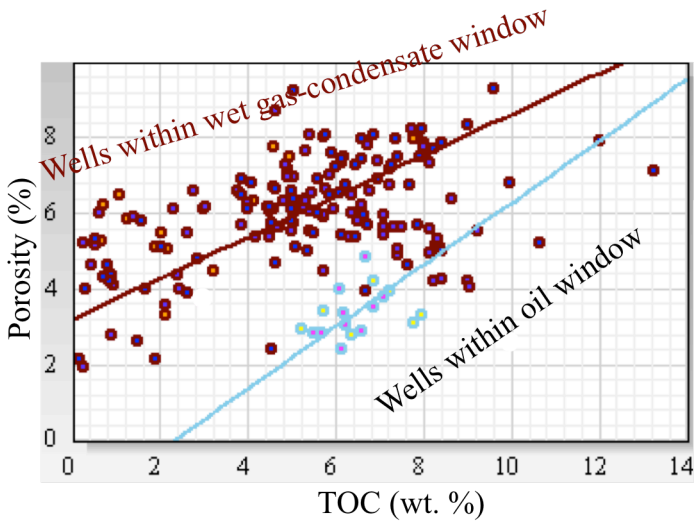

Figure 2.4-9: Crossplot of laboratory measured porosity and total organic carbon (TOC) showing overall lower porosity for less mature wells compared to highly mature wells.

Discussion

Here I propose a possible mechanism for the formation of organic pores that can explain the observed heterogeneous distribution of organic pores. Jarvie (1991) documented three forms of organic carbon such as: (i) extractable organic carbon (EOM), (ii) convertible carbon, and (iii) residual carbon. Ratios between these three forms of organic carbon control the organic pore formation within the organic matter. With increasing thermal maturity hydrocarbon is generated from EOM while some convertible carbon gets converted to EOM and fills up the void space created by the expulsion of hydrocarbons (Figure 2.4-10). Hence, organic pores are developed only when the convertible organic carbon concentration has dropped sufficiently low that it can no longer fill all the void spaces created by the expulsion of hydrocarbon from EOM. Hydrous pyrolysis experiments by Zargari et al. (2011) showed that the original solid

organic matter expands voluminously and almost covers the whole surface of the host rock at the early stage of thermal maturity (Figure 2.4-11) due to the expansion of the convertible organic carbon at the early stages of thermal maturity. At a later stage of thermal maturity, organic matter hardens, although the surface area increases through formation of organic pores (Figure 2.4-11). The proposed mechanism for organic pore development also predicts that organic pores will generate at a much earlier stage within organic matter containing high EOM and high EOM/convertible organic carbon compared to those organic matter with similar EOM but lower values of EOM/convertible organic carbon.

I interpret the different sizes of pores in Figure 2.4-4d, and e, and Figure 2.4-6 to be the result of multi-stage hydrocarbon expulsion. Hydrocarbon is first generated from the most labile part of the organic matter and hence, pores are first created in those areas of high labile carbon. With a progressive increase in thermal maturity, hydrocarbon escapes from less labile part and initiate small size pores in new areas. Pre-existing pores in the labile areas grow bigger.

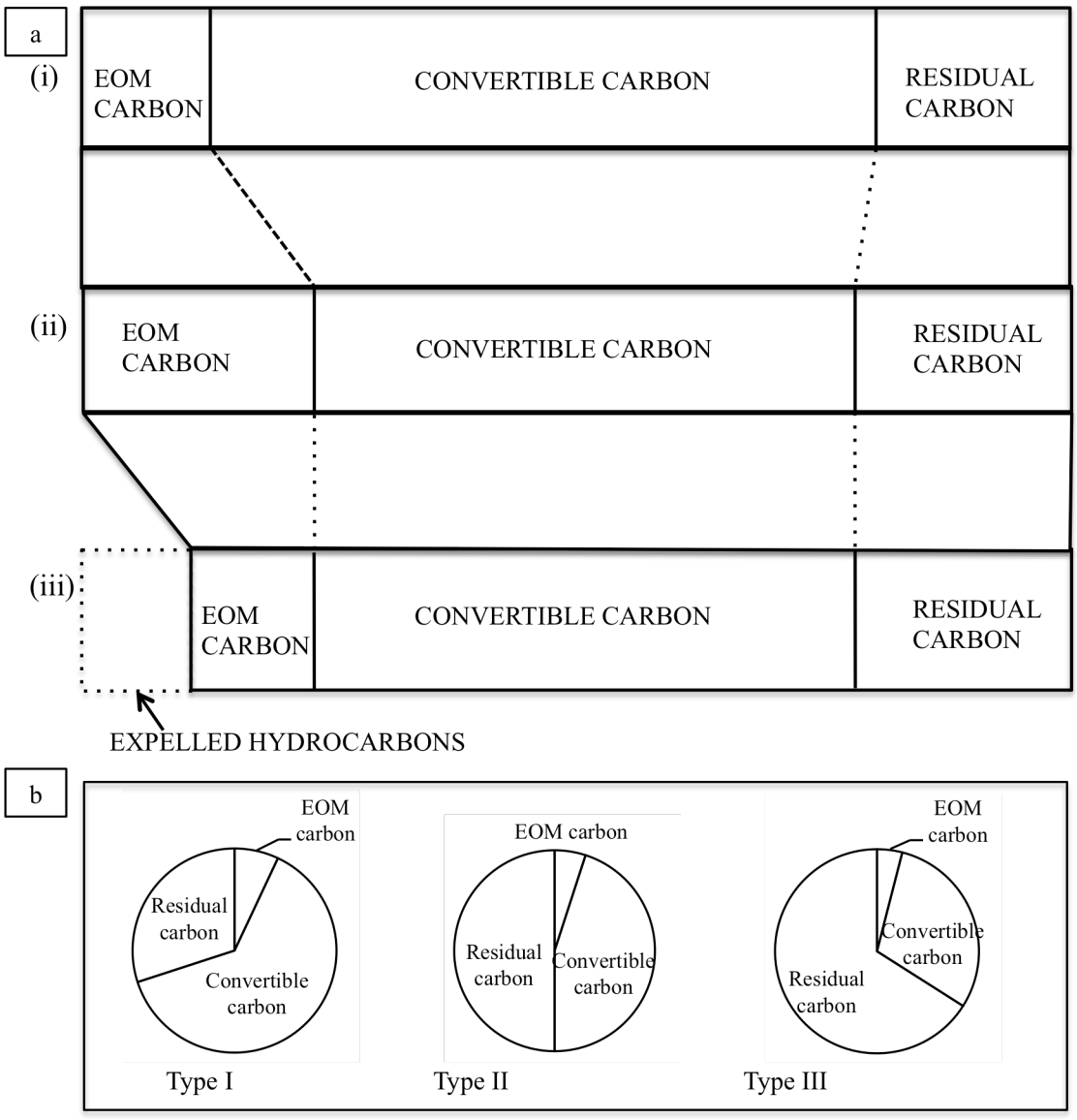

Figure 2.4-10: (a) Effect of thermal maturation on a given volume of organic carbon. (i) With increasing thermal maturity, the initial EOM and convertible carbon amounts are changed as a result of generation of hydrocarbon. (ii) EOM carbon increases at the expense of the convertible carbon. (iii) With expulsion, the original TOC value is decreased by the amount of carbon contained in the expelled EOM carbon fraction. The residual carbon increases slightly with maturation. (b) Typical distributions of different forms of carbon in different kerogen types. Modified from Jarvie, 1991.

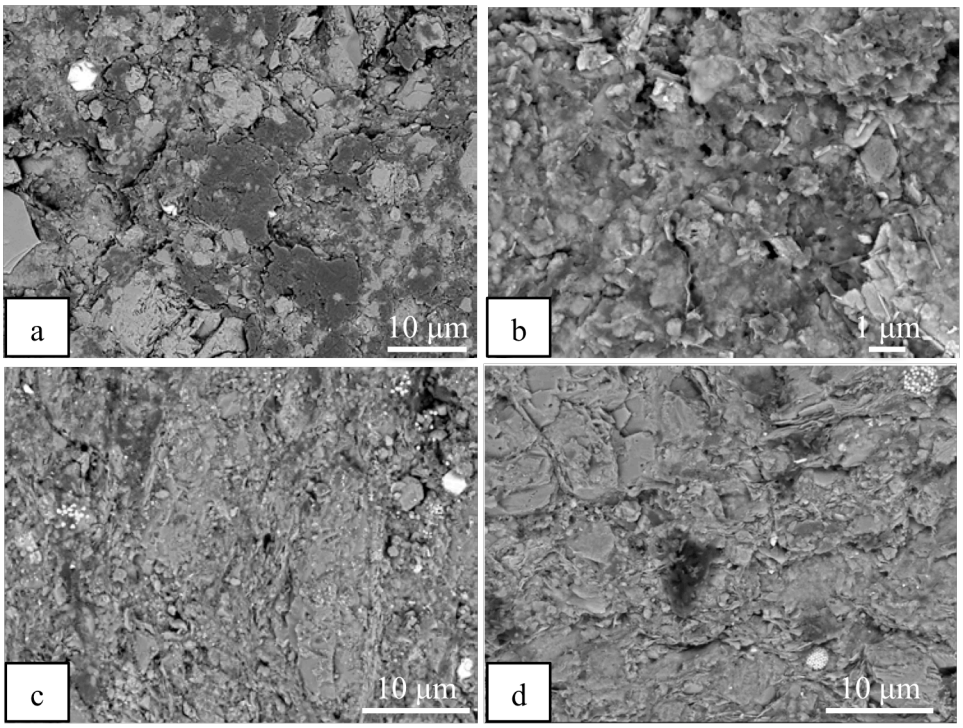

Figure 2.4-11: SEM images showing effect of hydrous pyrolysis on samples from the Bakken Shale with varying thermal maturity. (a) Before and (b) after pyrolysis of a sample with Tmax = 431.2°C, showing a dramatic change in the physical property of organic matter. Note in Figure b, that the generated hydrocarbon in the cooked sample covers most grains. In Figure a the natural state sample darker colored kerogen can be distinguished from lighter colored grains. (c) Before and (d) after pyrolysis of a sample with Tmax = 457.1°C showing minor changes after pyrolysis. Modified from Zargari et al. (2011).

2.5 Conclusions

Micro-scale inspections have revealed a set of characteristic features critical to development of the Woodford Shale. Although SEM imaging captures only an extremely small portion of the highly heterogeneous resource shales, it provides detail understanding about the internal pore structure and connectivity. These estimates correlate well to macroscopic averaging measurements of pore bodies through nuclear magnetic resonance (NMR) relaxation and of pore throats through high pressure mercury injection, indicating that indeed the objects controlling critical reservoir attributes of the Woodford Shale are small and have been captured through SEM imaging.

Organic pores are the most common pore type within the Woodford Shale. Pores of inorganic origin occur at irregular grain boundaries, interstitial spaces between individual clay platelets, as well as microcracks.

A combination of SEM imaging and petrophysical analyses indicates that the amount of organic pores increase with increasing thermal maturity. Heterogeneity in the starting organic material causes heterogeneous distribution of EOM, convertible and residual organic carbon, which in turn causes heterogeneous porosity distribution even within the same piece of organic matter.

SEM imaging revealed that the Woodford Shale is characterized by two sources of clays: detrital and diagenetic. Detrital clays are imbricated and form parallel laminae if not distorted by the surrounding larger and heavier grains. Diagenetic clays are randomly oriented and decrease the shale anisotropy.

References

Curtis, M. E., C. H. Sondergeld, R. J. Ambrose, and C. S. Rai, 2010a, Microstructural observations in gas shales: AAPG Hedberg Conference.

Curtis, M. E., R. J. Ambrose, and C. H. Sondergeld, 2010b, Structural characterization of gas shales on the micro- and nano-scales, Canadian Unconventional Resources and International Petroleum Conference, Calgary, Alberta, Canada, Society of Petroleum Engineers.

Jarvie, D. M., 1991, Total Organic Carbon (TOC) Analysis, *in* R. K. Merrill, ed., Treatise of petroleum geology: handbook of petroleum geology, source and migration processes and evaluation techniques, American Association of Petroleum Geologists, p. 113-118.

Loucks, R. G., R. M. Reed, S. C. Ruppel, and D. M. Jarvie, 2009, Morphology, genesis, and distribution of nanometer-scale pores in siliceous mudstones of the Mississippian Barnett Shale: Journal of Sedimentary Research, v. 79, p. 848.

O'Brien, N. R., M. D. Cremer, and D. G. Canales, 2002, The role of argillaceous rock fabric in primary migration of oil: Transactions-Gulf Coast Association Of Geological Societies, v. 52, p. 1103-1112.

Schieber, J., 1996, Early diagenetic silica deposition in algal cysts and spores; a source of sand in black shales: Journal of Sedimentary Research, v. 66, p. 175-183.

Schieber, J., J. Southard, and K. Thaisen, 2007, Accretion of mudstone beds from migrating floccule ripples: Science, v. 318, p. 1760-1763.

Totten, M. W., 2011, Electron probe micro-analysis of the Woodford Shale, south-central Oklahoma, The University of Oklahoma, Norman.

Zargari, S., M. Prasad, K. C. Mba, and E. Mattson, 2011, Organic maturity, hydrous pyrolysis, and elastic property in shales, Canadian Unconventional Resources Conference, Alberta, Canada, Society of Petroleum Engineers.

3 Chapter 3

3 Seismic attribute driven integrated characterization of the Woodford Shale in west-central Oklahoma

3.1 Abstract

The organic-rich, silty Woodford Shale in west-central Oklahoma is a prolific resource play producing both gas and liquid hydrocarbons. I calibrate seismic attributes and pre-stack inversion using well logs and core information within a seismic geomorphologic framework to define the overall basin architecture, major stratigraphic changes, and related changes in lithologies. Core measurements of elastic moduli and TOC indicate that the Woodford Shale can be broken into three elastic petro-types important to well completion and hydrocarbon enrichment. Upscaling these measurements facilitates regional mapping of petro-types from prestack seismic inversion of surface data.

Seismic attributes highlight rugged topography of the basin floor of the paleo Woodford Sea, which controlled the lateral and vertical distribution of different lithofacies containing variable amount of TOC, as well as quartz which controls brittleness. Depressions on the basin floor contain TOC-lean cherty lithofacies alternating with TOC-rich lithofacies, thus resulting in brittle-ductile rock couplets. In contrast, basin floor highs are characterized by overall TOC-rich ductile lithofacies.

Seismic attributes illuminate complex post-Woodford tectonic deformation. The Woodford Shale is known to be naturally fractured on outcrop. Image log analysis in

other shale plays shows a good correlation between such tectonic features and natural fractures. These features need to be correlated with well trajectories and EUR to determine which hypothesized "fracture sets", if any, to improved well performance.

3.2 Introduction

The Late Devonian Woodford Shale was deposited in an epeiric sea covering a wide area of the southern midcontinent. Regionally the Woodford Shale play is divided into three parts: the Woodford, the Cana-Woodford of the Midwest and the Barnett Woodford of the Southwest, with estimated technically recoverable resource of 22.21 TCF, 5.72 TCF and 32.15 TCF respectively (EIA, 2011). The current study focuses on the Woodford Shale of the Midwest (Figure 3.2-1) where the shale is reported to produce dry gas, condensate, and oil and has an average thickness of 200 ft. In the study area the Woodford Shale exhibits complex and heterogeneous lithological and hence geophysical characteristics. Core analyses discussed in Chapter 4 of indicate that the Woodford Shale is characterized by both lithological heterogeneity and non-uniform fracture distributions within the study area. My goal is to integrate core analysis results with the seismic data to identify areas with having high TOC, as well as more brittle lithology that favor natural fracture concentrations.

A number of authors have used seismic attributes to illuminate geomorphologic features such as collapse chimneys and fracture zones within resource shales. Sullivan et al. (2006) used a set of seismic attributes to highlight collapse chimneys associated with the collapse and karsting of the underlying Limestone. Marfurt (2010) presents a set of volumetric seismic attributes to quantitatively highlight different shapes of seismic reflector. Chopra and Marfurt (2010) discuss seismic attributes useful for highlighting

fracture zones. Guo et al. (2010) have used seismic attributes to illuminate zones of faults and fractures within the Woodford Shale in the Arkoma Basin. Arroyal (2009) presents a multi-scale study highlighting fractures within the Woodford Shale and directly correlates potential fracture zones identified from seismic attributes with the fracture zones identified on the outcrop. Schuelke (2011) used a set of attributes to map drilling hazards and showed how curvature volumes can be used to link natural fractures in shales to hydraulic fracture performance.

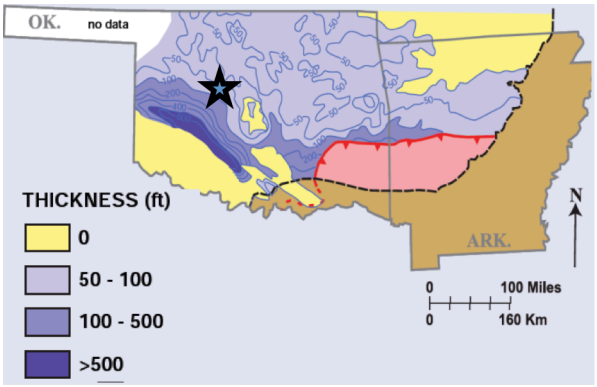

Figure 3.2-1: Thickness map showing the distribution of the Woodford Shale in Oklahoma. The star shows the study area. Map modified from Comer (2008).

In this paper, I present a workflow for the regional characterization of the Woodford Shale. I start with the mapping of regional geomorphologic features. Next, I show a comparison between petrophysical properties extracted through simultaneous prestack seismic inversion, well logs and core measurements. I will use this analysis to provide the calibration necessary to map the regional distribution of different elastic petro-types within the Woodford Shale in the study area. Finally, I use seismic attributes to map areas that have been highly deformed and are thus more likely to exhibit natural

fractures. I conclude with a summary of reservoir potential and data needed to better implement my workflow.

3.3 Depositional environment and stratigraphic framework

Pre-Woodford basin geomorphology shows irregular remnant topography that formed the basin floor of the Woodford Sea, which in turn controlled the distributions of different lithologies, key to mapping the resource potential in the study area.

Time-structure maps (Figure 3.3-2) of the Woodford Shale and the underlying Hunton Limestone show an overall flat topography with structural dips of less than 2°. Such time-structure maps reveal that the palaeo shoreline was located toward the northeast while the basin depocenter was located toward the southwest. The time-thickness map of the Woodford Shale (Figure 3.3-1) shows little correlation between the top and base time-structure maps in Figure 3.3-2. Vertical slices through the 3D seismic amplitude volumes (Figure 3.3-3) show a number of faults extending through these stratigraphic intervals indicating that major tectonic activities affected the study area. Most faults stop below the Oswego Limestone horizon indicating that tectonic activity occurred during Pennsylvanian time, consistent with Johnson's (2008) observation that the Pennsylvanian was a time of crustal unrest when both orogeny and basin subsidence affected Oklahoma.

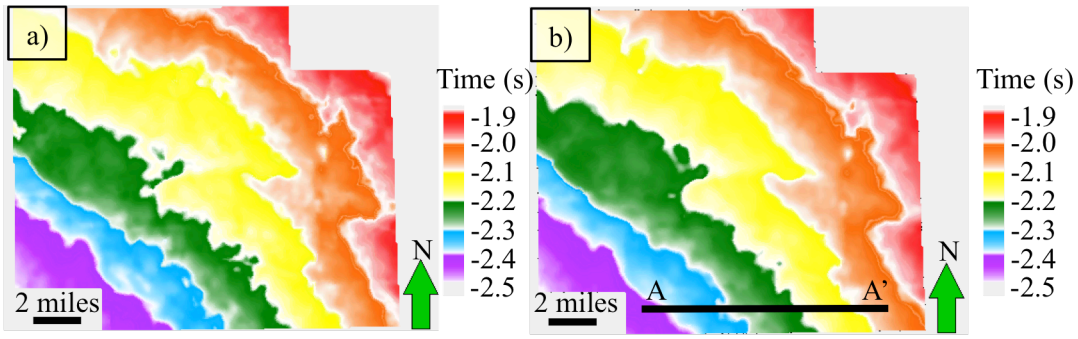

Figure 3.3-2: Time structure map of the (a) base of the Woodford Shale/top of the Hunton limestone, and (b) top of the Woodford Shale. Vertical slices along line AA' are shown in Figure 3.3-3.

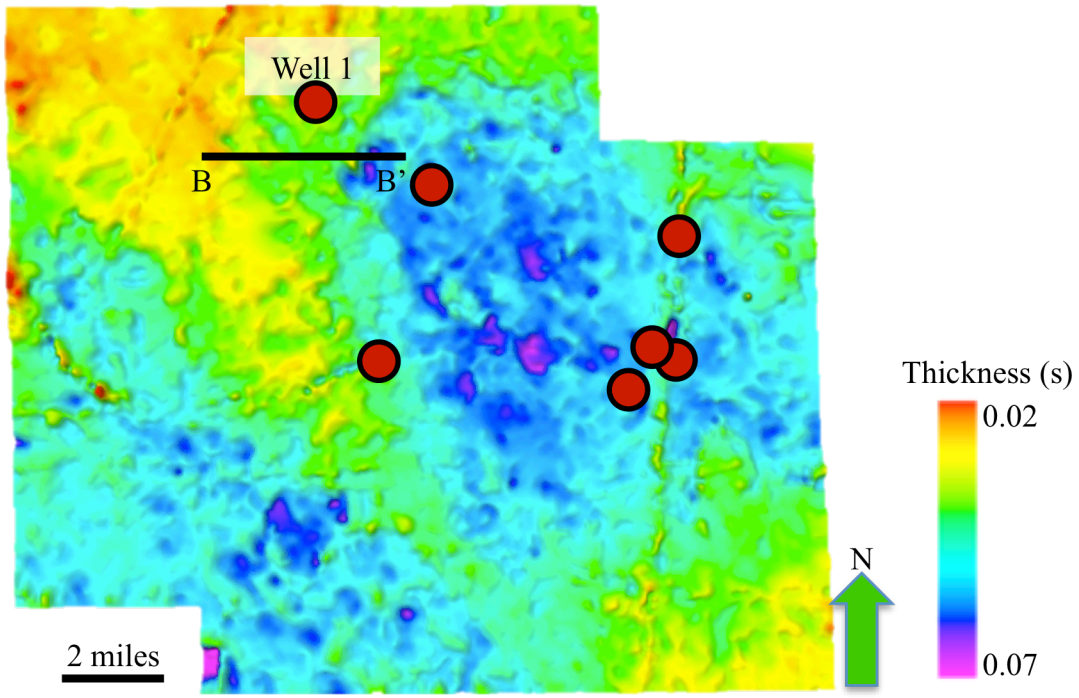

Figure 3.3-1: Time thickness map of the Hunton Limestone which ignore any erosion along the top Woodford, approximates the paleo sea-floor topography. Thicker areas of the Woodford Shale correspond to thinner areas of Hunton Limestone. Vertical slices along line BB' are shown in Figure 3.3-4. Circles indicate seven wells used for the impedance inversion of the prestack seismic data discussed later. Well 1 is a cored well.

I have flattened the seismic volume along the top of the Woodford in order to remove most of the rugged topography on the Hunton Limestone resulting from post-depositional tectonic deformation. Figure 3.3-4 shows a slice through the areas least affected by the tectonic activity in order to illuminate the original basin geomorphology at the time of Woodford deposition. Ideally, a detailed structural restoration is needed to fully reconstruct the basin geometry of the Woodford Sea. However, given the overall dip of 2° the flattened volume provides sufficient insight into the depositional processes at a regional scale. Figure 3.3-5 shows a suite of volumetric seismic attributes computed from this flattened volume to illuminate highly paleotopographic anomalies. High coherent seismic energy and high $\mu\rho$ values (Figure 3.3-5a and b) calculated from the impedance inversion of the pre-stack 3D surface seismic volume (Figure 3.3-5a) correspond to the remnant Hunton Limestone, present as topographic highs in the Woodford Sea. Stratal slices through the co-rendered high curvature values and coherent seismic energy (Figure 3.3-5d) show strong negative curvature values in juxtaposition with areas with high seismic energy. Such correlations suggest that these paleo lows are filled with higher impedance quartz-rich sediments.

This rugged Hunton paleo topography formed the rugged basin floor topography of the Woodford Sea. The Woodford Shale was deposited as the sea progressively transgressed onto the unconformity surface with depressions on the sea-floor inundated earlier compared to topographically high areas. Figure 3.3-6 was chosen over an area with no visible faults or folds and is thus unaffected by the post-Woodford tectonic deformation and thereby preserving the original basin floor topography. Although the top Woodford is also an unconformity, it is not deeply eroded. For this reason the time

thickness map in Figure 3.3-6 are good approximations to the paleo water bottom. Relatively thick accumulation of the Woodford Shale exists in topographically low areas of the basin while thinner Woodford interval exists in topographically high areas. Moreover, basin floor lows are likely areas for storm current/turbidity current related flows which give rise to the brittle cherty lithofacies identified in the subsurface cores deposits (Chapter 4 of this dissertation). Thus the overall organic-rich shale in the depressions often contains intervening brittle cherty lithofacies, which are absent in topographically higher areas. Such intervening cherty layers are critical for initiating hydraulic fractures and producing hydrocarbons from impermeable shale reservoirs.

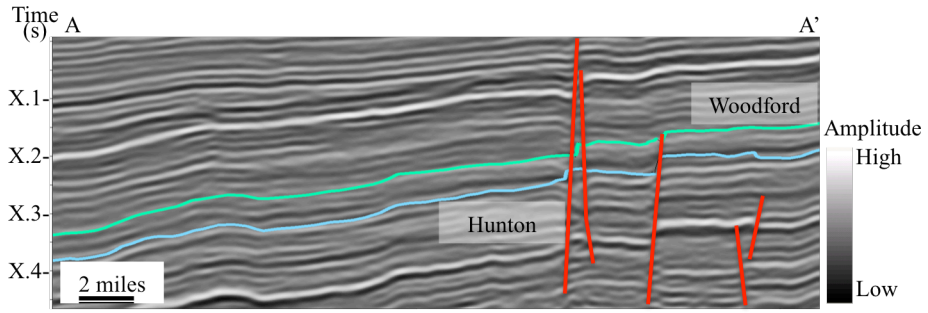

Figure 3.3-3: Vertical slice along AA' through the seismic amplitude volume showing the Woodford Shale and the underlying Hunton limestone. Faults cutting through these two horizons are marked with red lines. Location of the line is shown in Figure 3.2-1.

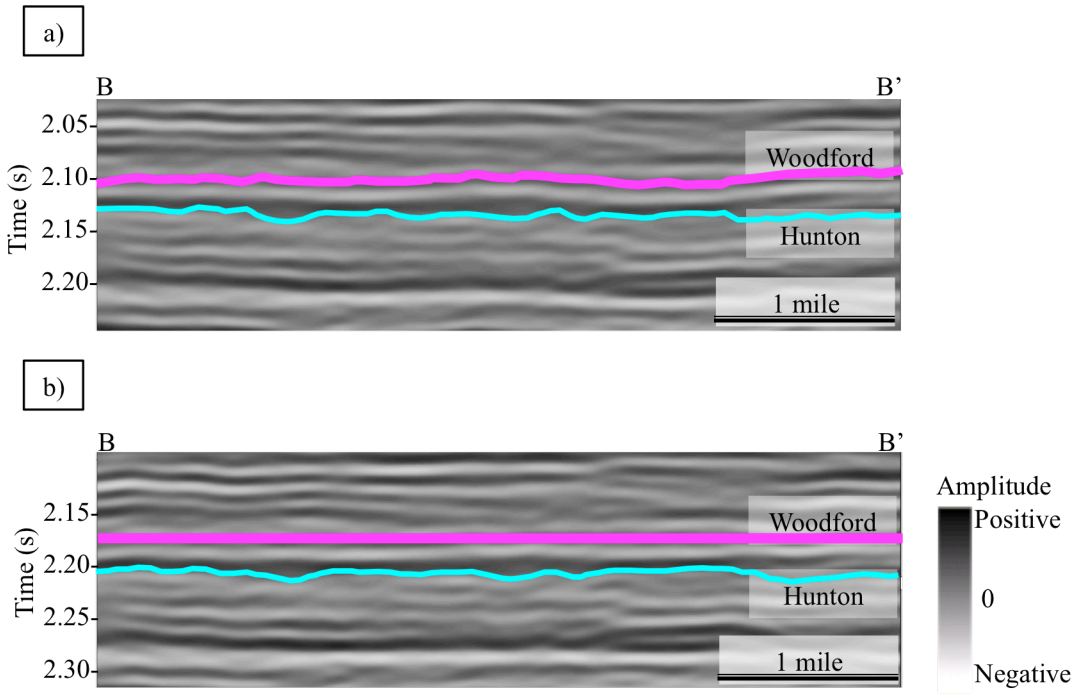

Figure 3.3-4: (a) Vertical slice along BB' through the seismic amplitude volume showing the Woodford Shale and the underlying Hunton limestone. (b) Seismic amplitude volume flattened along the top of the Woodford showing the Woodford Shale and the underlying Hunton limestone.

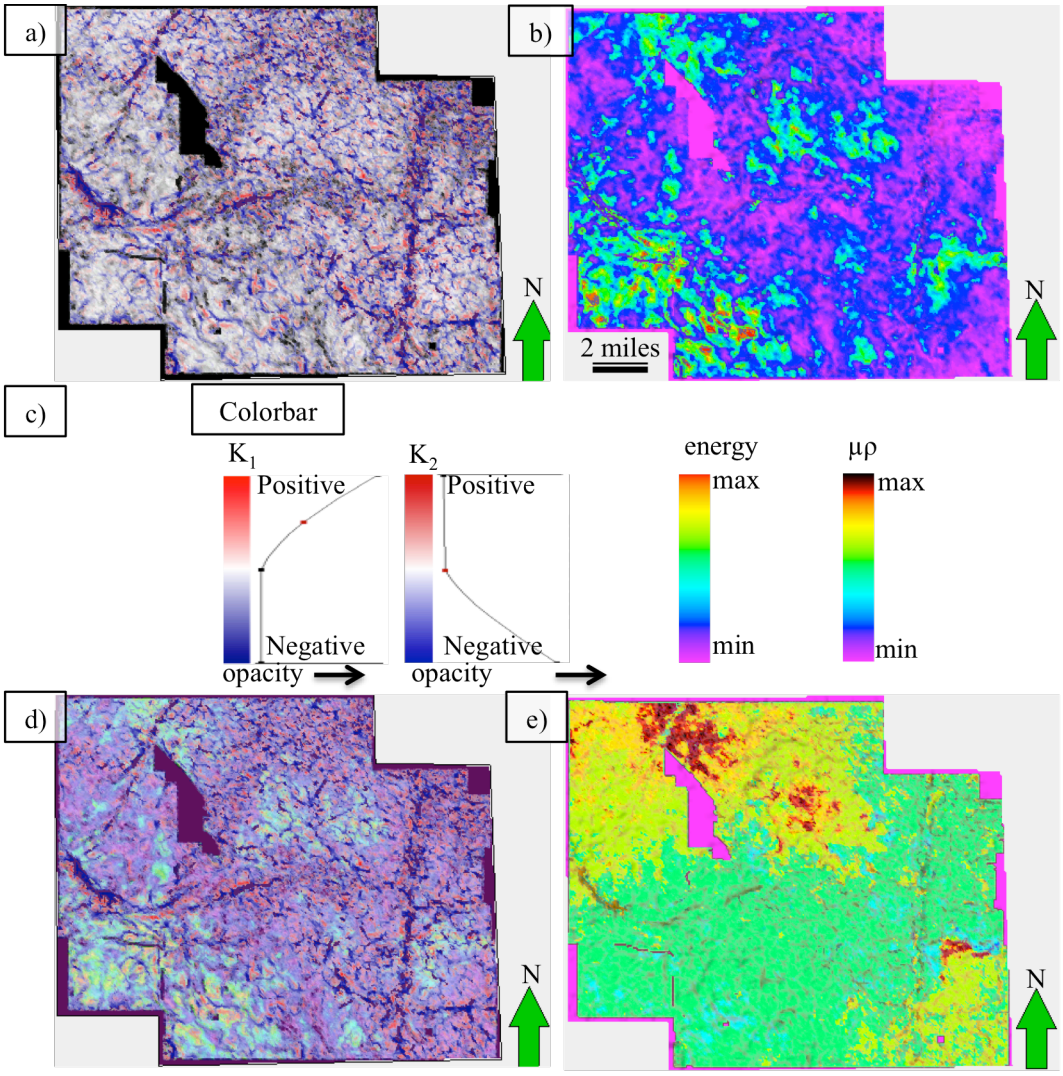

Figure 3.3-5: Horizon slices through the attributes calculated from a seismic volume flattened along the top of the Woodford Shale such that the top of the Hunton Limestone reflects the geomorphologic features of the basin floor during Woodford deposition. (a) Horizon slice through the co-rendered most positive (k_1) and most negative (k_2) principal curvature attribute volumes. (b) Horizon slice through the coherent seismic energy attribute volume. (c) Colorbars used in Figures a, b. (d) Horizon slice through the co-rendered most positive (k_1) and most negative (k_2) principal curvatures, and coherent seismic energy attribute volumes. The coherent seismic energy attribute volume is rendered transparent (~50%) in this figure. (e) Horizon slice through the $\mu\rho$ impedance inversion. Note the areas with high $\mu\rho$ values match with higher values for the coherent seismic energy shown in Figure b.

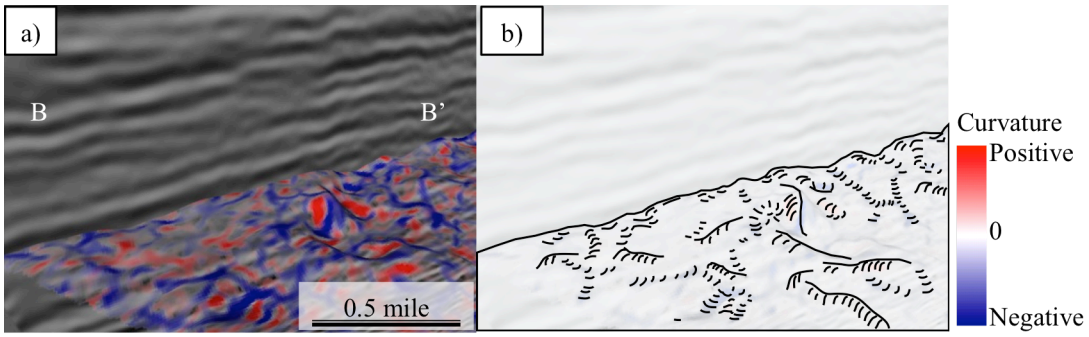

Figure 3.3-6: (a) 3D display of a horizon slice through most positive and most negative principal curvatures with a vertical slice through seismic amplitude. Curvature computed and image capture from seismic volume flattened along the top of Woodford. (b) Schematic diagram drawn from the curvature expression of the horizon in (a) showing the rugged sea-bed topography of the Woodford Sea as defined by the unconformity surface on the top of the Hunton Limestone. Location of BB' is shown in Figure 3.3-1.

Core analyses indicate three petro-types within the Woodford Shale, based on subtle changes in petrophysical properties (Chapter 1 of this dissertation). These petro-types are only loosely connected to elastic parameters detected by seismic data. Lithologic heterogeneity results in laterally highly variable impedance contrasts posing challenges for high-precision horizon picking. My analyses show that volumetric seismic attributes help to map subtle but important stratigraphic components especially when calibrated with well-logs and core measurements mapping the components in order to facilitate the construction of the depositional history. To this end, I examined 20 Woodford stratal slices through co-rendered coherent seismic energy and in-line energy gradient volumes in order to track stratigraphic changes in the study area. Five of these slices are shown in Figure 3.3-7. Low seismic energy areas (magenta and blue colored) in Figure 3.3-7a represent the initial shale deposition on top of the high seismic energy

Hunton Limestone. Structural lows on the sea floor were inundated earlier, are affected by storm and turbidity currents, as well as debris flows resulting into thin intervals of quartz rich silty deposits rather than only clay-rich suspension fallout. Areas marked with orange ellipses on Figure 3.3-7a and b indicate that shale deposition didn't start until the beginning of Middle Woodford deposition (Figure 3.3-7c). The high seismic-energy areas contained by white polygons on Figure 3.3-7d, and e are areas with possible silica enrichment within the Woodford Shale which are otherwise characterized by low seismic energy (Figure 3.3-7a, b, and c). Such an increase in silica in the Upper Woodford is in accordance with the cherty Upper Woodford intervals reported in the literature (Chapter 4 of this dissertation).

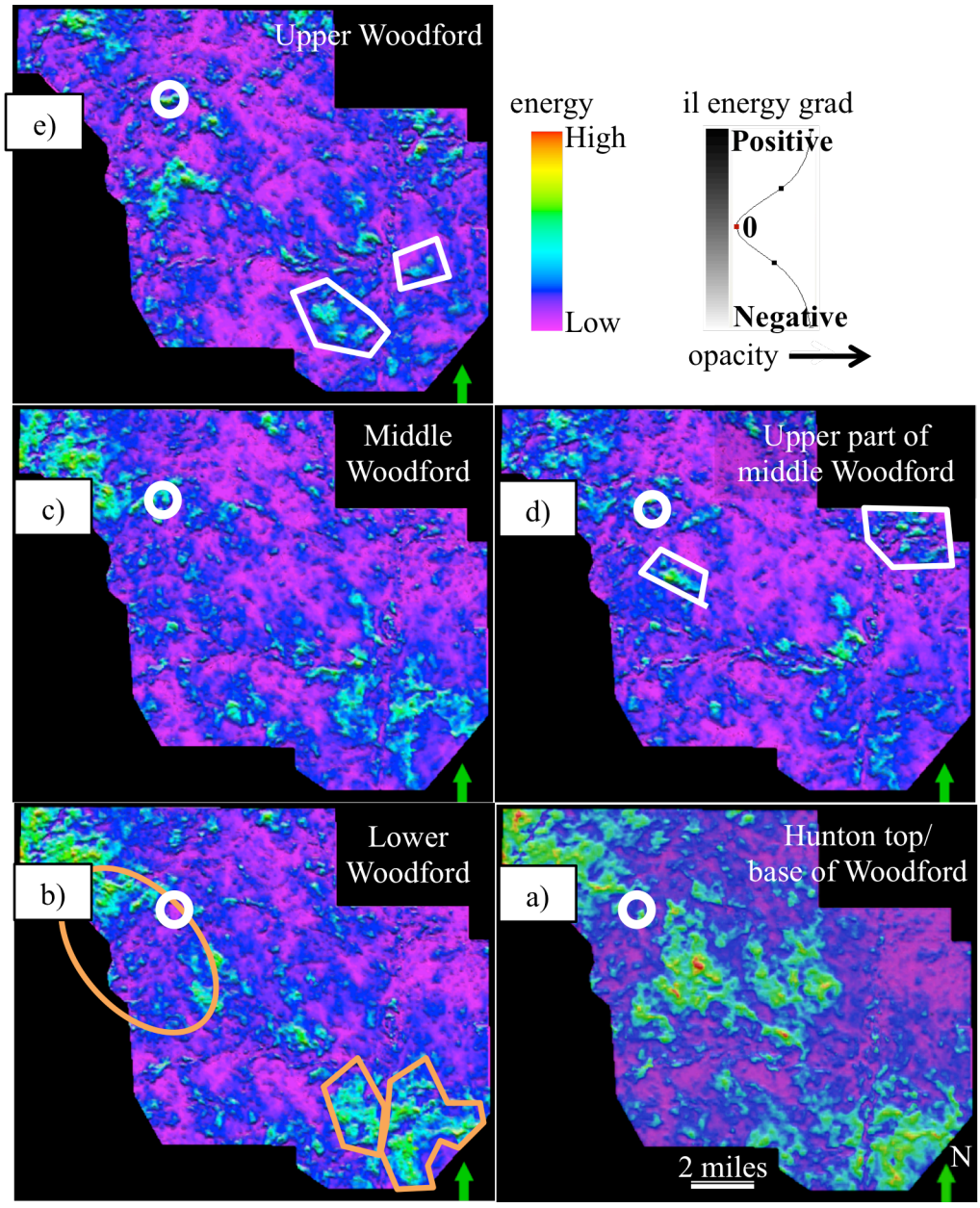

Figure 3.3-7: Stratal slices generated by co-rendering coherent energy with in-line energy gradient. Figures from bottom to top represent top of the Hunton unconformity, in the middle of the Woodford Formation and near the top of the Woodford Formation respectively (a, b, c). Notice the subtle high seismic-energy nature (represented by cyan color) in the top-most stratal slice. (c) may be indicative of richness in biogenic silica concentration as reported in the literature (Chapter 4 of this dissertation). White circle indicates location of the cored well.

3.4 Prediction of elastic rock types from seismic inversion

Core measurements of elastic moduli and organic carbon content (TOC) indicate that the Woodford Shale can be grouped into three elastic petro-types containing high, intermediate and low organic carbon content (TOC) on a Young's modulus versus Poisson's ratio crossplot (Figure 3.4-1a). Comparison between elastic moduli calculated from ultrasonic core measurements and well logs from well 1 (mentioned in chapter 1 of this dissertation) helped to map these three petro-types to the well log scale (Figure 3.4-1b) and ultimately to the seismic scale.

I performed simultaneous angle dependent inversion (Hampson et al., 2005) of the pre-conditioned prestack seismic gathers in order to estimate elastic properties from the seismic data. Fatti et al.'s (1994) modification of Aki and Richard's (1980) approximation of the Zeoppritz equations provide the basis for this inversion technique. The inversion was achieved through five steps: (i) selecting wells located across the seismic survey, (ii) generating angle gathers from the offsets, (iii) extracting representative wavelets for each angle to generate synthetic seismic which ties at the wells, (iv) modeling low frequency components of the P- and S-impedances from well logs and seismic data, and ultimately (v) inverting the seismic data. Locations of the wells used for the seismic inversion are shown in Figure 3.3-1.

Crossplots of Young's modulus, E and Poisson's ratio, ν, from impedance inversion of pre-stack 3D surface seismic data are shown in Figure 3.4-1c. Note, the higher E values calculated from ultrasonic measurements made on horizontal core plugs compared to values calculated from well-logs from vertical wells can be attributed to the transverse isotropic nature of the shales.

Core measurements indicate that TOC-rich rocks are ductile and TOC-lean rocks are brittle. The TOC-lean rocks typically occur as cherty lithofacies within the Woodford Shale (Chapter 4 of this dissertation). Detailed core analyses highlight intervals containing alternating TOC-rich ductile rocks and TOC-lean brittle rocks within well 1 (discussed in chapter 1 of this dissertation) which are identified as ideal intervals for placing horizontal wells within the Woodford Shale.

Figure 3.4-2 shows maps of the three elastic petro-types within the study area. The middle Woodford member contains high amounts of petro-type with intermediate TOC. Such characteristics of the middle Woodford matches with the geologic history (Chapter 4 of this dissertation). The middle Woodford member is likely to contain the highest amount of brittle-ductile rock couplets (core description in chapter 4 of this dissertation) for most of the study area and hence, generate an average response for the petro-types with intermediate TOC. It is possible to correlate the elastic petro-types with the petro-types identified using mineralogy in the petrophysical analyses (Chapter 1 of this dissertation) through incorporating more well-log information. Such additional information will ultimately lead to integrated 3D reservoir descriptions and 3D mechanical properties and illuminate the sweet spots within the Woodford Shale.

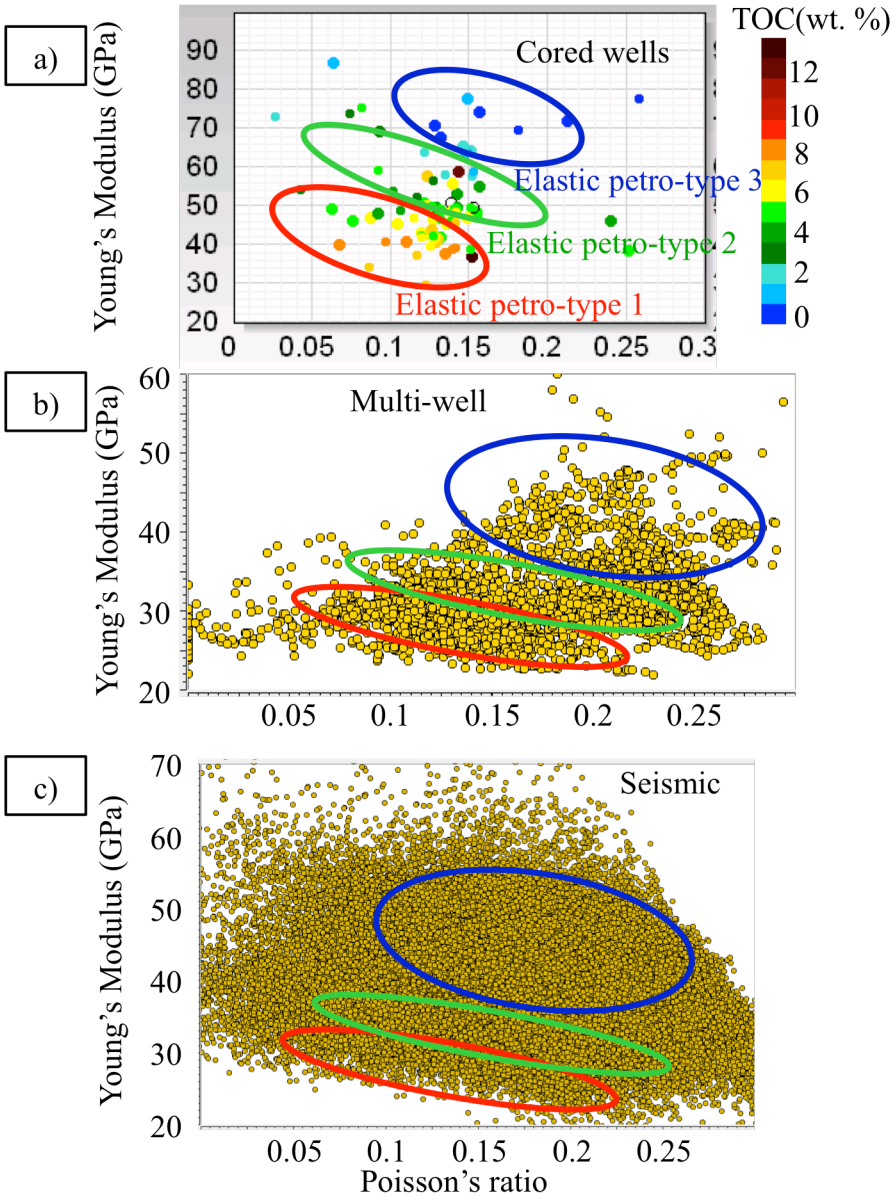

Figure 3.4-1: Crossplots of Young's modulus (E) and Poisson's ratio (v), (a) from core measurements, (b) from logs in 12 wells, and (c) prestack seismic inversion. Crossplots indicate comparatively narrow range of v and wider range for the E. (a) Three rock types identified from core measurements. Data values are color coded by total organic carbon (TOC). Note the TOC-rich rocks (red ellipse) have lowest range of Young's modulus and hence, are ductile in nature compared to more brittle TOC-lean rocks (blue ellipse). Rock types from core data are transferred to well data and seismic data crossplots.

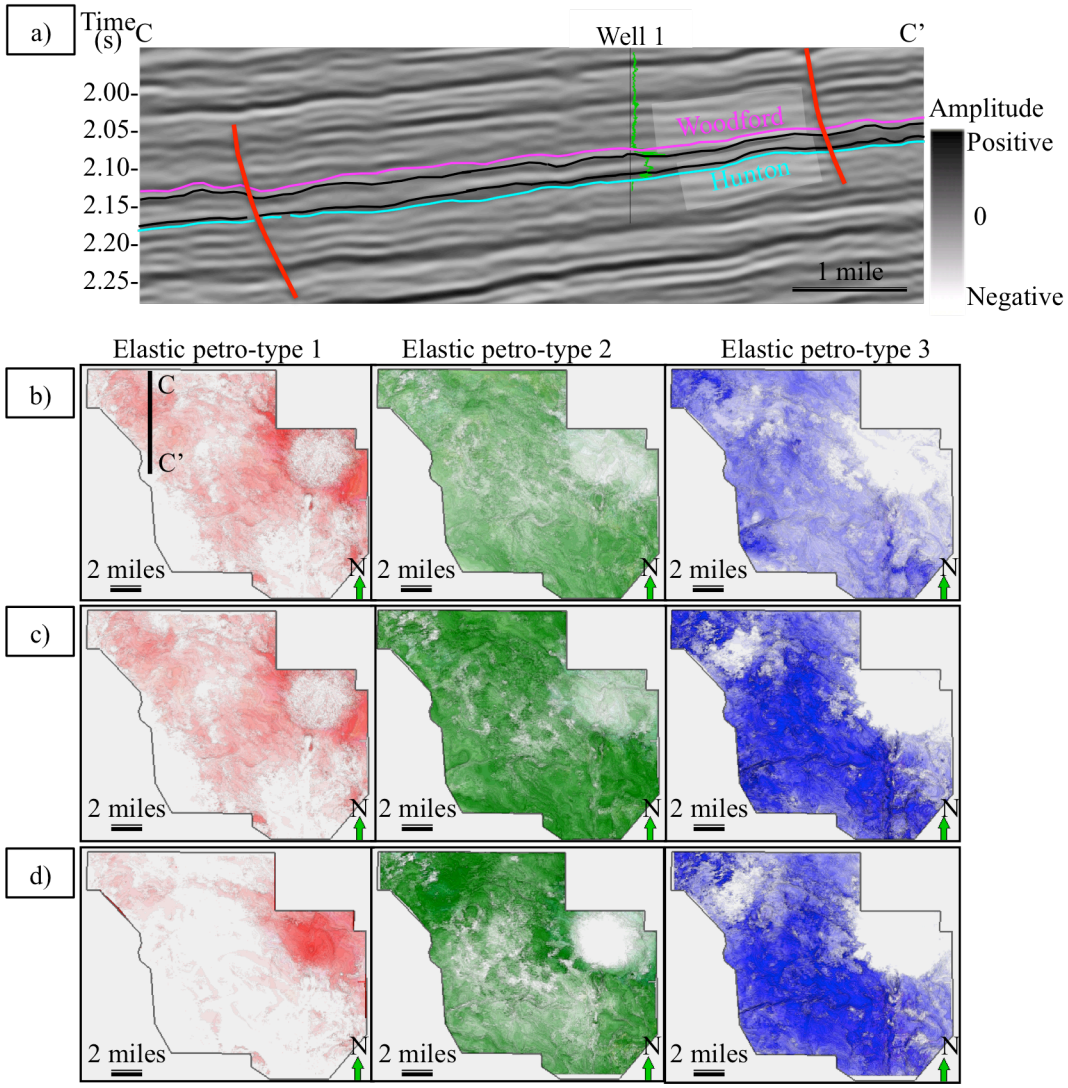

Figure 3.4-2: (a) Vertical slice through the seismic amplitude volume showing the relative location of the base of the Woodford located on top of the Hunton Limestone (cyan), top of the lower Woodford (black), top of the middle Woodford (black), and top of the upper Woodford (magenta) on a vertical seismic line CC'. Gamma ray from well 1 is plotted as green curve on this figure. (b), (c), and (d) Maps of three elastic petro-types one through three from left to right. Each of these petro-types are characterized by unique ranges of Young's modulus and Poisson's ratio corresponding to rocks with different TOC and quartz content as shown on the previous Figure. with red, green and blue ellipses on Young's modulus and Poisson's ratio crossplots in the previous figure. (b), (c) and (d) are maps of elastic petro-types within the upper, middle and lower Woodford members respectively.

3.5 Tectonic deformation and natural fracture distribution

Natural fractures play a critical role in the evaluation of tight, low-permeable resource-shales. Open fractures often improve the host rock's permeability while mineral-filled fractures often provide weak areas in rocks that are more amenable to artificial fractures. Natural fractures can also affect reservoir performance in a negative way. For example, in the Barnett Shale natural fractures may connect to the underlying Ellenburger aquifer (Schuelke, 2011). Structural deformation seen on seismic data (Figure 3.3-3), the tectonic history derived from outcrop studies (Arroyal, 2009) along with detailed core descriptions indicate that major, multi-stage tectonic activity affected the Woodford Shale in the study area resulting in highly deformed areas and a heterogeneous distribution of natural fractures in the study area. Volumetric seismic attributes highlight areas with fault offsets, folds, flexures and areas with rotated fault blocks. Such attributes are a direct measure of strain, which is one of the key components in mapping natural fractures (Nelson, 2000).

Figure 3.5-1 highlights faults and the irregular unconformity surface at the base of the Woodford Shale (which is also the top of the underlying Hunton Limestone) in a horizon slice through Sobel filter similarity, an edge-detecting attribute. Detailed structural analysis of the north-south trending Fault on Figure 3.5-1 indicates that it is a strike-slip fault. Clay model experiments show similar reidel shears. Collapse features in the Hunton Limestone highlighted by the Sobel filter similarity (Figure 3.5-1) form low areas (Figure 3.3-6) on the Woodford Sea characterized by high curvature values (Figure 3.3-5) and likely not only to be significantly fractured but also accommodate thicker Woodford Shale succession.

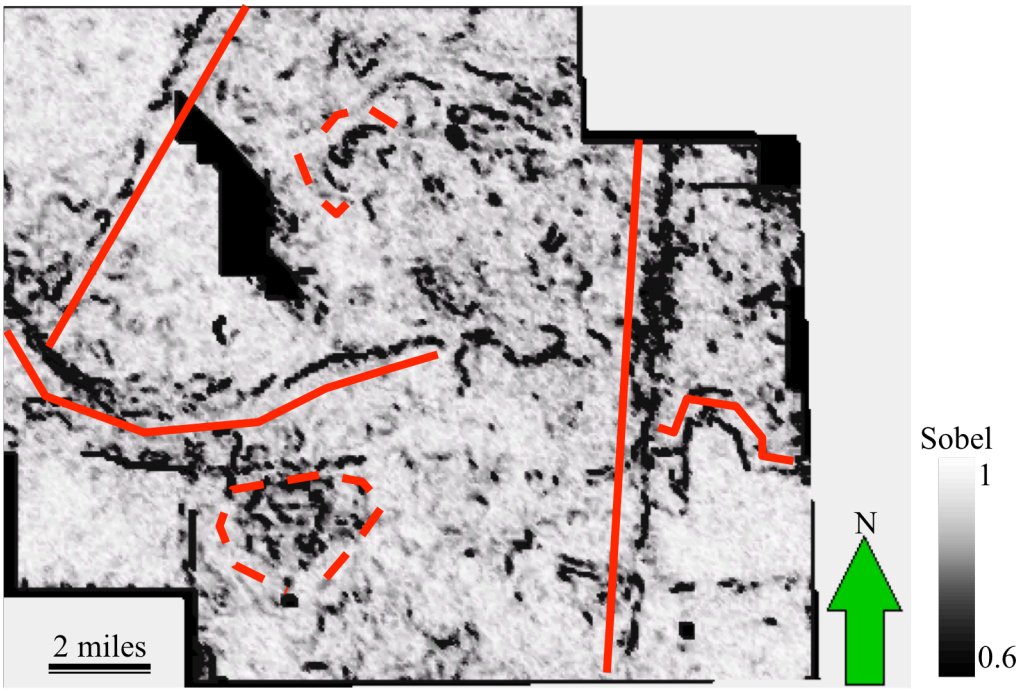

Figure 3.5-1: Horizon slice through the Sobel filter similarity attribute volume along the underlying Hunton Limestone over which the Woodford Shale was deposited. Solid red lines indicate faults while the dashed red lines indicate some of the collapse features.

Murray (1968) correlated natural fractures and improved production from the Bakken formation of North Dakota with curvature obtained from well tops and 2D seismic data. In this study, I have used the positive and negative principal curvatures instead of the more popular curvature attributes. The principal curvatures exhibit anomalies along the tightest synclinal and anticlinal components of a fold, independent of the fold orientation with respect to the vertical. I have used the most positive and most negative principal curvatures to highlight potential areas for higher number of natural fractures. Guo et al. (2010) correlated natural fractures and the curvature attribute in the Woodford Shale of the Arkoma Basin.

Multi attribute analyses through co-rendering of geometrically independent and interpretationally complementary attributes highlight potential areas with natural fractures. Co-rendered Sobel filter similarity and most positive and most negative principal curvatures highlight the potential natural fractures (Figure 3.5-4).

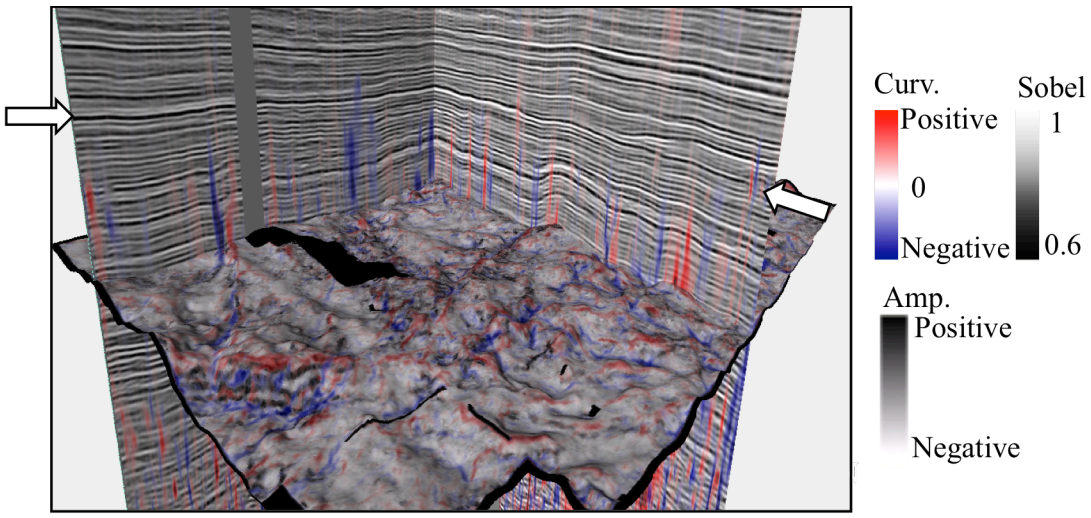

Figure 3.5-2: Chair display showing vertical slices through seismic amplitude co-rendered with most-positive and most-negative principal curvature volumes and horizon slices along the top Hunton through the coherence and most-positive and most-negative principal curvature volumes. Black polygons indicate no data permit areas in the survey. Faults seen on the vertical sections do not exhibit a strong lateral discontinuity such that the appearance on the coherence image is muted. Note that the faults do not continue into the overlying Red Fork formation indicated by the white arrows.

Amplitude curvature (Figure 3.5-3) highlights lateral changes in reflectivity and is independent from structural curvature. Amplitude curvature often highlights joints in carbonates and large cleats in coals. Such lineaments are due to either local stress release or diagenetic alteration of a zone sufficiently large to be seen by surface seismic data.

The strike of the most-negative principal curvature, $\psi_{k2,}$ modulated by the magnitude of the most negative principal curvature, k_2, (Al-Dossary and Marfurt, 2006) shows the progressive change in lineament strike from NE-SW to NW-SE across the survey within the Woodford Shale interval (Figure 3.5-3). Such changes in strike indicate non-planar fault planes and subsequent twisting of the Woodford Shale.

The reflector rotation with respect to reflector normal attribute volume further shows such "twisting" and maps the relative movements of the fault blocks with respect to each other (Figure 3.5-4). Marfurt and Rich (2010) discuss the mathematical background for the calculation of this attribute.

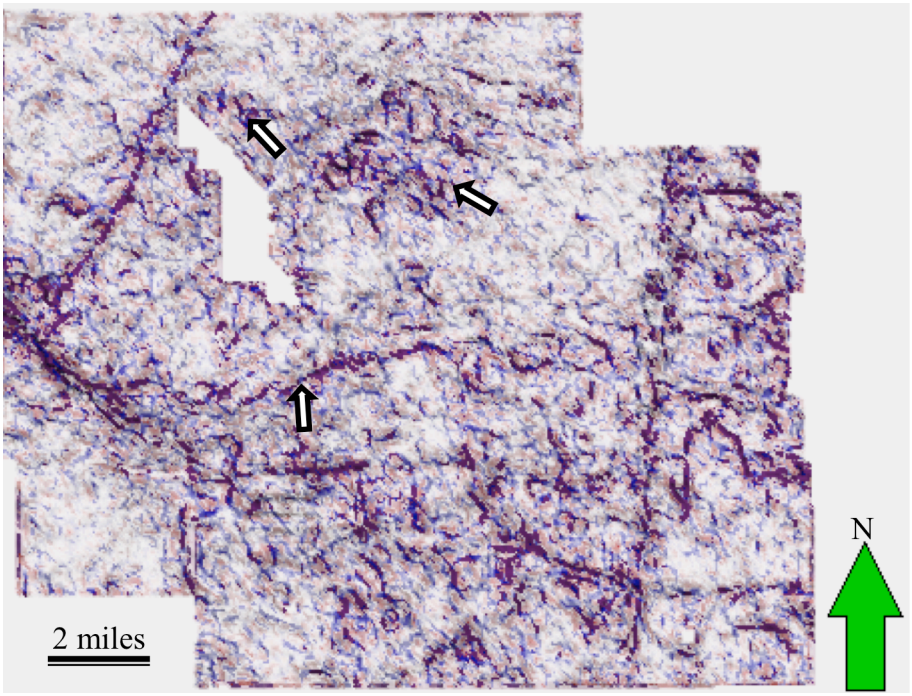

Figure 3.5-3: Co-rendered horizon slice along the top of the Hunton through the most-positive curvature and most-negative curvatures of seismic amplitude. Areas with strong curvature correspond to strong lateral changes in amplitude and are sensitive to strain release and diagenetic alteration about fractures.

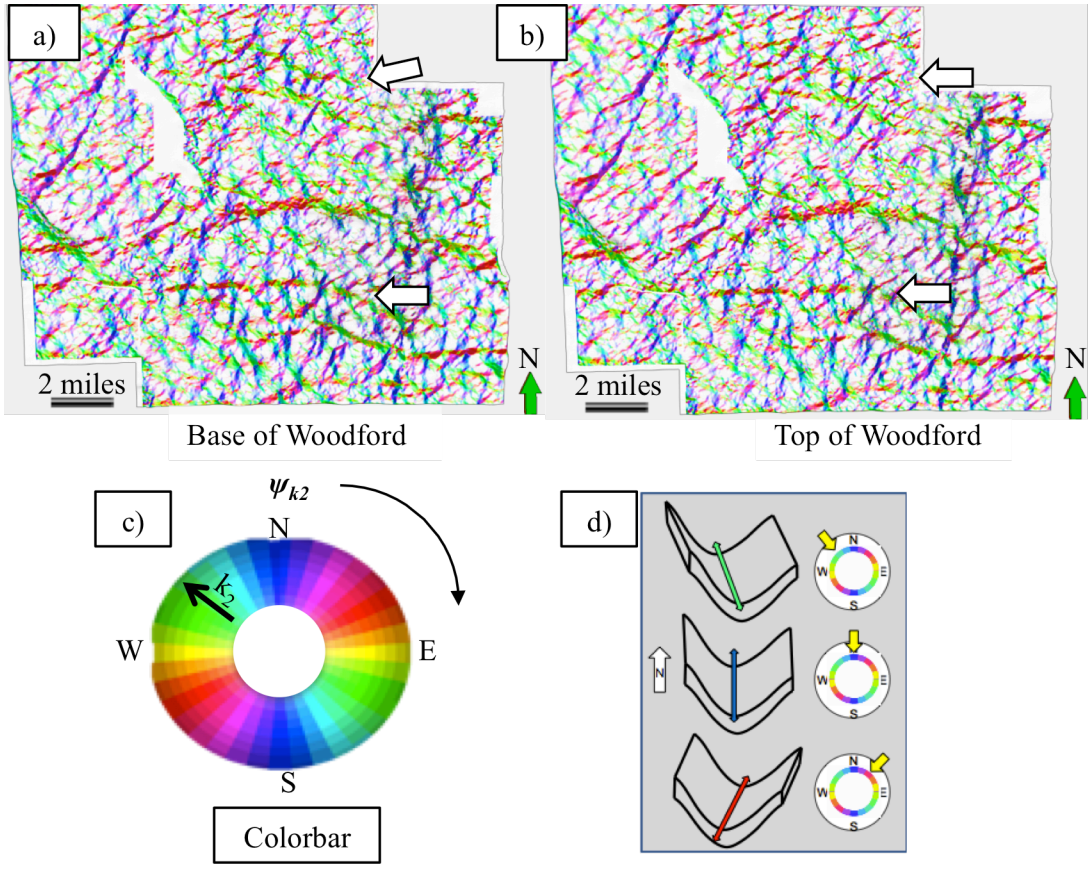

Figure 3.5-4: Horizon slice through the strike of the most-negative principal curvature, ψ_{k2}, (plotted against hue) modulated by the magnitude of the most negative principal curvature, k_2. (a) 10 ms above the Hunton top and (b) near the Woodford top using (c) a 2D colorbar and making the low curvature values transparent. (d) Cartoon illustrating a valley trending NW-SE colored cyan (top), a valley trending NS colored blue (middle), and a valley trending NE-SW colored magenta (bottom). Note the change in the orientation (indicated by white arrows) of the lineaments in the Woodford compared to the Hunton, indicated by white arrows.

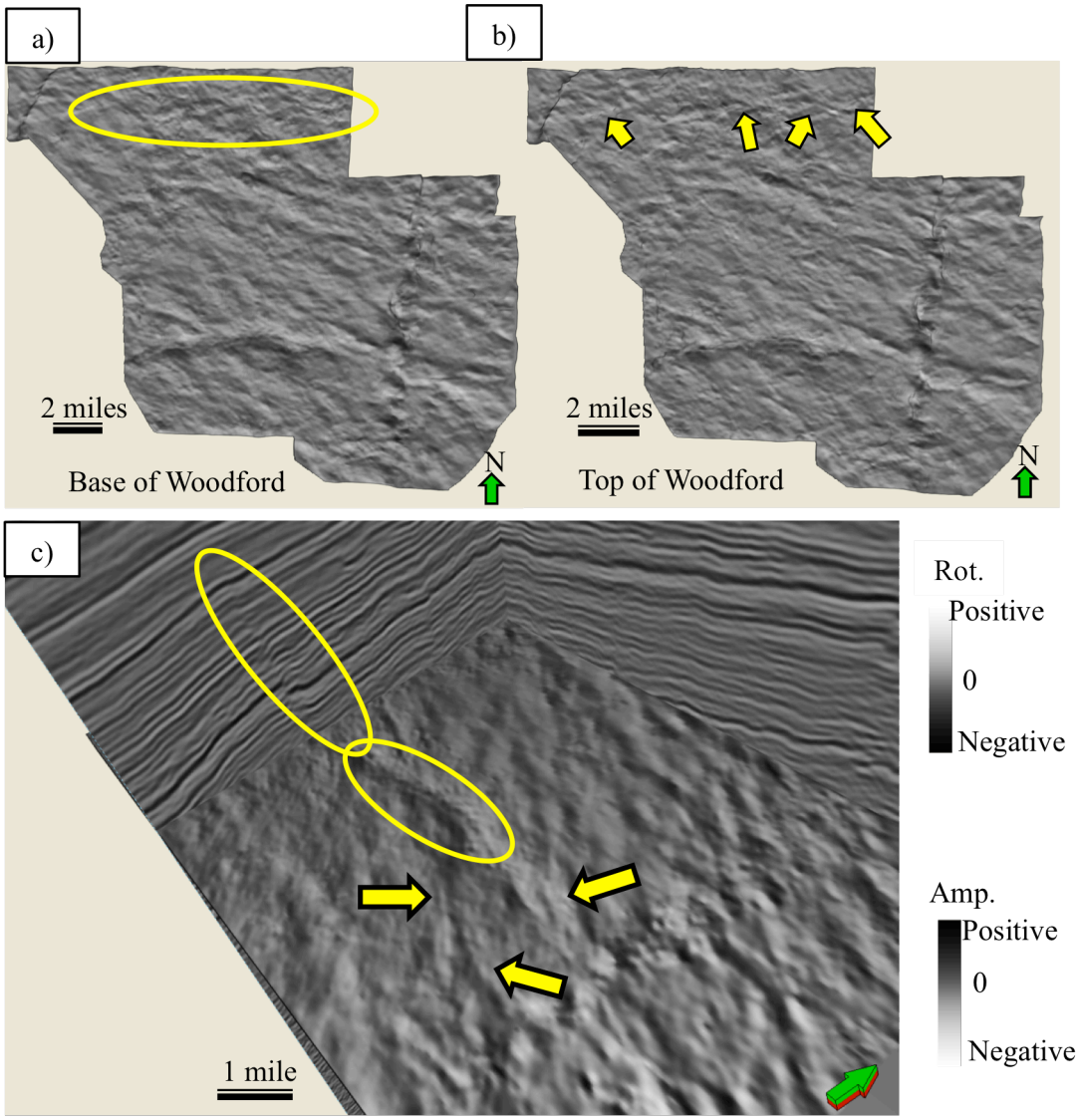

Figure 3.5-5: Reflector rotation about the average reflector normal. The horst and graben blocks show considerable contrast and can be interpreted as separate units. (a) Horizon slice at t = 10 ms above the top of the Hunton Limestone, and (b) horizon slice near the top of the Woodford Shale. Ellipse and arrows on Figures a and b indicate progressive changes in the fault block rotation from the base to the top of the Woodford Shale. (c) Chair display of a time slice through reflector rotation about the average reflector normal and vertical profiles through seismic amplitude. Yellow ellipses show the same fault seen on the vertical slice through the seismic amplitude volume and on the time slice. Yellow arrows indicate a number of fault branches connected to a parent fault block.

Guo et al. (2010) used the shape index modulated by curvedness attribute volume to illuminate surface irregularity of the Woodford Shale in the Arkoma Basin. They showed that anticlinal areas of a reflector (ridges and domes) are most likely areas for the microseismic events and most likely following higher number of natural fractures in those areas (Figure 3.5-6). Thompson (2010) showed the opposite phenomenon in her work on the Barnett Shale where microseismic events were concentrated in bowl-shaped structures. Similarly, I have used the same attribute to quantitatively highlight the shapes of seismic reflectors and highlight ridges and domes as potential areas for higher number of natural fractures. I have shown a co-rendered image of shape index modulated by curvedness and seismic amplitude delineating the similarity between reflector shape and the calculated shapes of reflectors in Figure 3.5-7. Bowl-shape collapse features are possibly associated with the collapse of Hunton Limestone appear blue (blue arrow) and areas of thicker accumulation of the Woodford Shale.

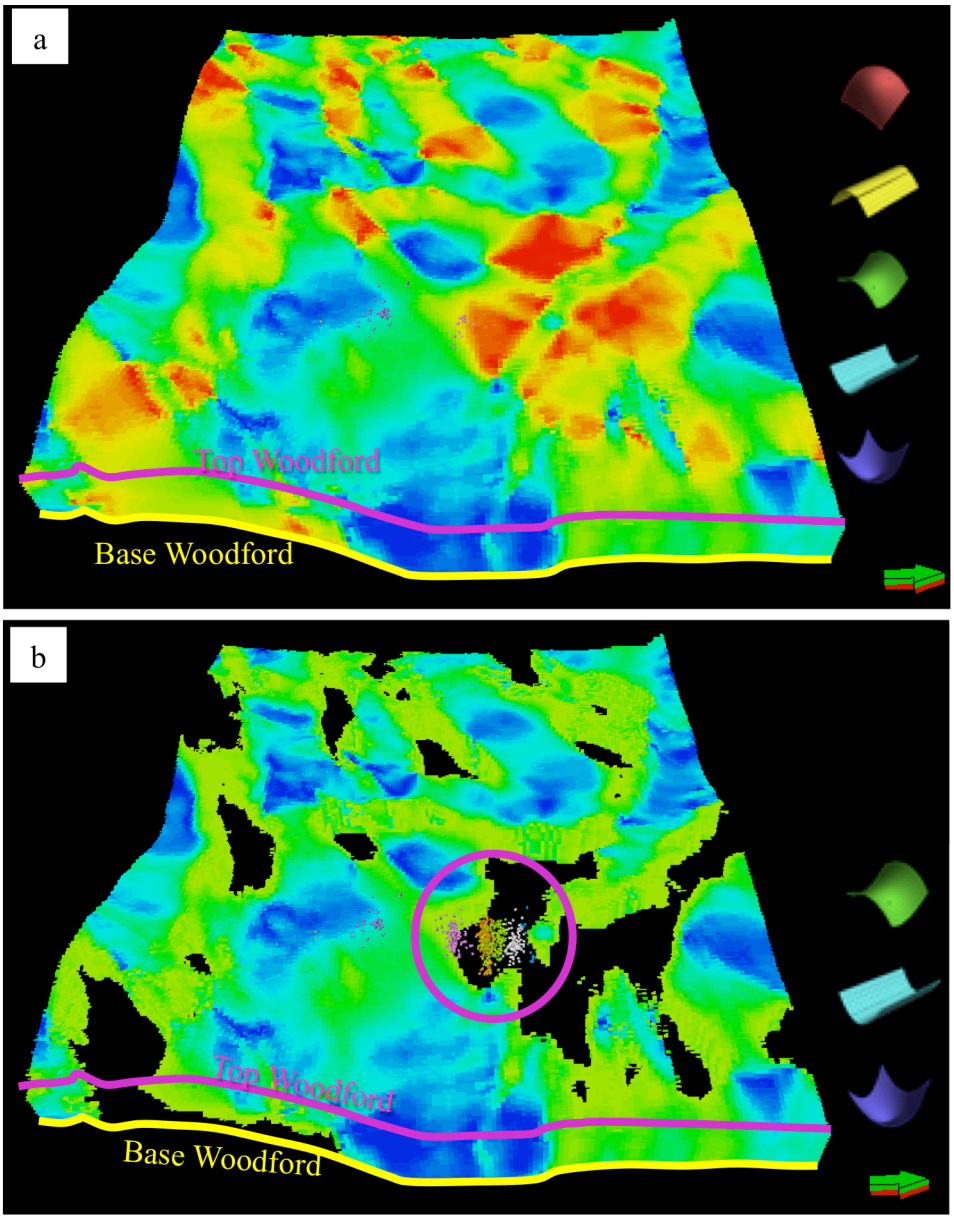

Figure 3.5-6: (a, b) Co-rendered horizon slice through the shape index modulated by curvedness and microseismic events. (b) Microseismic events are visible when the dome and ridges are rendered transparent indicating favorable areas for artificial fracturing in those areas and are also possible areas for higher number of natural fractures. Figure is modified from Guo et al., 2010; Microseismic courtesy of Pablo LLC; Seismic data courtesy of CGG-Veritas.

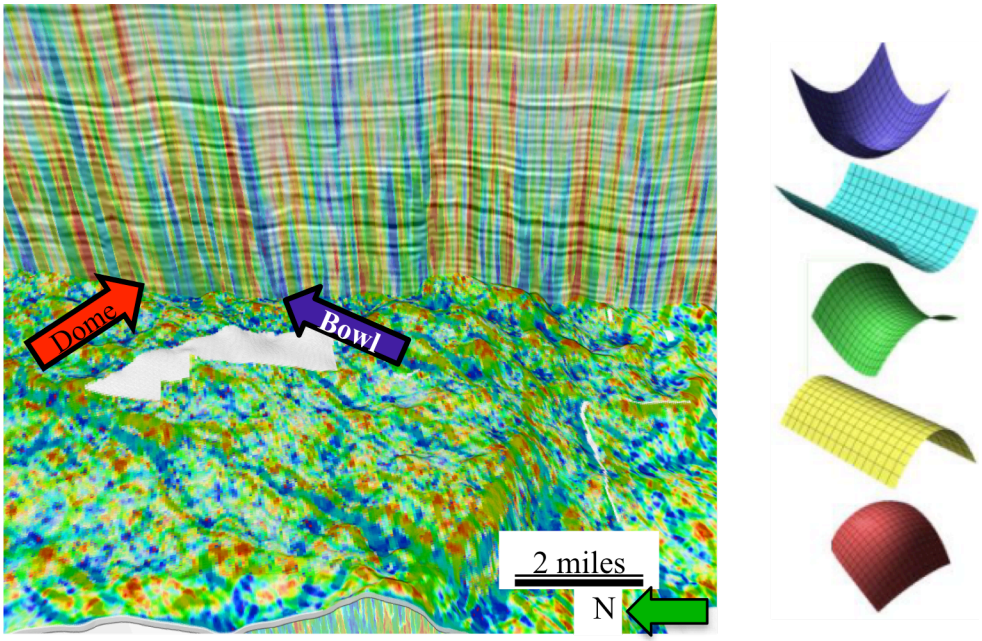

Figure 3.5-7: Chair display of shape index modulated by curvedness co-rendered with seismic amplitude. Red (dome) and blue (bowl) indicate irregularities associated with the unconformity surface. The base of the Woodford is shown as horizontal display. Note the correlation of the reflector shape attribute with the structure seen on the vertical slices through the seismic amplitude.

3.6 Conclusions

Seismic data provide the most promising means to extend core and well log measurements to map three-dimensional distributions of hydrocarbon reservoirs. Seismic geomorphology provides a means to define the depositional environment. Prestack seismic inversion, calibrated to core and logs provide estimates of petro-types at a regional scale. Geometric attributes indicate areas more prone to natural fractures.

Due to the competitive acreage positions at the time of this thesis, I do not have access to the dense well control common to shale resource plays. Horizontal image logs can provide direct correlations between impedances, curvature, and natural fractures. The seismic data used in this study are from a megamerge with 70% of my study area covered by low-fold narrow azimuth 1994-1996 surveys that cannot be used to estimate azimuthal or vertical transverse anisotropy. The hundreds of triple combo well logs can provide the statistical control for high-resolution neural network estimation of petro-types. Microseismic measurements provide direct evidence of brittle versus ductile behavior. My hope is that as these data are released for publication, others can build on my preliminary analysis.

References

Aki, K., and P.G. Richards, 1980, Quantitative seismology: Theory and methods: 1,W.H. Freeman and Company.

Al-Dossary, S., and K. J. Marfurt, 2006, 3D volumetric multispectral estimates of reflector curvature and rotation: Geophysics, 71, P41-P51.

Arroyal, R. M. P., 2009, Characterization and origin of fracture patterns in the Woodford Shale in southeastern Oklahoma for application to exploration and development,

Masters Thesis, The university of Oklahoma, Norman.

Chopra, S. and K. J. Marfurt, 2010, Interpreting fractures through 3-D seismic discontinuity attributes and their visualization: AAPG international convention and exhibition.

Comer, J. B., 2008, Distribution and source-rock characteristics of Woodford Shale and age-equivalent strata: AAPG Annual Convention and Exhibition.

Energy Information Administration, 2011, Review of emerging resources: U.S. shale gas and shale oil plays, ftp://ftp.eia.doe.gov/natgas/usshaleplays.pdf.

Fatti, J.L., G.C. Smith, P.J. Vail, P.J. Strauss, and P.R. Levitt, 1994, Detection of gas in sandstone reservoirs using AVO analysis: a 3D seismic case history using the geostack technique: Geophysics, 59, 1362-1376.

Guo, Y., K. Zhang, and K. J. Marfurt, 2010, Seismic attribute illumination of Woodford Shale faults and fractures, Arkoma Basin, OK: 80th Annual International Meeting of the SEG, expanded abstracts 1372-1376.

Hampson, D. P., B. H. Russell, and B. Bankhead, 2005, Simultaneous inversion of pre-stack seismic data: Proceedings of the 75th Annual International Meeting of the SEG; Expanded Abstracts, 1,633-1,637.

Johnson, K. S., 2008, Geologic history of Oklahoma: Educational publication, Norman, Oklahoma Geological Survey.

Marfurt, K. J., 2010, The shape of seismic interpretation: 29th Annual GCSSEPM Bob Perkins Conference on Seismic Geomorphology.

Marfurt, K. J. and J. Rich, 2010, Beyond curvature – volumetric estimates of reflector rotation and convergence, 80th Annual International Meeting, SEG, Expanded

Abstracts, 1467-1472.

Murray, G. H. Jr., 1968, Quantitative fracture study-Sanish Pool, McKenzie County, North Dakota: AAPG Bulletin, 52, 57-65.

Nelson, R. A., 2001, Geologic analysis of naturally fractured reservoirs, Gulf Professional Publishing.

Schuelke, J. S., 2011, Overview of seismic attribute analysis in shale plays: GCSSEPM, 31. 2011, 806-827, published online on February 9, 2012, doi: 10.5724/gcs.11.31.0806.

Sullivan, E. C., K. J. Marfurt, A. Lacazette, and M. Ammerman, 2006, Application of new seismic attributes to collapse chimneys in the Fort Worth Basin: Geophysics, 71, B111-B119.

Thompson, A. M., 2010, Induced fracture detection in the Barnett Shale, Ft. Worth Basin, Texas, Masters Thesis, The University of Oklahoma.

Chapter 4

4 Lithostratigraphic characterization and depositional setting of the Woodford Shale in west-central Oklahoma

4.1 Abstract

The Late Devonian-Early Mississippian Woodford Shale of the southern midcontinent was deposited in an epeiric sea, records a number of depositional cycles and associated lithologic changes. Slow sedimentation rate resulted into high frequency lithologic changes difficult to track from regular field measurements. Limited understanding about the depositional processes adds uncertainty and therefore increases risk in the exploration activities in the emerging Woodford Shale play. To address this issue, this paper presents an integrated study of a set of laboratory measured and field data from both hydrocarbon producing and non-producing wells and 3D seismic data from the northern part of the Anadarko basin where the Woodford Shale is characterized by high gas deliverability. Cores were subjected to visual core description, petrographic analyses, laboratory measured petrophysical properties (bulk density, grain density, porosity, mineralogy, total organic carbon [TOC], rock eval pyrolysis, acoustic velocities [V_p-fast, V_s-fast and V_s-slow], core gamma ray), scanning electron microscopic analyses (SEM), and then correlated to wireline logs.

In the study area, the Woodford Shale is made up of primarily two lithofacies: (1) black mudstone and (2) cherty lithofacies. High organic productivity during the Woodford deposition maintained reducing condition at the sediment-water interface and

resulted into overall dark color, high TOC, laminated Woodford Shale. Changes in the lithofacies, relative abundances of biogenic silica, and fossils versus kerogen, mineralogy, and density revealed 14 depositional cycles within the Woodford interval with the three individual members made up of 6, 4, and 4 cycles from base to top. All the major flooding events correlate with the eustatic sea-level curve curves. Such hot gamma ray measurements correlatable across wells from widely separated geographic areas and thus further confirm the global events. Depositional history when integrated with the seismic data indicate that depressions on the sea-floor were likely areas for the accumulation of the cherty lithofacies resulted from high energy current driven sedimentation. These preliminary findings provide components of a database that can be used to prioritize drilling prospects identified from surface seismic and production data.

4.2 Introduction

The late Devonian to early Mississippian Woodford Shale is an active shale-resource play. Although this shale formation has long been considered as the primary source rock for most of Oklahoma's hydrocarbon reserves, the depositional history and its correlation to reservoir petrophysical properties has not been established. A number of studies based on outcrop, laboratory and field data have shown the Woodford Shale to have a complex lithofacies distribution associated with variable amounts of TOC (Cardott and Lambert, 1982; Comer, 2008b; Comer, 1992; Fertl and Chilingarian, 1990; Hester and Schmoker, 1983; Hester et al., 1990; Kvale and Coffey, 2010; Lambert, 1993; Paxton et al., 2006; Sullivan, 2006). Comer (1992) lists the areas having greatest gas production potential and most prospective lithologies within the Woodford Formation to be the siltstone and silty black shale in the Anadarko Basin in Oklahoma, in the Delaware Basin

in Texas and New Mexico, and in the the Val Verde and Midland Basins in Texas; silty black shale in the Arkoma Basin in Oklahoma and Arkansas; and chert in the Frontal zone of Ouachita fold belt in Oklahoma. Major areas of thick Woodford accumulations include basins as well as uplifted areas in Oklahoma, Arkansas, Texas and New Mexico. Figure 4.2-1 shows the estimated resource potential of the Woodford Shale in Oklahoma (Comer, 2008b). Cardott and Lambert (1982) report that the depth of the Woodford Shale in the Anadarko Basin ranges from 5,060 ft on the northeastern shelf to 25,115 ft in the deepest part of the basin**;** thicknesses range from less than 25 ft in the northern shelf areas to more than 900 ft along the frontal Wichita fault zone. Vitrinite reflectance increases systematically with depth.

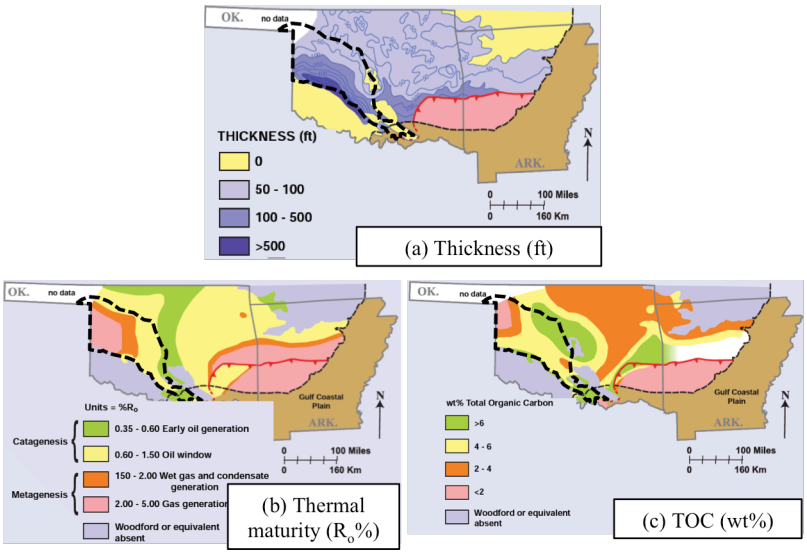

Figure 4.2-1: Map showing distribution of (a) thickness, (b) thermal maturity, and (c) TOC (wt%) of the Woodford and equivalent strata. Inscribed black dashed line delineates the extent of the Anadarko Basin. Modified from Comer (2008a).

Current study area focuses in west-central Oklahoma (Figure 4.2-2) where the Woodford Shale is about 200 ft thick. In this paper, I have developed a detailed depositional history, which can further be used to track the basin-wide correlations and lithologic changes. I start with petrographic observations, sedimentary and post-sedimentary structures, grain size distributions, and porosity. Next, I establish correlations between the petrophysical properties with the petrographic observations thereby defining principal petrophysical proxies for identifying syn- and post-depositional changes in the geologic processes. Finally, I correlate the cored wells to other wells in order to identify large-scale changes associated with the global sea-level curve.

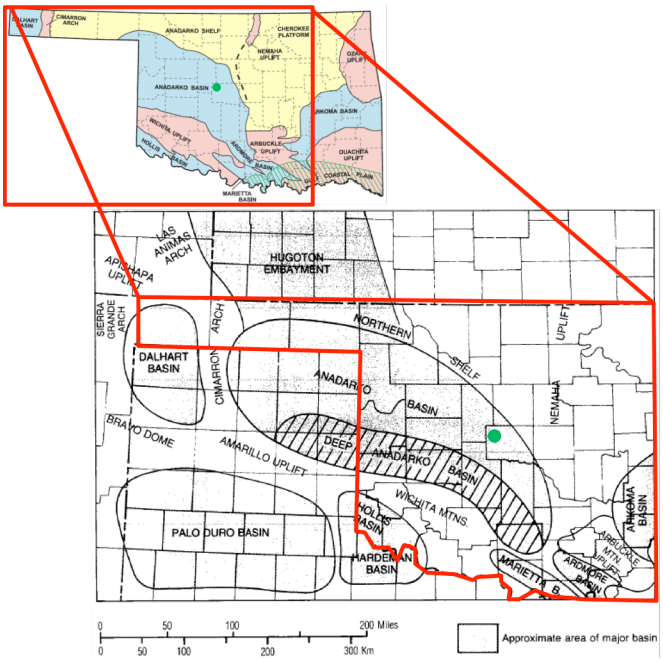

Figure 4.2-2: Major geologic provinces of Oklahoma. The enlarged map shows Anadarko basin and surrounding geologic provinces; outlined area in red marks a part of Oklahoma present in the enlarged figure. Green dot is the approximate location of the studied cored-well. Figures are modified from Johnson (1988).

4.3 Geologic framework

The late Devonian-early Mississippian Woodford Shale was deposited in an epeiric sea covering the huge Oklahoma basin extending over most parts of the southern Midcontinent (Figure 4.3-1) with the Anadarko basin being one of the protobasins of this ancestral Oklahoma basin. The Anadarko basin was formed as the Oklahoma basin was broken into a series of sharp uplifts and major basins during a post-Woodford, Pennsylvanian orogenic episode. The Wichita and Amarillo uplifts on the south, the Nemha uplift on the east, and the Cimarron arch on the west define the present day geographic boundary of the Anadarko basin. The northern end extends across much of western Kansas, part of which is denoted as the Hugoton embayment (Figure 4.2-2). The Anadarko Basin is the deepest sedimentary and structural basin in the cratonic interior of the United States. The deep Anadarko basin and the Wichita-Amarillo uplift is known as the southern Oklahoma aulacogen which was also the deepest part of the Oklahoma basin (Johnson, 1988). Figure 4.3-2 shows the generalized stratigraphy of southern Oklahoma. The Woodford Shale was deposited as the sea progressed from south-southeast to northwest during a global sea-level rise. The base of the Woodford Formation has been correlated with the Taghanic onlap (Paxton et al., 2006), formed in response to the Kaskaskia transgression (Sloss, 1963). A widespread regional unconformity (period of non-deposition and erosion) defines the base of the Woodford Shale that in most places rests on the Silurian age Hunton Limestone. Paleogeographic reconstruction indicates that during late Devonian time North America (Laurentia) moved north which placed the southern midcontinent near 15° to 20° south latitude (Figure 4.3-3). Such latitudes are

associated with frequent ocean upwelling and a temperate climate, both of which aided the high biologic production and resulting TOC enrichment seen in the Woodford Shale.

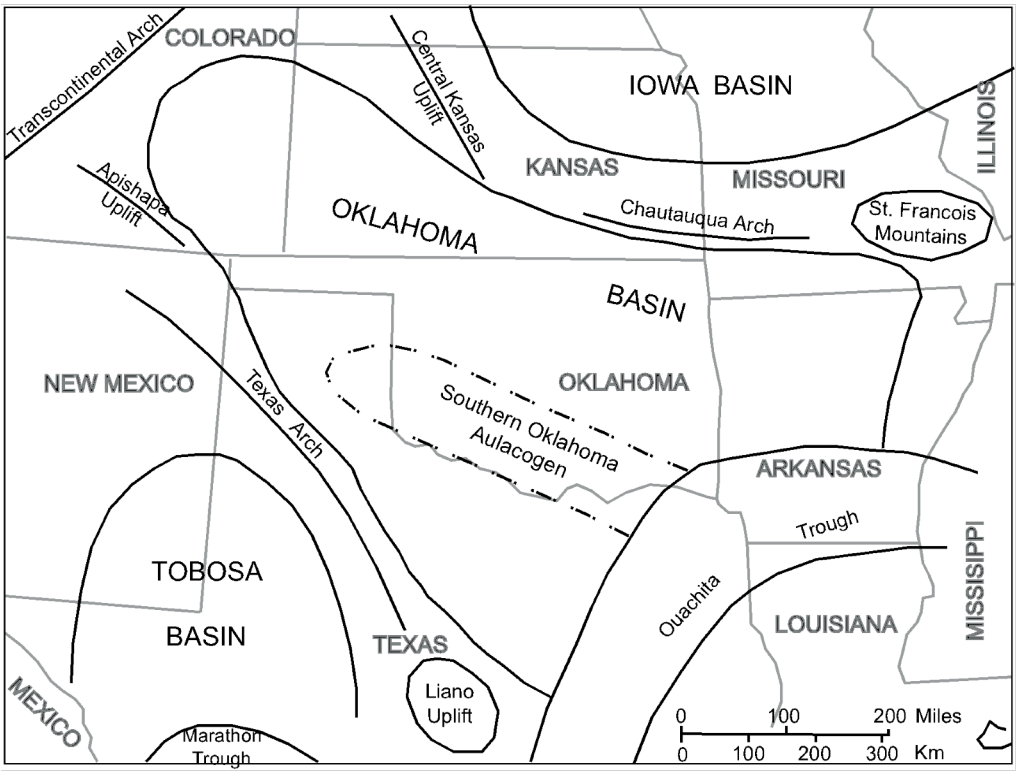

Figure 4.3-1: Approximate boundary of the Oklahoma basin and other major features in the early and middle Paleozoic time. Figure modified from Johnson,1988.

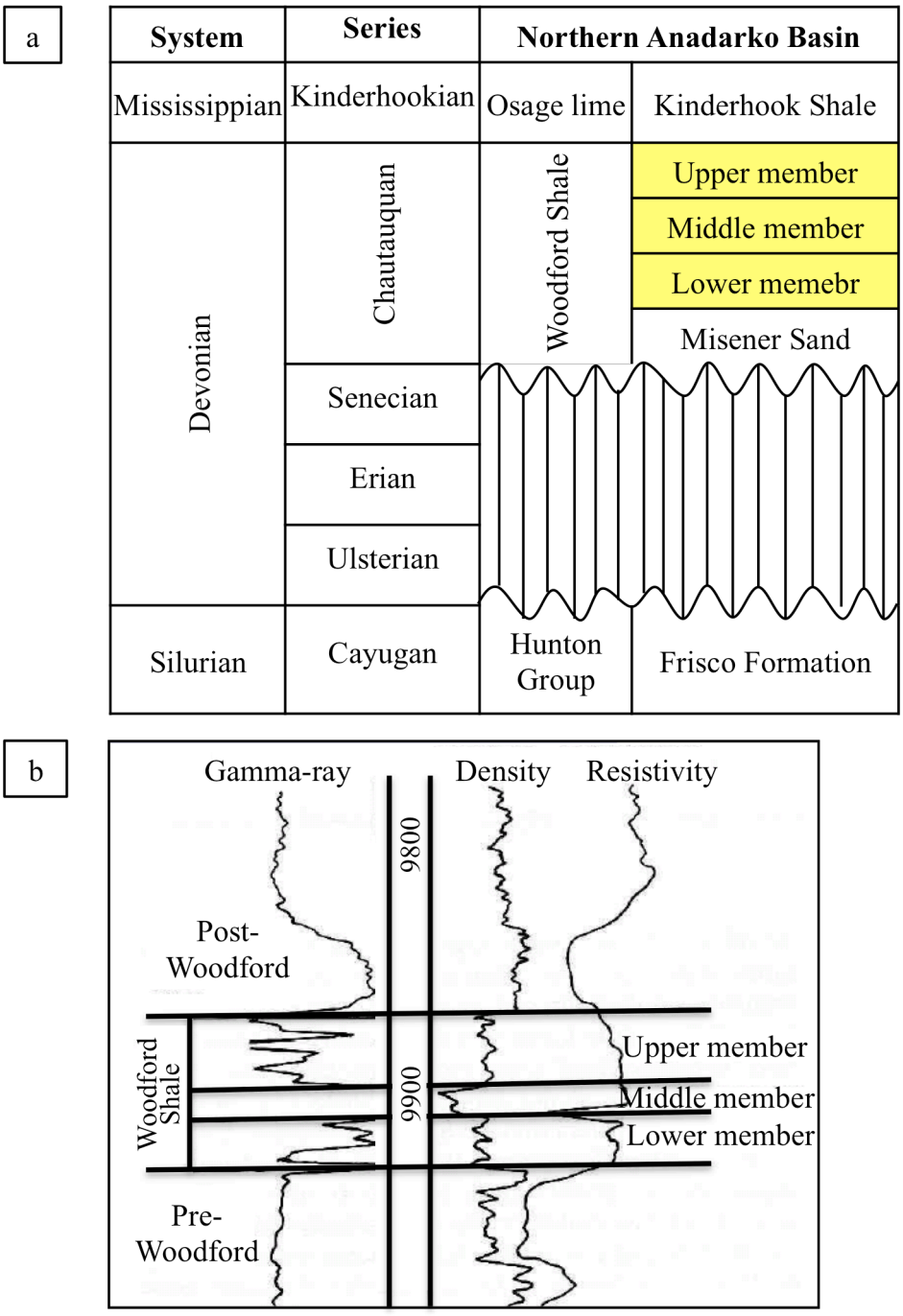

Figure 4.3-2: (a) Stratigraphy of the Woodford Shale in the Northern Anadarko Basin, (b) type logs for the Woodford Shale. The informal members are defined on the basis of palynomorph, geochemistry and log signatures. Figures are modified from Schmoker (1995) and Cardott (2008).

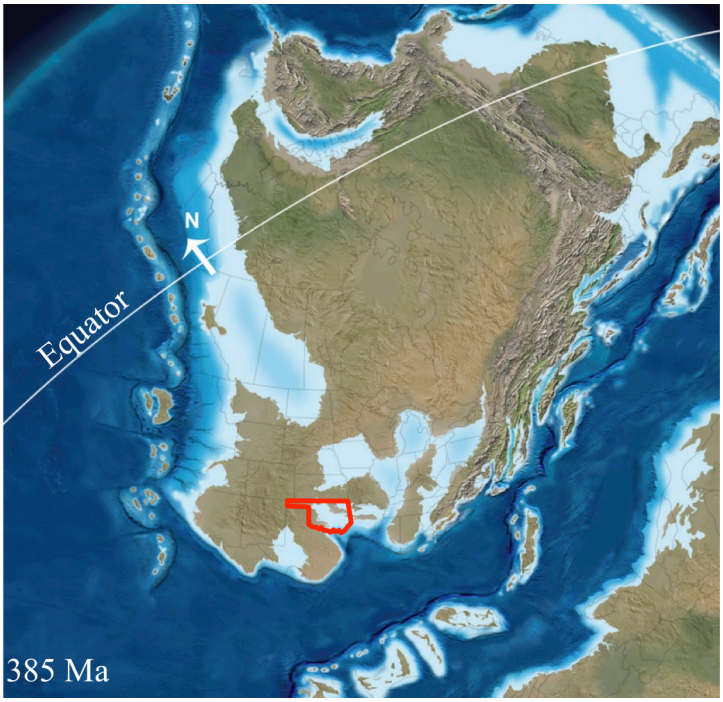

Figure 4.3-3: Paleogeography of North America at the beginning of late Devonian (Frasnian). Paleo-location of Oklahoma is marked with red line. Figure is modified from Comer, 2008a.

4.4 Available Data

Our analysis is based on detailed analyses of two subsurface cores (well 1 and well 3) from both hydrocarbon-producing and non-producing wells coupled with field data from a number of wells that will be used to understand the geologic history of the studied area. Figure 4.4-1 shows the locations of the wells used in this study. Visual core descriptions along with thin sections were analyzed for petrographic analyses. Pieces of the core were also analyzed under Scanning Electron Microscope (SEM). High-resolution sampling (roughly 2 ft sampling interval) was done for petrophysical measurements including mineralogical composition using the Fourier transform infra-red spectroscopy (FTIR) technique, porosity, Φ, using low pressure porosimetry (LPP) technique, bulk

density, ρ_b, grain density, ρ_g, mercury injection capillary pressure curve, total organic carbon content, TOC, using LECO method, and rock-eval pyrolysis. Acoustic velocities (one P- and two polarized S-wave velocities) as well as nuclear magnetic resonance (NMR) measurements were made on 82 horizontal plugs. The TOC and rock-eval measurements were carried out at the Weatherford laboratories while bulk of the measurements were made at the University of Oklahoma's Integrated Core Characterization Center (IC^3). Core gamma ray measurements were made by Terratek and provided by the operator. Core measurements were augmented by gamma ray, sonic velocities (V_P, V_S), ECS, ρ_b, PEF, resistivity well-logs.

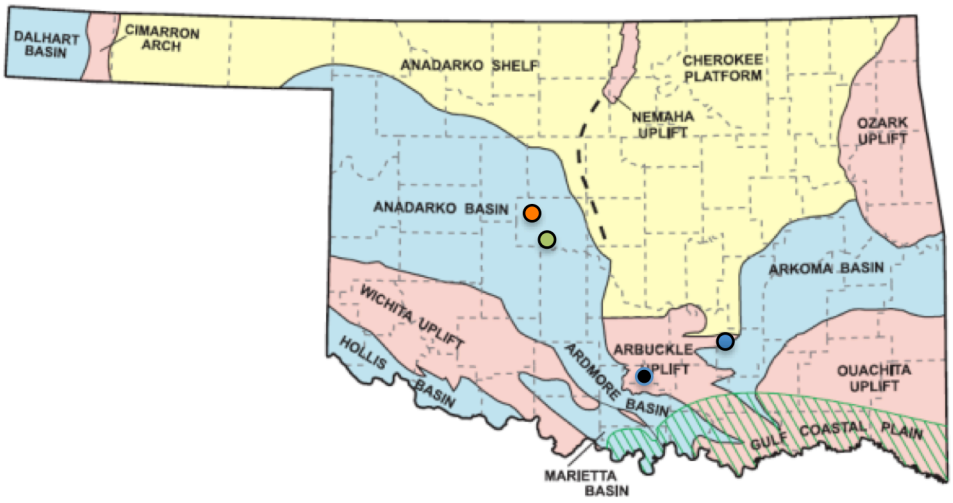

Figure 4.4-1: Major geologic provinces of Oklahoma shown by different colors (modified from Johnson et al., 1988) with dots showing the well locations used in this study. Red, and green dots indicate two cored wells, well 1 and well 3 respectively. Black dot indicates Amis 1-3 well, and blue dot indicates Wyche well; both located near the Arbuckle uplift.

4.5 Lithofacies and petrographic characteristics

Overall, the Woodford Shale core appears from dark brown to black in color. I have identified 6 lithofacies based on visual description (Figure 4.5-1) of two subsurface cores: (1) black shale, (2) cherty, shiny black shale, (3) greyish shale, (4) yellowish-black shale, (5) highly organic-rich shale and (6) yellowish-grey shale. The black shale and shiny-black shale facies constituted about 80% of the Woodford interval. Further analyses of different lithofacies were then performed through microscopic and sub-microscopic observations of these rocks. Thin sections of the black shales not only provide a means for petrographic analyses but also a means to visualize megascopic sedimentary features which are otherwise impossible to recognize due to dark color of the studied rock. These megascopic features can then be correlated to microscopic and submicroscopic features imaged using SEM analysis.

The framework elements of these rocks are grouped into four primary components: (i) clay matrix, (ii) silty particles, (iii) organic matter, and (iv) fractures. The silty material is composed of flattened Tasmanities cysts, mineralized fossils (primarily Tasmanities cysts, along with some benthic foraminifera), detrital quartz and dolomite particles, and pyrite. Petrographic inspection of the dominant black shale facies subdivides this facies into two: fossil-rich mudstones and laminated mudstones (Figure 4.5-2). While both types of black shale are present in the two studied wells, well 3 contains much smaller amount of both fossil and detrital silt-materials and greater quantity of clay. Measured mineralogy data discussed in Chapter 1 of this dissertation indicates that average clay content of well 1 is 40 wt.% and well 3 is 60 wt.%. Petrographic observations also reveal that Tasmanities are present throughout the

Woodford interval and served as the primary source of organic matter in the study area. Tasmanities were mineralized to different extent depending on the availability of silica with dissolution of radiolarians serving as the primary source of silica (Schieber, 1996).

In some intervals the lamination of the black shale facies is completely destroyed by bioturbation activity. Bioturbated intervals could easily be identified through mottled fabric, and destroyed lamination (Figure 4.5-3a, and b) distinguishable under petrographic microscope. Identification of bioturbated intervals on hand specimen is possible through careful inspection of water-wet surface (Figure 4.5-3c, and d). The presence of pyrite streaks also indicates bacterial activity at the sediment-water interface that might have been flattened due to compaction. Pyrite is also present as nodules and pyritized microfossils as well as in the form of framboids. The cherty facies (the second dominant lithology) is present at many scales, ranging from lamina to beds to layer (Figure 4.5-5). The irregular boundary of this lithofacies at any scale indicates that deposition of this lithofacies was associated with current action (Figure 4.5-4). Other sedimentary structures in the rocks include: fining-upward sequences (Figure 4.5-4), slump structures (Figure 4.5-6), and fractures.

The Woodford Shale is affected by both natural and drilling-induced fractures (Figure 4.5-7) with natural fractures identified by the presence of authigenic minerals. Natural fractures are present within the brittle cherty facies while no natural fractures could be distinguished within the ductile black shale facies. Natural fractures vary in orientation (vertical to near horizontal), filling material (such as dolomite, silica, and pyrite) and also filling property (completely-filled versus partially-filled). Deformed nature of both fractures (Figure 4.5-7a) and adjacent host layers indicate these fractures

were developed prior to complete lithification of the unconsolidated sediments. Comer (2008b) proposes these dolomite-filled fractures to be possible hydrocarbon primary migration pathways that probably were generated during hydrocarbon generation. Figure 4.5-1 is a representative image showing fracture intensity, which made it impossible to collect core plugs over highly fractured/broken areas. Mineralogy data (Figure 4.5-8) indicates that well 3 has higher clay content and is less fractured compared to well 1, which has a lesser amount of clay and is broken into pieces at many intervals (Figure 4.5-1). Mineralogy data (Figure 4.5-8) also indicates fracture intensity (Figure 4.5-1) increases in areas with higher amount of brittle minerals such as quartz and carbonates. Within well 1, the presence of dolomite-filled fractures subdivide the lower Woodford (LW) interval into a lower, highly-fractured interval and an upper interval with lower fracture intensity. The lower interval is badly fractured due to dense silica-filled fractures, which may have been enhanced by the drilling activity. There were fewer natural and induced fractures present in the upper part of the LW, which contains higher clay content compared to the lower part. Most of the middle Woodford (MW) is characterized by medium fracture intensity. At the base of MW very few fractures were present followed by a 10 ft thick missing interval. Medium fracture intensity is observed in the interval X0570ft-X0605ft, followed by high fracture intensity in the upper Woodford. Only part of the upper Woodford (UW) was present in well 1. The UW was highly fractured (both natural and drilling induced) for much of the interval such that core was not recovered in several intervals. The black shale facies present near the very top had very few fractures.

No pore spaces are visible through petrographic microscopic observation owing to the nanometer-scale characteristic pore size, as discussed in chapter 2 of this thesis. SEM

imaging has revealed organic pores as the most common pore types in the studied shale (Figure 4.5-9).

The rich diversity of sedimentary features illuminated through these multi-scale analyses indicates a range of geologic processes during Woodford deposition. All of these petrographic and lithologic characteristics observed at multiple scales are used to investigate the depositional history and stratigraphic changes during the Woodford Shale deposition.

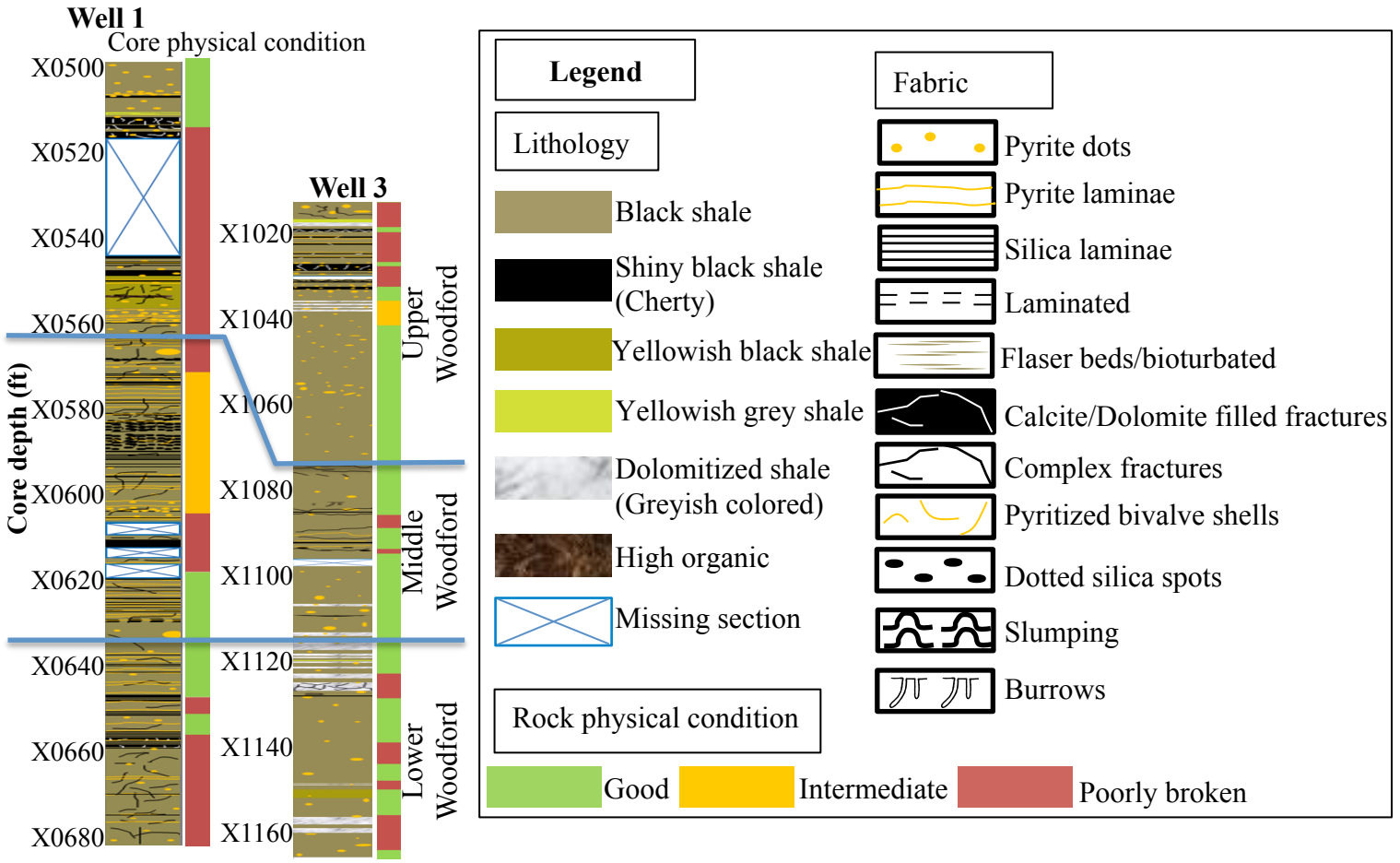

Figure 4.5-1: Schematic core description of wells 1 and 3.

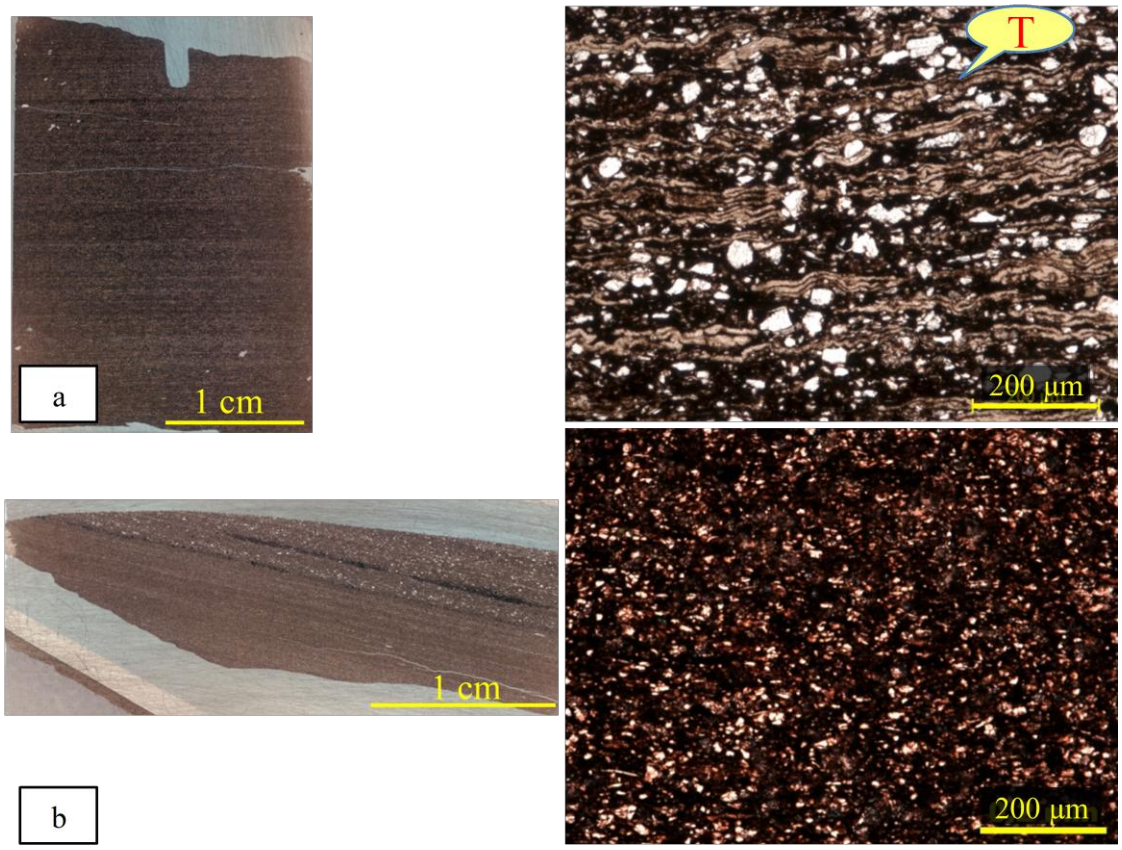

Figure 4.5-2: Two types of black shale: (a) organic rich shale, and (b) laminated shale. High-resolution scan of the thin section is shown on the left and photomicrograph under plane polarized light is shown on right. Deformed Tasmanities spores (T) can be seen on Figure a.

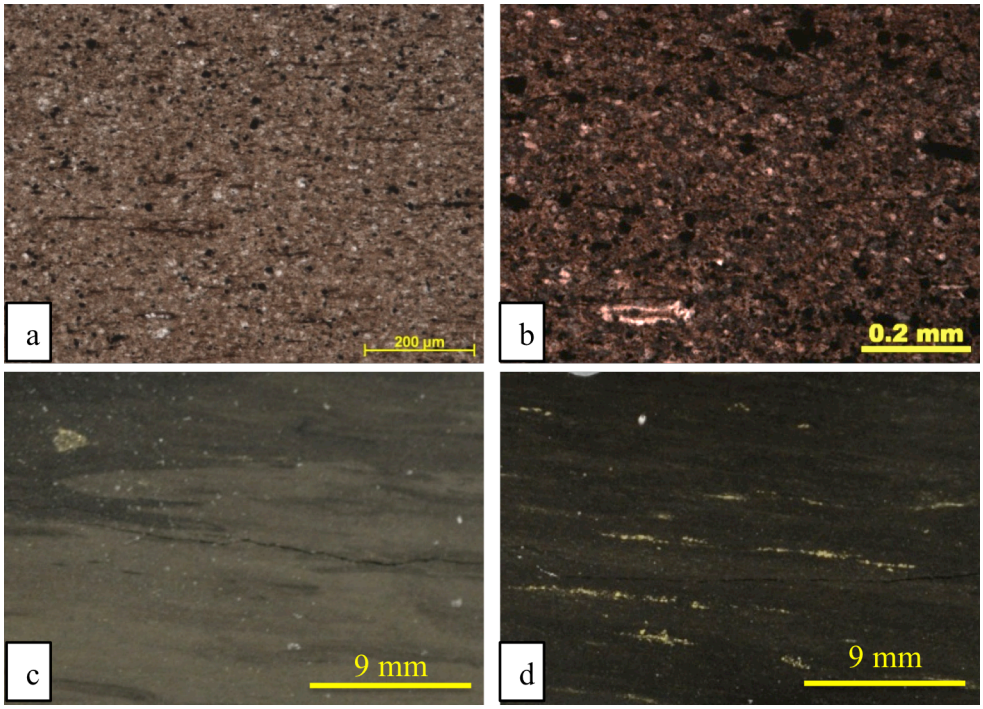

Figure 4.5-3: Photomicrograph under plane polarized light showing mottled fabric of highly bioturbated samples from (a) well 1 (a) and (b) well 3. (c), and (d) Water-wet surface of core showing bioturbated rocks in hand specimen, further enhanced by digitally increasing the contrast of the picture.

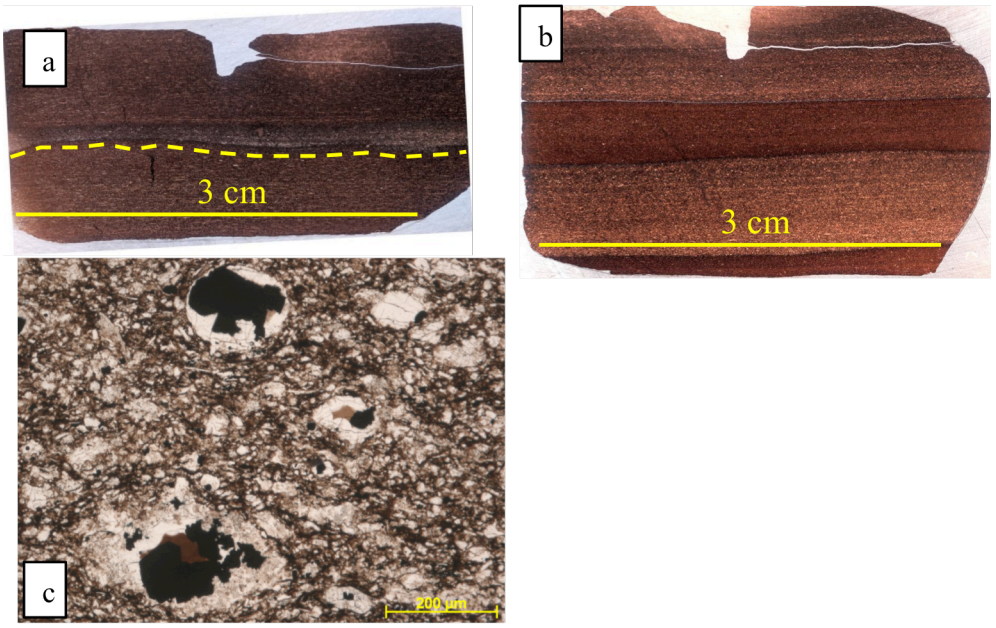

Figure 4.5-5: (a, b) High-resolution scan of thin sections showing different thicknesses of the cherty lithofacies. The millimeter-thick cherty layer is highlighted by the yellow dashed line on Figure a. (c) Photomicrograph under plane polarized light showing the cherty facies.

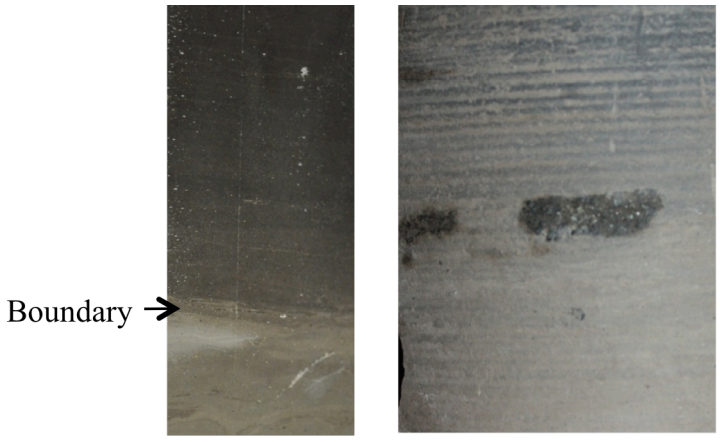

Figure 4.5-4: Picture of the water-wet hand specimen showing boundary between the underlying bioturbadated mudstone and overlying black shale. A fining upward sequence can be observed just above the boundary. Presence of pyrite-rich clay clasts, which appear as dark color in the figure on right at this boundary possibly indicative of transgressive lag deposit.

Figure 4.5-6: Slump visible at the high resolution scanned image of a thin section.

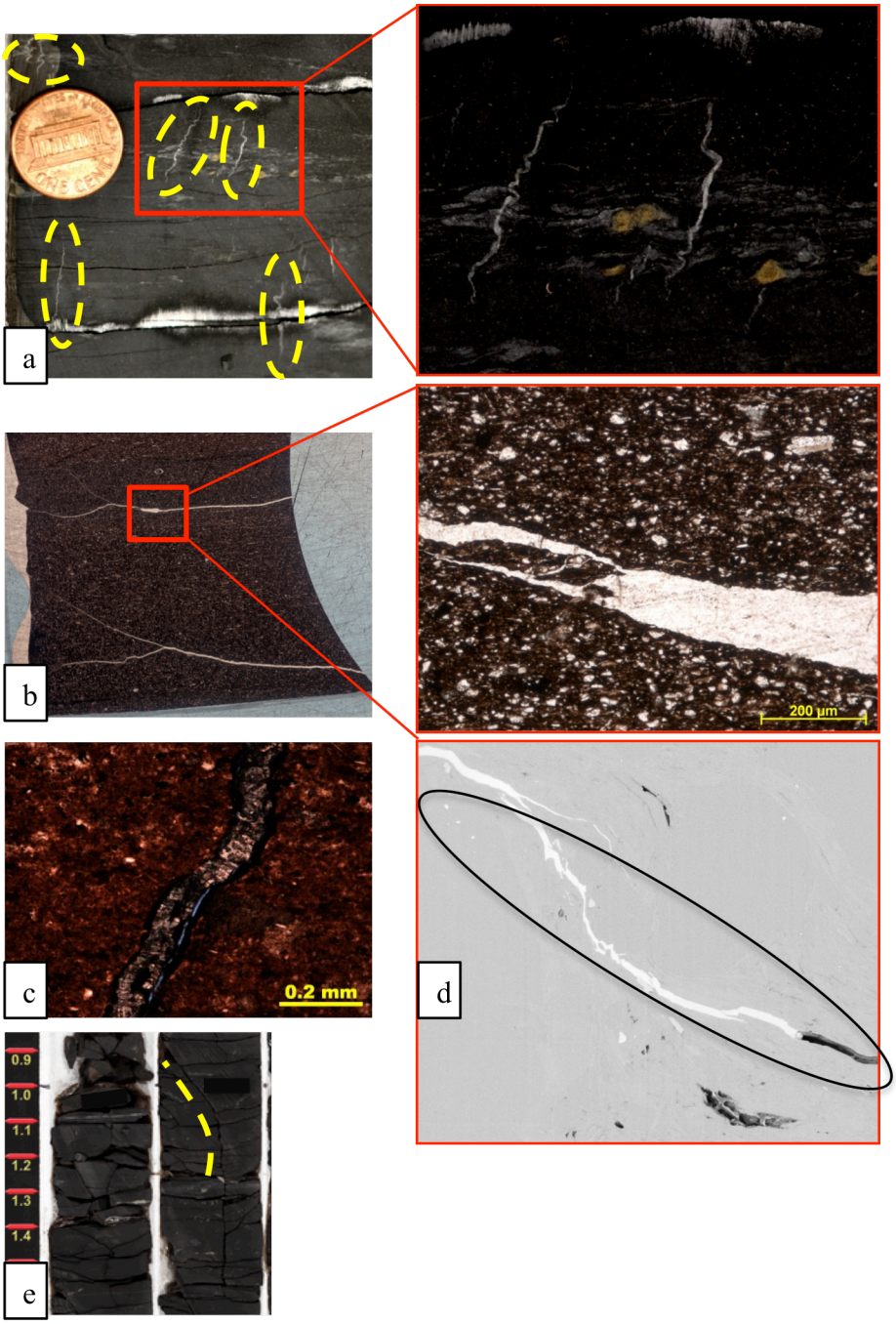

Figure 4.5-7: (a) Photo of a piece of core showing near vertically oriented dolomite-filled natural fractures. (b) Images of a thin section showing low-angle dolomite-filled natural fractures. (c) Thin section showing partially filled natural fracture. (d) SEM image showing a pyrite-filled natural fracture highlighted by ellipse. (e) Photo of a core; yellow line indicates a drilling induced natural fracture.

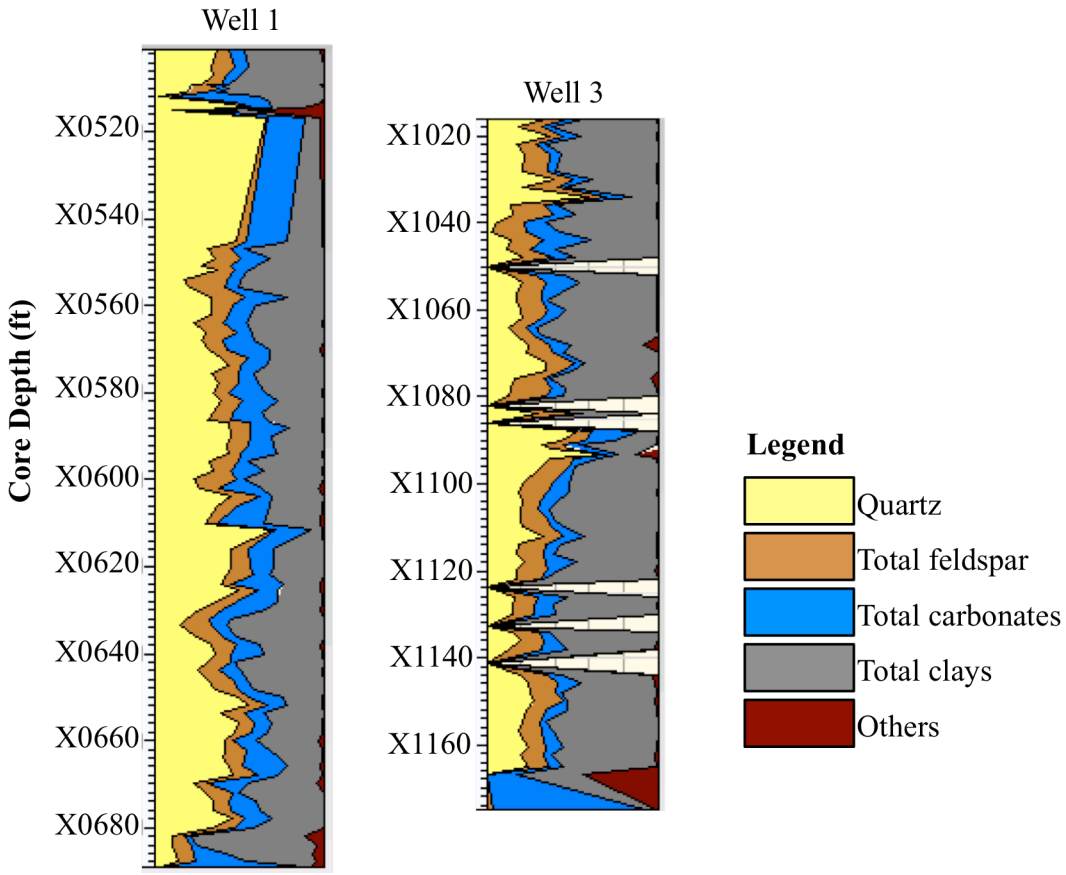

Figure 4.5-8: Mineralogic variations with depth for wells 1, and 3 showing that well 3 has higher clay content compared to well 1.

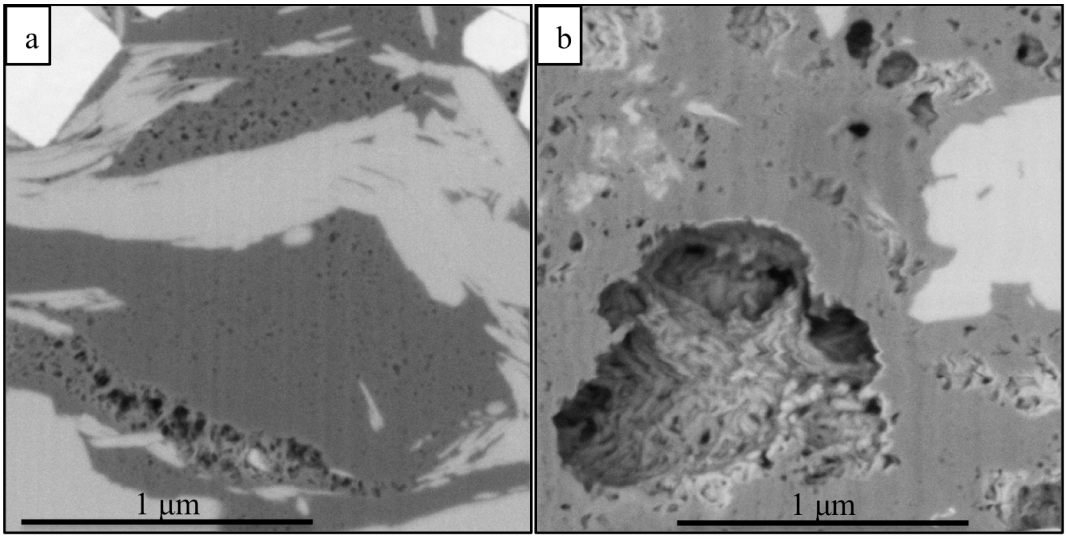

Figure 4.5-9: FIB-SEM images of samples from (a) well 1, and (b) well 3 showing organic pores which are the most common pore types in the studied cores. Dark grey areas indicate organic matter, while still darker areas within the organic matter indicate pores within the organic matter.

4.6 Depositional history

The overall silty nature, random orientation of clay and silt grains, disrupted shale laminae, storm deposits identified through thin alternating layers of clay and silt lamina suggesting episodic sedimentation indicate that the Woodford deposition occurred above the storm-weather wave-base, probably within a shallow-shelf depositional environment (Figure 4.5-2). Petrographic analyses and petrophysical properties coupled with knowledge about the paleogeography of North America (Comer, 2008a) indicate that the Woodford Shale was deposited in an epeiric sea during a eustatic sea-level rise punctuated by a number of higher order depositional cycles. An arid paleoclimate, indicated by the south 15° latitudinal position of North America, limited the amount of detrital supply to the basin, which resulted in high clay concentration in both near shore

and far offshore areas (Comer, 2008a). The slow rate of deposition (where 50 Ma is represented by a 200 ft thick rock record) results in high frequency variations in the lithostratigraphic column where thin intervals of rocks represent individual depositional cycles. The fine-grain nature and overall dark color reduces the ability to visually identify all the depositional cycles. Change in mineralogy seems to be one of the primary parameters responding to geologic processes and sea-level changes. Overall, the mineralogical constituents are: 10%-50% quartz except for a few samples from cherty intervals where the quartz component approaches 70%, 0%-20% feldspar, 3%-32% total carbonate, 20%-60% total clays and 0%-14% other minerals which include anhydrite, apatite and pyrite (Figure 4.5-8 and Figure 4.6-1). Illite is the dominant clay mineral in both the wells, which correlates with the high thermal maturity ($450°C<T_{max}<500°C$) of the studied rocks. However, the complex nature of lithostratigraphic changes indicates that no one parameter can adequately be used to track the depositional history. Among the petrophysical systematics identified in this study, an increase in bulk density correlates with an increase in clay content, specifically illite and a decrease in quartz content. Changes in bulk density also correlate to other changes observed through microscopic and sub-microscopic observations of samples collected at frequent depth intervals providing a means of identifying 14 depositional cycles within the Woodford interval. The lower Woodford has six (named as LW1 through LW6 from base to top), middle Woodford has four (named as MW1 through MW4 from base to top) and the upper Woodford has four (named as UW1 through UW4 from base to top) cycles in well 1. Well 3 has a comparatively thinner Woodford interval with the individual Woodford members containing five, four, and four depositional cycles from the base to the top

respectively. The LW, MW and UW measure 58.4 ft, 75.8 ft, and 59.2 ft respectively in well 1 and 45 ft, 38 ft, and 57 ft respectively in well 3 (Figure 4.6-2). Photomicrographs indicate increasing bioturbation, and the presence of cherty facies near the top of most of these depositional cycles. An increase in gamma-ray response at the boundaries indicate that these depositional cycles may correspond to parasequences within the study area. The three informal members (lower, middle and upper member) of the Woodford Shale have been identified based on the wireline log signatures and correlation to other wells in the field.

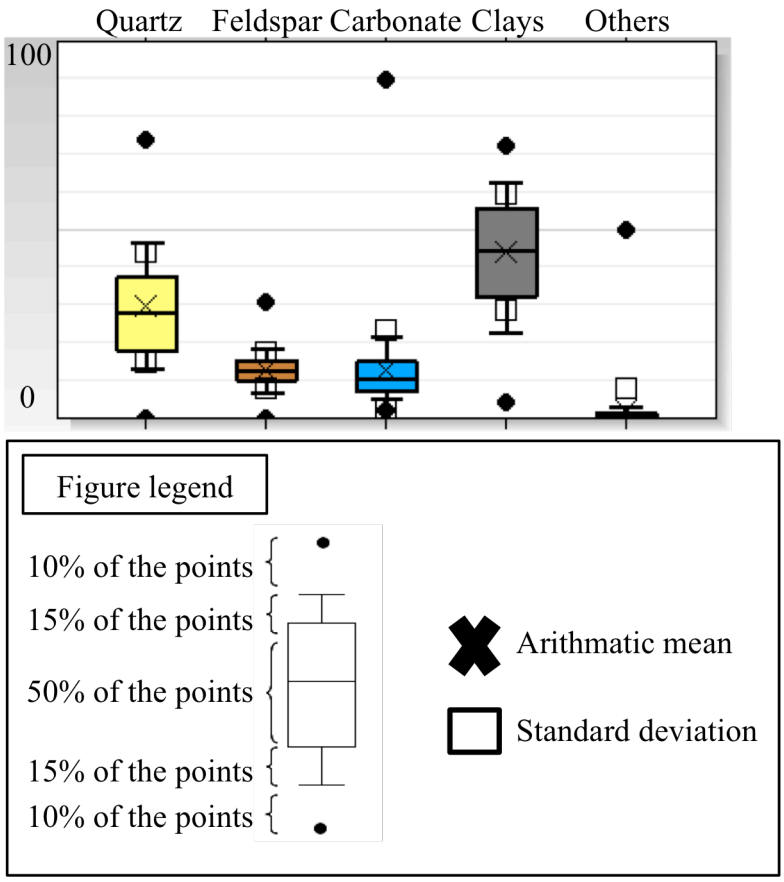

Figure 4.6-1: Box-and-whisker plots showing distributions of 5 groups of minerals mentioned in Figure 4.5-8.

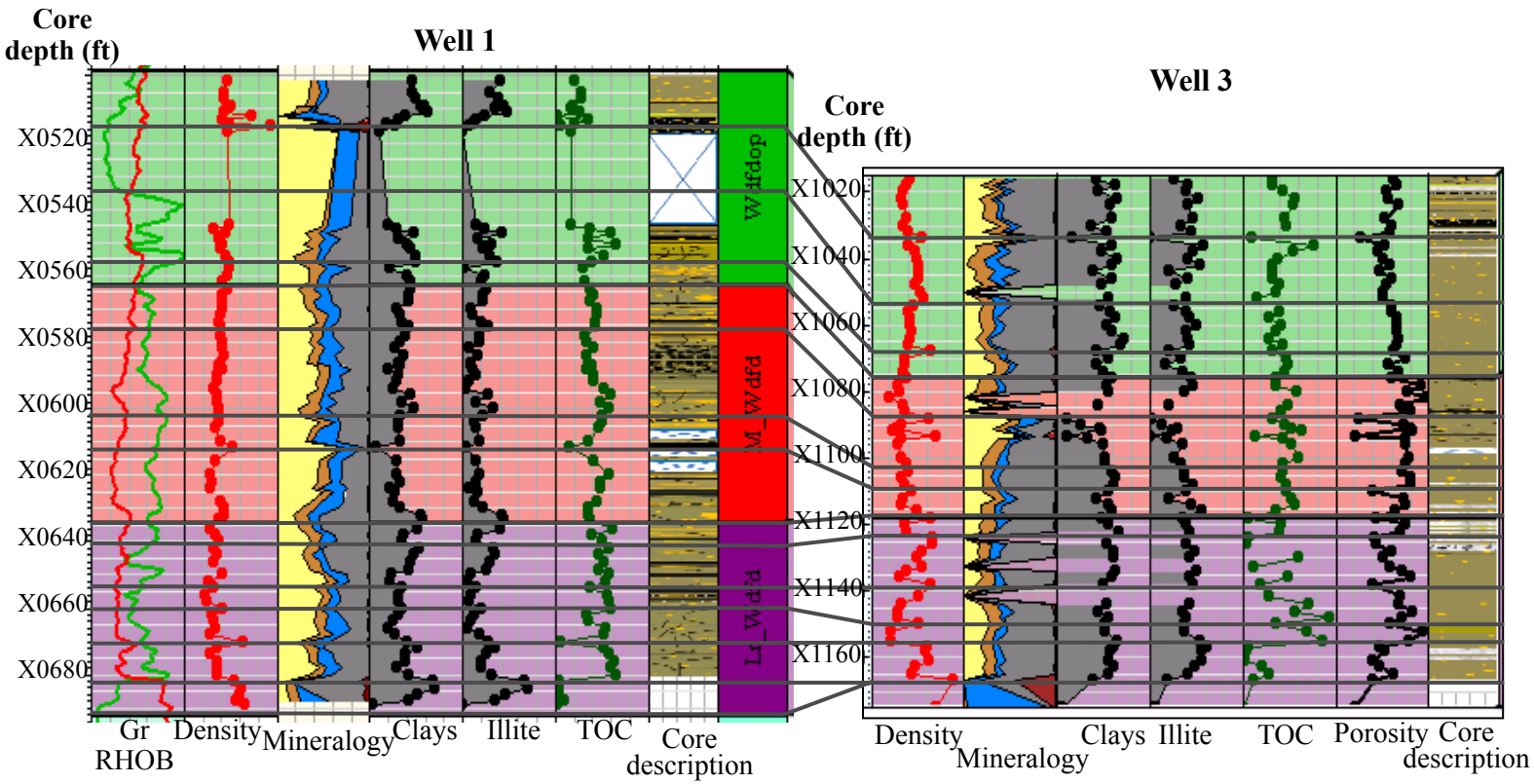

Figure 4.6-2: Depositional cycles for well 1 and well 3.

Lower Woodford

The base of the Woodford is defined by an unconformity and the sharp change from limestone to black shale (Figure 4.6-3). Following is a brief description of each depositional cycle. The depositional cycles are denoted (from bottom to top) as LW1-LW6.

LW1: X0688.4 ft to X0680 ft in well 1. Total thickness: 8.4 ft. This cycle is present in well 1 only. This is a unique cycle at the base of the Woodford, containing a carbonate turbidite at the top of this cycle. A sudden jump in quartz content, TOC, and porosity and a sudden drop in clay content define the upper boundary of this cycle. Randomly oriented, partially silica-filled natural fractures are common in this cycle. A few drilling induced fractures are also present.

LW2: X0680 ft to X0670 ft in well 1, X1167 ft to X1156 ft in well 3. The upper boundary of this cycle is marked by an increase in bulk density and clay content. Photomicrographs suggest an increase in bioturbation (Figure 4.5-3a) at the top of this depositional cycle.

LW3: X0670 ft to X0660 ft in well 1, X1156 ft to X1150 ft in well 3. The upper boundary of this cycle is marked by an increase in bulk density and clay content. Like the cycle below, photomicrographs suggest an increase in bioturbation at the top of this depositional cycle.

LW4: X0660 ft to X0650 ft in well 1, X1150 ft to X1138 ft in well 3. The upper boundary of this cycle is marked by an increase in bulk density and clay content. Overall, high TOC and porosity values characterize this cycle in well 1. Both TOC and porosity decreases upward in well 3.

LW5: X0650 ft to X0641 ft in well 1, X1138 ft to X1124 ft in well 3. The upper boundary of this cycle is marked by an increase in bulk density and clay content. Again photomicrographs suggest an increase in bioturbation at the top of this depositional cycle.

LW6: X0641 ft to X0633 ft in well 1, X1124 ft to X1117 ft in well 3. The upper boundary of this cycle is marked by an increase in bulk density and clay content. Again photomicrographs suggest an increase in bioturbation at the top of this depositional cycle. The upper boundary of this cycle matches with the boundary between the lower and the middle Woodford member and hence is traceable across the basin.

Middle Woodford

The depositional cycles are denoted (from bottom to top) as MW1-MW4.

MW1: X0633 ft to X0618 ft in well 1, X1117 ft to X1110 ft in well 3. The upper boundary of this cycle is marked by an increase in bulk density and clay content. Again photomicrographs suggest an increase in bioturbation at the top of this depositional cycle.

MW2: X0618 ft to X0602 ft in well 1, X1110 ft to X1115 ft in well 3.

MW3: X0602 ft to X0578 ft in well 1, X1115 ft to X1091 ft in well 3. Photomicrographs from well 3 indicate a period of non-deposition or formation of hard ground (Figure 4.6-4) near the top of this cycle.

MW4: X0578 ft to X0562 ft in well 1, X1091 ft to X1078 ft in well 3. The upper boundary of this cycle matches the boundary between the middle and the upper Woodford and hence, is traceable throughout the basin.

Upper Woodford

The core was not recovered for part of the upper Woodford in well 1. Hence, the wireline bulk density is used to determine the depositional cycles in the upper Woodford, which are denoted UW1-UW4.

UW1: X0562 ft to X0555 ft in well 1, X1078 ft to X1068 ft in well 3. Figure 4.6-5 shows high-energy current related deposit present just above the top of this boundary. The upper boundary of this cycle matches with the highest gamma ray count within the Woodford interval, indicating a flooding surface and the rock indicates a transgressive lag (Figure 4.6-5).

UW2: X0555 ft to X0526 ft in well 1, X1068 ft to X1051 ft in well 3.

UW3: X0526 ft to X0515 ft in well 1, X1051 ft to X1034 ft in well 3.

UW4: X0515 ft to top of the Woodford in well 1, X1034 ft to top of the Woodford in well 3. The base of this cycle indicates a regional slumping event (Figure 4.5-6) followed by shallowing of the water column. Characteristic features of this unit include: bioturbated rock (Figure 4.6-6), fossil assemblages dominated by benthic organisms (for example, benthic foraminifera) (Figure 4.6-7).

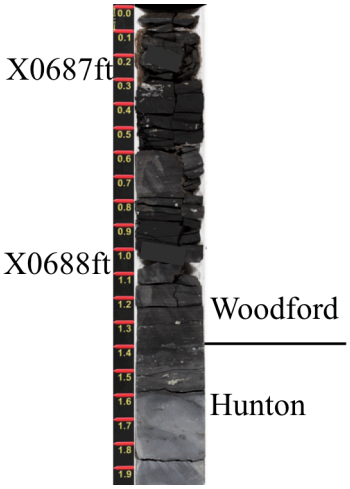

Figure 4.6-3: Core from well 1, showing the erosional unconformity between the Hunton Limestone and the overlying Woodford Shale.

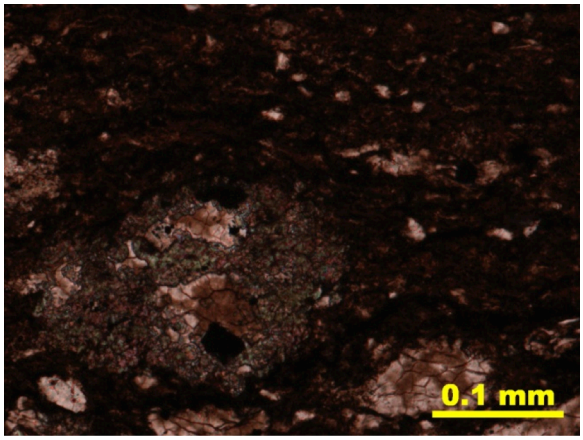

Figure 4.6-4: Photomicroph under plane polarized light showing hard ground present at X1091 ft in well 3.

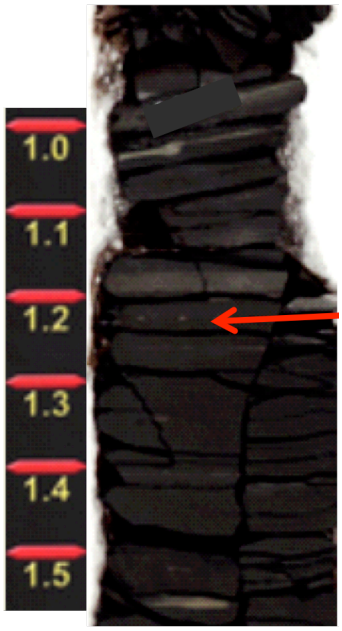

Figure 4.6-5: A section of core showing the contact at X0555 ft in well 1(marked by red arrow).

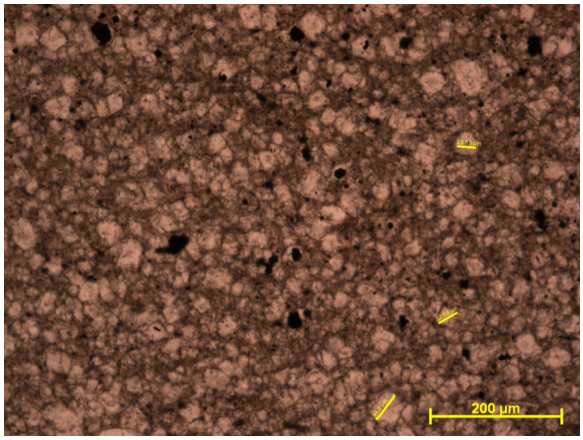

Figure 4.6-6: Photomicrograph of a sample from well 1 showing highly bioturbated, dolomitic layer (at X0511.8ft) under plane polarized light. Original laminations are completely disrupted by the bioturbation.

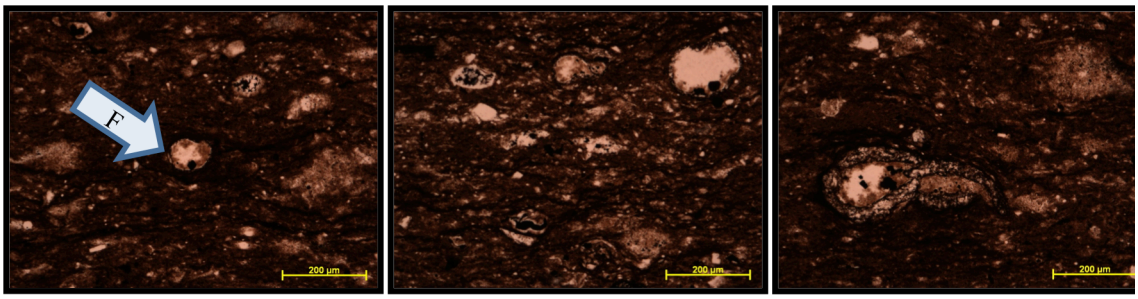

Figure 4.6-7: Photomicrographs of samples from well 1 indicate completely different fossil assemblage of the upper Woodford at X0513ft compared to the rest of the Woodford interval containing primarily algal laminae, Tasmanities spores etc. Agglutinated foraminifer is marked on the left figure with white arrow (F).

4.7 Correlation to the regional changes

Gamma ray (GR) logs is the most common tool used for the stratigraphic correlation across long distances. However, gamma-ray models by Paxton et al. (2006) suggest that high radioactivity in shale reservoirs has two causes: high TOC, and slow sedimentation rates giving rise to an increase in uranium associated clay minerals. Hence, GR correlation can be misleading except for very high peaks, which are likely to be related with large basin-wide events and are expected to be present basin wide. The Woodford Shale is characterized by an overall high gamma ray (>200 API) and only a few very high GR peaks (>400 API) correlatable across the basin, most likely indicate global events.

Johnson et al. (1985) proposed a eustatic sea-level curve for the late Devonian-early Mississippian time. Sandberg et al. (2002) later refined these curves. Figure 4.7-1 contains the descriptions of 18 late Devonian events, as described by Sandberg et al. (2002). Paxton et al. (2006) correlated the gamma ray from the Amis 1-3 using Johnson

et al.'s (1985) eustatic sea level curve. Correlation between well 1 to the Amis 1-3 well have been used to identify sea-level changes in the study area. Figure 4.4-1 shows the locations of the wells used for regional correlation. Paxton et al. (2006) correlated the base of the Woodford Shale with the Tahini onlap (Sloss, 1963). Both correlations to the eustatic sea-level and petrographic analyses of the cored wells indicate that the lower Woodford (LW) was deposited as an earlier part of transgression, the middle Woodford (MW) was deposited when the transgression reached the maximum and the upper Woodford (UW) was deposited as the sea level began to fall. Lambert (1993) also concluded (based on regional work) that the lower, middle, and upper shale members of the Woodford and Chattanooga represent the transgressive and early and late highstand systems tracts of the sequence. The highest gamma ray peak near the MW-UW boundary probably matches the maximum flooding surface (MFS) and is the highest gamma ray peak within the Woodford interval in all the studied wells (well 1, Amis 1-3 and Wyche-1) (Figure 4.7-2). The slumping event in the upper Woodford (UW4) is correlated with the period of collapse of shelf margin at event 11 in the eustatic sea-level curve. The high TOC content of UW4 matches the post-biotic organic bloom reported at the event 12 on the eustatic sea-level curve.

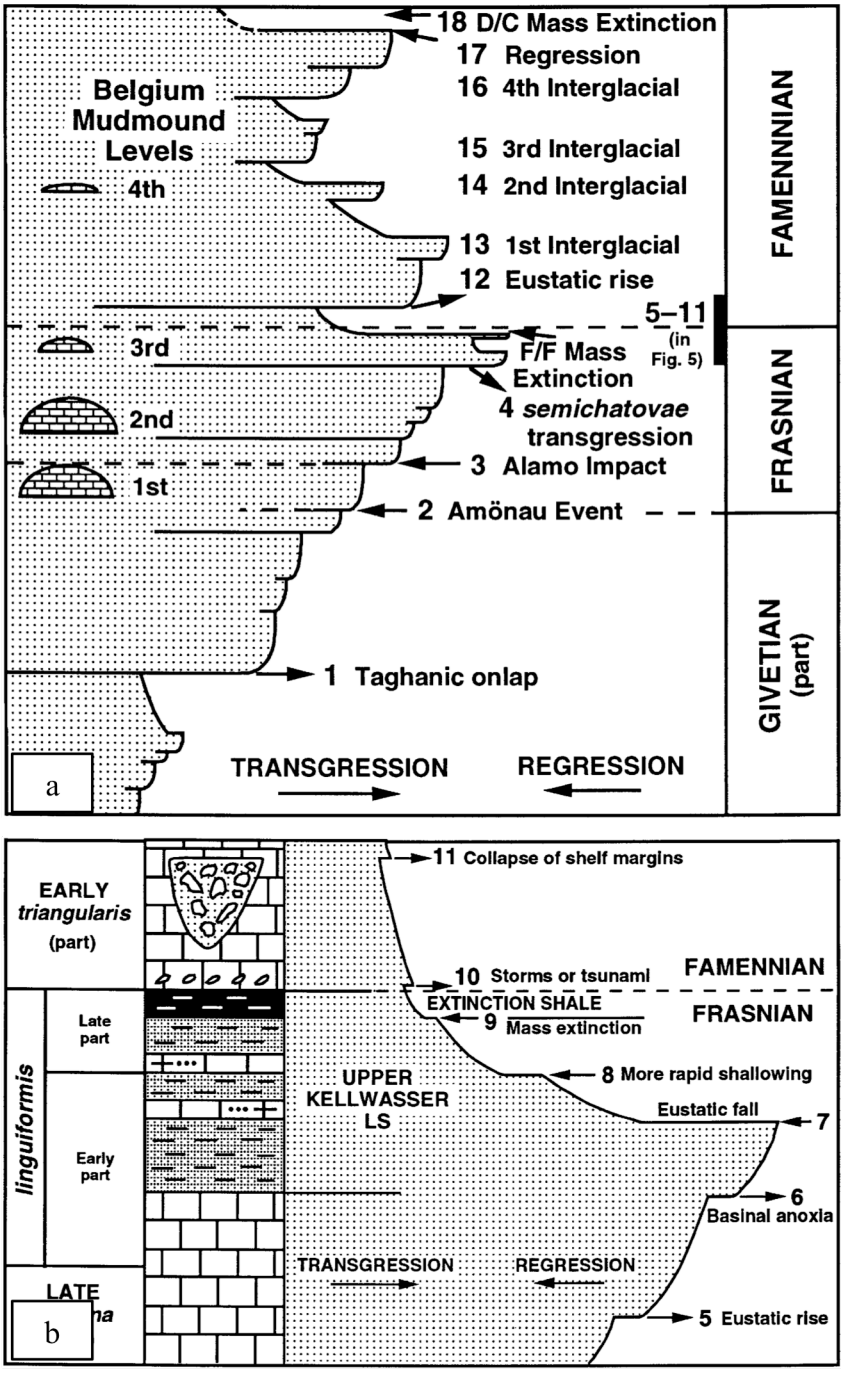

Figure 4.7-1: Eustatic sea-level curve during late Devonian time (stages include Givetian, Frasnian, and Famennian) and associated events proposed by Sandberg et al., 2002. (a) Eustatic sea-level curve showing events 1 through 18. (b) Eustatic sea-level curve showing high frequency events 5 through 11 shown a one line in Figure a. (c) Description of events 1 through 18.

No. of events	c Event Descriptions
18	Late Famennian mass extinction within eustatic fall; loss of many Devonian species including Lazarus fauna
17	Start of major eustatic fall at climax of Southern Hemisphere glaciation; biotic decline begins
16	Eustatic rise at start of 4th interglacial episode; Etroeungt Lazarus fauna suddenly appears in Northern Hemisphere
15	Eustatic rise at start of 3rd interglacial episode; annulata black basinal shales deposited in Germany
14	Eustatic rise at start of 2nd interglacial episode; Baelen mudmound formed in Belgium
13	Eustatic rise at start of 1st interglacial episode; Cheiloceras dark shales deposited
12	Eustatic rise, producing initial post-extinction biotic radiation
11	Carbonate-platform margins collapse due to glacioeustatic lowering of seas; widespread coarse tsunamite breccias result
10	Storms and (or) tsunami scour or remove Frasnian-Famennian boundary beds in France, Germany, and Nevada
9	Late Frasnian mass extinction within eustatic fall; widespread layer of abiotic extinction shale deposited; start of Southern Hemisphere glaciation
8	Rapidly increased shallowing; storm deposits; stepwise extinction of some deep-water species as shallow-water species move into deeper water; spore floras change
7	Eustatic fall; start of global cooling; reduction in number and diversity of deep-water faunas
6	Continued eustatic rise; stratification of water column, resulting in widespread basinal anoxia; start of rapid evolution of deep-water entomozoan ostracods
5	Eustatic rise producing dysoxia in deep basins; start of events leading to mass extinction
4	Major semichatovae transgression producing biotic changes and stress
3	Alamo Impact in Nevada, coinciding with eustatic rise and demise of 1st level of Belgian mudmounds
2	Amo¨nau Event, coinciding with onset of impact-induced(?) volcanic activity in central Germany and with eustatic rise at start of Frasnian
1	Taghanic onlap at start of plate-tectonic movements in Northern Hemisphere; end of faunal provincialism

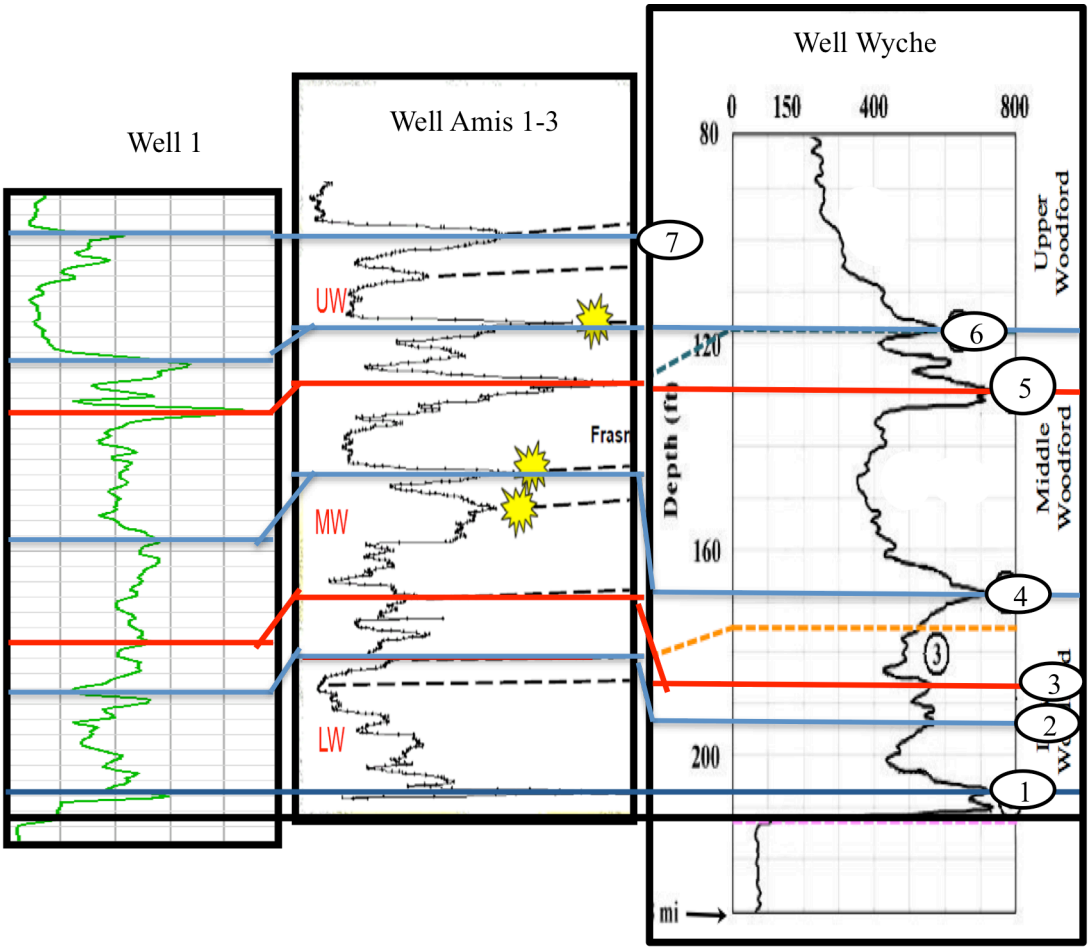

Figure 4.7-2: Gamma-ray correlations. Blue dashed lines are correlation lines indicated by circled numbers 1-7. Red correlation lines are the boundaries between lower-middle Woodford and middle-upper Woodford respectively. The boundary between LW and MW was originally placed at correlation point 2, in the Amis 1-3 well, in Paxton et al.'s (2006) original paper.

4.8 Depositional model

Seismic data indicates that the Woodford deposition took place on a very irregular surface (Chapter 3 of this dissertation) of the Hunton Limestone. Topographic lows on the Hunton Limestone were inundated earlier and topographic highs inundated later. The overall thinner Woodford interval with a missing LW1 depositional cycle in Well 3 indicates that the Woodford deposition started later in well 3 than in well 1, and was located topographically higher on the basin floor. Well 1 contains both the black shale lithofacies and the brittle cherty lithofacies, which was associated with high-energy flow. Such high-energy flow might have resulted from a number of events, including storm-related currents and/or debris flows, both of which would have followed depressions on the basin floor. The lack of significant cherty facies in well 3 also supports the location of the well 3 on a local basin floor high. Seismic attribute analysis indicates that the depressions on the basin floor are characterized by high curvature values, collapse features (low similarity values), all potentially indicating zones of natural fracture concentrations. The core from well 3 indicates frequent bioturbated interval indicating significantly more benthic organic activities compared to well 1, most probably owing to the shallower water depth at well 3 compared to well 1. Figure 4.8-1 proposes a depositional model for the Woodford shale that integrates these hypotheses.

This model shows that the organic matter in the Woodford Shale is sourced from highly mobile planktonic organisms (for example, Tasmanities, Radiolarian etc.). For this reason, intermediate basin locations, typical areas of upwelling are likely to have high population of such organic matter and are potential areas for greater organic and therefore hydrocarbon accumulation. This model predicts the upper Woodford member to be

organic rich in deeper parts of the basin. Eustatic sea-level curve indicates a major sea-level drop at this stage of the Woodford deposition, making the deeper part of the basin likely areas for upwelling, nutrient supply and planktonic organic matter concentrations.

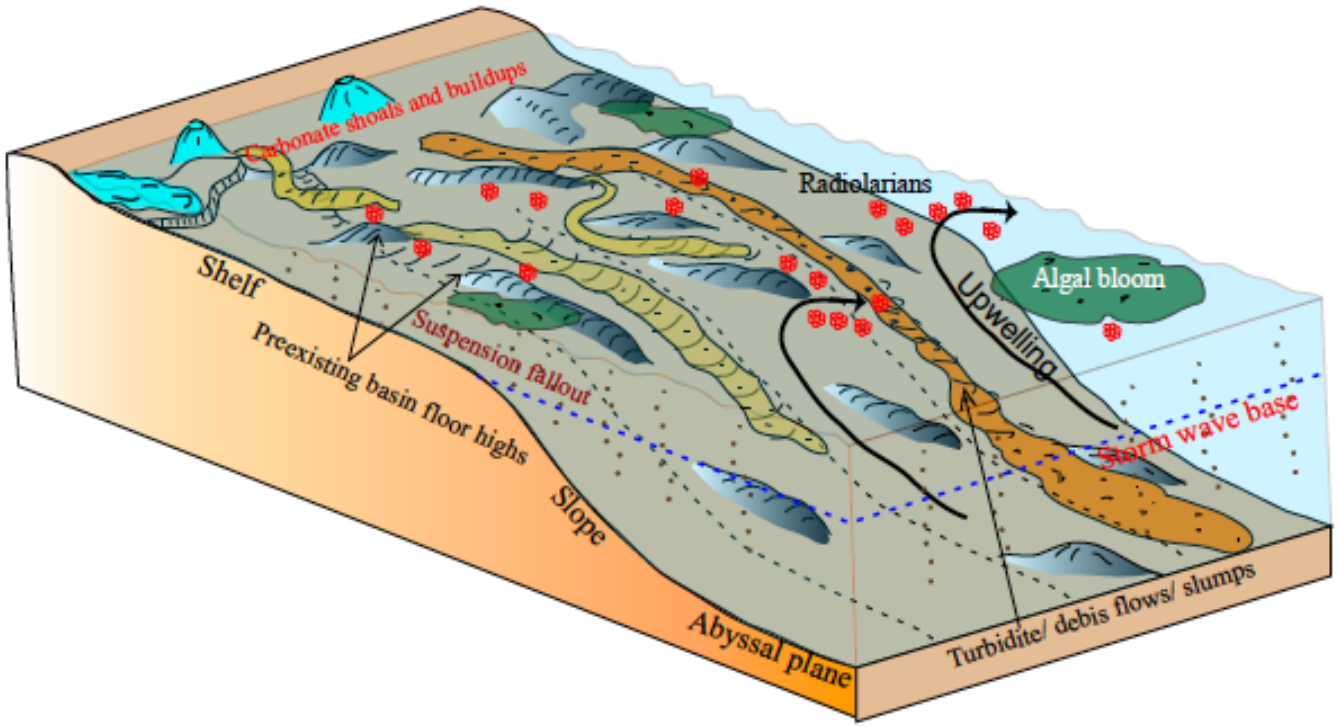

Figure 4.8-1: Proposed depositional model for the Woodford Shale.

4.9 Conclusions

Although superficially a homogeneous shale, the Woodford Shale records a prolonged period of complex and variable sedimentation. Paleoclimate and physiogeographic conditions allowed very little terrigeneous input, and provided a warm climate and upwelling possibly resulting in high biologic productivity. These three factors favored the deposition of organic-rich black shale. Restricted terrigeneous input allowed high concentration of clay even in the shallow part of the basin. Petrographic analyses was performed at microscopic and sub-microscopic scales since, very little can be seen megascopically due to dark color and fine-grained nature of the studied rock.

Integration of seismic, core and paleo data indicate that the Woodford Shale was deposited on top of an irregular unconformity surface that controlled the accumulation of the Woodford Shale. Basin floor topography resulted in thicker Woodford accumulation in topographic lows and thinner Woodford in areas of topographic highs. The thickness of the Woodford Shale may vary over considerably small distances, as seen in well 1 and well 3. Basin floor depressions are likely to receive any high-energy turbidity current related deposits in contrast to basin floor highs, which receive only the suspension fall-out. Basin floor highs are areas for clay-rich sediments, although they can have high TOC, they contain limited cherty facies, which provides the brittleness critical for initiating fractures within these rocks.

The presence of frequent high-energy deposits indicate that the Woodford Shale was deposited above the storm wave base (tens of meters) in the study area. High organic productivity and deposition of the huge organic ooze maintained low oxygen, reducing conditions, favoring thick accumulation of TOC-rich black shale.

Both petrographic observations and petrophysical properties indicate the cyclic nature of the Woodford deposition. Such cyclic deposition resulted in alternating cherty facies and TOC-rich ductile rock. Most of the depositional cycles are comprised of a lower organic-rich, high gamma-ray interval, with cherty facies near the top. This cyclicity provides the brittle-ductile rock couplet critical for the exploration within the resource shale. Good correlations between changes in bulk density, clay content, TOC and actual rock architecture indicate that it is possible to track the fine-scale stratigraphic changes using such petrophysical proxies in the uncored areas.

References

Cardott, B., 2008, Overview of Woodford gas-shale play of Oklahoma, US: AAPG Annual Convention and Exhibition.

Cardott, B. J., and M. W. Lambert, 1982, Thermal maturation by vitrinite reflectance of Woodford Shale, Anadarko basin, Oklahoma: AAPG Bulletin, v. 69, p. 1982–1998.

Comer, J., B., 2008a, Distribution and source-rock characteristics of Woodford Shale and age-equivalent Strata: AAPG Annual Convention and Exhibition.

Comer, J., B., 2008b, Reservoir characteristics and production potential of the Woodford Shale: World Oil, v. 229.

Comer, J. B., 1992, Potential for producing oil and gas from the Woodford Shale (Devonian-Mississippian) in the southern mid-continent, USA, Medium: X; Size: Pages: 574 p.

Fertl, W. H., and G. V. Chilingarian, 1990, Hydrocarbon resource evaluation in the Woodford shale using well logs: Journal of Petroleum Science and Engineering, v. 4, p. 347-357.

Hester, T. C., and J. W. Schmoker, 1983, Tectonic controls on deposition and source-rock properties of the Woodford Shale, Anadarko Basin, Oklahoma—loading, subsidence, and forebulge development: US Geological Survey bulletin.

Hester, T. C., J. W. Schmoker, and H. L. Sahl, 1990, Log-derived regional source-rock characteristics of the Woodford shale, Anadarko Basin, Oklahoma.

Johnson, J., G. Klapper, and C. A. Sandberg, 1985, Devonian eustatic fluctuations in Euramerica: Geological Society of America Bulletin, v. 96, p. 567-587.

Johnson, K. S., 1988, Geologic evolution of the Anadarko basin, in K. S. Johnson, ed., Anadarko basin Symposium: Circular 90, Oklahoma Geological Survey, p. 3-12.

Kvale, E. P., and B. Coffey, 2010, Depositional model for the Devonian Woodford Shale, SE Oklahoma, USA: AAPG Annual Convention and Exhibition.

Lambert, M. W., 1993, Internal stratigraphy and organic facies of the Devonian-Mississippian Chattanooga (Woodford) Shale in Oklahoma and Kansas: Source rocks in a sequence stratigraphic framework: AAPG Studies in Geology, v. 37, p. 163–176.

Paxton, S. T., A. M. Cruse, and A. M. Krystyniak, 2006, Detailed fingerprints of global sea-level change revealed in Upper Devonian / Mississippian Woodford Shale of south-central Oklahoma: AAPG Annual Meeting.

Sandberg, C. A., J. R. Morrow, and W. Ziegler, 2002, Late Devonian sea-level changes, catastrophic events, and mass extinctions, in C. Koeberl, and K. G. MacLeod,

eds., catastrophic events and mass extinctions: impacts and beyond: Geological Society of America Special Paper 356, Geological Society of America, p. 473–487.

Schieber, J., 1996, Early diagenetic silica deposition in algal cysts and spores; a source of sand in black shales: Journal of Sedimentary Research, v. 66, p. 175-183.

Schmoker, J. W., 1995, Woodford/Chattanooga/Arkansas/Novaculite of Midcontinent play, *in* M. E. Henry, and T. C. Hester, eds., Anadarko basin Province (058), USGS.

Sloss, L. L., 1963, Sequences in the cratonic interior of North America: Geological Society of America Bulletin, v. 74, p. 93-114.

Sullivan, K. L., 2006, Organic facies variation of the Woodford Shale, in western Oklahoma, The University of Oklahoma.

Chapter 5

5 Conclusions

Geologic history indicates that the Woodford Shale was deposited as organic rich black shale. Petrographic analyses indicate that planktonic organisms were the primary source of organic matter. Both petrographic observations and petrophysical properties reflect the cyclic nature of the Woodford deposition. The presence of frequent high-energy deposits indicate that the Woodford Shale was deposited above the storm wave base (at a depth of tens of meters) in the study area. Good correlation between bulk density, clay content, TOC and actual rock architecture indicate that these parameters can be used as proxies to track fine-scale stratigraphic changes. The upper part of the upper Woodford member records major changes in the depositional history, starting with slumping, followed by shallowing of the Woodford sea and then again a gentle sea-level rise indicating a possibility of TOC-rich upper Woodford in the deeper part of the basin. The slumping event is correlatable with the global event of storm and collapse of shelf margin.

My analysis indicates that quartz and clays along with TOC and porosity are the most important parameters in defining different economic petro-types within the Woodford Shale. TOC and porosity are correlated with reservoir quality. Highly quartz-rich cherty rocks, although characterized by poor reservoir quality (low porosity, low TOC), provide the brittleness needed to allow effective hydraulic fracturing for hydrocarbon production. Rocks with intermediate clay and quartz content are the best

reservoir rocks, with TOC increasing slightly with increasing quartz. The overall ductile nature of the TOC-rich rocks (indicated by elastic moduli) require intervening brittle rocks in order to initiate hydraulic fracturing and produce hydrocarbon.

SEM microstructural analysis reveals most of the pore spaces lie within organic matter (organic pores). Modal analyses of organic pores visible on SEM images and laboratory-measured porosity are consistent. The volume of organic pores increases with increasing thermal maturity. However, the distribution and development of such pores are complex and are controlled by the relative distribution of the different forms of extractable organic carbon, convertible organic carbon and residual organic carbon.

Attribute-assisted seismic stratigraphic and geomorphologic analyses indicate that the Woodford Shale was deposited on a very irregular surface controlling both lateral and vertical distributions of different petro-types. Sequential seismic geomorphologic analyses indicate stratigraphic changes during the Woodford deposition. A set of seismic attributes (coherent energy, mu-rho) highlights the distributions of ductile clay-rich rocks and comparatively brittle quartz-rich rocks at different level of Woodford deposition. Petrophysical properties extracted through simultaneous inversion of the pre-stack seismic data provides a means of petro-typing at a regional scale.